DESIGN AND MODELING OF A PNEUSMA SOFT ROBOTIC CATHETER DEVICE USING RESISTANCE-BASED MODELING OF NITINOL SPRINGS

By

EMILY A. ALLEN

A dissertation submitted in partial fulfillment of
the requirements for the degree of

DOCTOR OF PHILOSOPHY

WASHINGTON STATE UNIVERSITY
School of Mechanical and Materials Engineering

JULY 2022

To the Faculty of Washington State University:

The members of the Committee appointed to examine the dissertation of EMILY A. ALLEN find it satisfactory and recommend that it be accepted.

John P. Swensen, Ph.D., Chair

Arda Gozen, Ph.D.

Ming Luo, Ph.D.

Narasimha Boddeti, Ph.D.

ACKNOWLEDGEMENTS

I would like to express my sincere gratitude toward my research advisor Dr. John Swensen for offering guidance in my research, inspiring my curiosity, and pushing me toward my goals.

I am also grateful to other faculty members at WSU who contributed ideas and insight for my research endeavors; and to the other lab members—Ben, George, and Daniel—for their camaraderie over the last few years.

My parents are beyond deserving of thanks for their selfless support, prayers, wisdom, and encouragement throughout my life. My dad's contagious enthusiasm for engineering first piqued my interest in the subject.

Finally, I have been richly blessed by my friends and roommates who never fail to provide encouragement and distraction when needed most.

DESIGN AND MODELING OF A PNEUSMA SOFT ROBOTIC CATHETER DEVICE USING RESISTANCE-BASED MODELING OF NITINOL SPRINGS

Abstract

by Emily A. Allen, Ph.D.
Washington State University
July 2022

Chair: John P. Swensen

The soft robotics paradigm involves constructing robots out of soft materials to improve their safety and ability to interact with humans and delicate objects. Much research has been devoted to this emerging field in recent years as soft robotic devices lend themselves to a variety of applications ranging from wearable rehabilitation devices to biomimetics.

Soft, flexible devices show particular promise for medical applications where the ability to perform snake-like manipulations with soft devices could radically improve the safety and effectiveness of endoscopic and intravenous procedures. Where traditional catheter devices for these procedures can only be steered at the tip, there exists a need for more maneuverable devices with a high number of degrees of free-

dom (DOF) that can be controlled throughout the entire length. These devices would be capable of traversing sharp bends and branches, enabling access to more remote locations while reducing stress on surrounding tissue.

Recent efforts have focused primarily on pneumatic- and tendon-driven designs for flexible catheter devices. While these methods offer excellent maneuverability, they require complicated networks of tendons or supply tubes to accommodate individual control of each DOF in each series segment. In this dissertation, a hybrid pneumatic/shape-memory alloy (PneuSMA) actuation strategy is proposed for a flexible catheter device. The PneuSMA actuator is capable of multi-directional bending without requiring separate tendons or pneumatic chambers for each series segment.

The PneuSMA actuator design and fabrication method are explained, and a quasi-static analytical model is developed to predict the configuration of the device based on the input pressure and shape-memory alloy (SMA) activation. The PneuSMA analytical model relies on a resistance-based mechanical model for the SMA springs which is developed in this work. The resistance-based nitinol spring model can easily be applied more broadly to other SMA-actuated devices, and experimental results show good agreement between the predicted and experimental curvatures in a single pneuSMA actuator segment, indicating potential for precise control of the PneuSMA catheter device.

TABLE OF CONTENTS

Page

ACKNOWLEDGEMENTS iii

ABSTRACT iv

LIST OF FIGURES x

LIST OF TABLES xiv

CHAPTER

1. INTRODUCTION TO SOFT ROBOTICS 1

Motivation 1

Biological inspiration 2

Actuation 3

Dielectric elastomers 4

Shape-memory alloys 5

Fluidic actuators 6

Medical applications 7

Terminology 9

Existing soft robotic catheter devices 9

Objective and contents overview 13

Summary of main contributions 15

Contents organization 16

2. ELECTRO-MECHANICAL CHARACTERIZATION OF NITINOL SPRINGS 17

Abstract 17

Introduction 18

Applications of shape memory alloys 19

Existing nitinol models 20

Existing SMA control methods 23

Electrical resistance feedback 24

Resistance-based nitinol spring model 26

Background and modeling 28

Nitinol phase transformations 28

Electrical resistivity in metallic materials 31

Helical spring mechanics for large deformation 35

Nitinol spring force model 40

Characterization from measured data 54

Experimental setup 54

Methods 59

Temperature-resistance relationship 61

Strain-resistance relationship 62

Isoresistive mechanical tests 66

Model implications 74

Conclusions and future work 77

3. PNEUSMA ACTUATOR DESIGN AND MODELING 81

Abstract 81

Introduction 82

Pneumatic soft actuators 83

SMA's in soft actuators 84

PneuSMA actuator design 85

Soft actuator modeling/control methods 87

Background 89

Properties of nitinol material 89

Properties of silicone material 93

Experimental characterization of constituent materials 95

Nitiol spring characterization 95

Silicone characterization 103

Analytical model for PneuSMA actuator 115

State variables and curvature parameters 117

Silicone force distribution 120

Bending moment balance 122

Force balance 124

Model adaptations for alternative designs 126

Actuator fabrication 129
Experimental validation of analytical model 133
Sample preparation 133
Experimental setup 136
PneuFLEX curvature tests 138
PneuSMA constant pressure tests 139
PneuSMA constant heating tests 141
Model implications 146
Workspace comparison 147
Design optimization 149
Conclusions and future work 149
BIBLIOGRAPHY 154

LIST OF FIGURES

Page

1.1 Comparison of tip-steerable versus total-steerable catheter devices and the resulting stress on tissue at branch points and sharp turns due to passive design of tip-steerable devices. 10

1.2 Diagram of pneumatic/shape-memory alloy (PneuSMA) actuation approach for a soft, steerable catheter device. 14

1.3 Insertion of active, total-steerable PneuSMA catheter device into a curved channel to reach a target location. 14

2.1 Nitinol phase transformations. 29

2.2 Stress/strain diagram of nitinol phase transformations. 31

2.3 Factors affecting nitinol resistivity. 33

2.4 Helical spring coil parameters. 34

2.5 Conversion from geometry-specific spring strain and spring force to normalized material shear strain and shear stress. Dotted and dashed lines show the effects of different mandrel diameters with the same 0.25mm wire diameter; different colors represent the effect of the initial spring pitch (based on shape-setting) 41

2.6 Resistivity variation between phases. 51

2.7 Process of mounting nitinol springs on copper hooks using Molex crimp terminals to connect electrical wires. 55

2.8 Experiment setup for electro-mechanical testing of nitinol springs. . . 56

2.9 Circuit diagram for heating and measuring temperature/resistance of nitinol springs. 58

2.10 Isometric measurements of resistance vs. temperature in two different Nitinol springs. 61

2.11 Isothermal measurements of resistance vs. strain at room temperature in two different nitinol springs. 63

2.12 Conversion from twinned to detwinned martensite as a function of shear strain from room temperature test where ξ_0 is assumed to be one (pure martensite when $\gamma = 0$). 64

2.13 Conversion from austenite to detwinned martensite as a function of shear strain from highest temperature test where ξ_0 is assumed to be zero (pure austenite when $\gamma = 0$). 65

2.14 Measurements of shear stress versus shear strain at constant resistance in two different Nitinol springs. 69

2.15 Measurements of resistivity during loading from isoresistive tests in two different Nitinol springs. 70

2.16 Phase fraction evolution during isoresistive testing of two different nitinol springs. 72

2.17 Model fit to loading data from two different nitinol springs. 73

2.18 Families of isoresistive loading curves for two different nitinol springs. 74

2.19 Loading surface as a function of resistivity for two different nitinol springs. 75

3.1 PneuSMA actuator design and bending capabilities. 86

3.2 Illustration of various PneuSMA actuator configurations achievable by heating select regions of nitinol springs. 87

3.3 Isoresistive stress-strain curves generated by resistance-based model from the previous chapter for 35°C nitinol springs. 96

3.4 Residual strain as a function of pre-strain for 100% martensitic nitinol springs. 97

3.5 Residual strain in 35° nitinol springs from Eq. 3.2 as a function of pre-strain and onset martensite fraction. 99

3.6 Stress-strain curves generated from Eq. 3.3 for various pre-strains at different onset martensite fractions. Bold black curves represent initial conditions in PneuSMA actuator springs which have been pre-strained to $\gamma_p = 0.1924$. 102

3.7 Stress-strain curves for PneuSMA actuator springs that are pre-strained to $\gamma_p = 0.1924$. Left: recovery of residual strain upon heating from $\xi_0 = 1$ to $\xi_0 = 0.4$. Right: keeping of residual strain γ_R during cooling from $\xi_0 = 0.4$ to $\xi_0 = 1$. 103

3.8 Samples and setup for standard tension and bulk compression testing of silicone material. 105

3.9 Samples and setup for tension and buckling testing of fiber-wrapped silicone tubes. 107

3.10 Stress-strain data from five different mechanical tests on Dragon Skin 10 FAST silicone. 109

3.11 Stress-stretch data from uniaxial tension and tube tension tests, along with Neo-Hookean hyperelasticity model fit to uniaxial tension data. . 111

3.12 Silicone tube elongation tests compared with predicted elongation from uniaxial stress assumption and Neo-Hookean model. 116

3.13 Left: dimensions of nitinol springs and silicone tube. Center: coordinate system used for analytical modeling. Top center: silicone force distribution throughout cross-section for bending actuation. Right: configuration variables and curvature parameters. Top right: force balance on actuator cap. 118

3.14 PneuSMA actuator fabrication process for 2-spring actuator. Steps (a)-(e) show the silicone tube casting; steps (i) - (j) show the pre-stretching and placement of the nitinol springs; steps (k) - (m) show the fiber wrapping process, and steps (n) - (t) show the silicone coating and the attatchment of the supply tube and electrical connectors. . . 130

3.15 Electrical connections to nitinol springs created by crimping Molex crimp terminals around a copper core inserted into nitinol coils. . . . 133

3.16 PneuSMA and PneuFLEX samples for experimental validation. . . . 135

3.17 Wiring diagram and experimental setup for PneuSMA actuator tests. 137

3.18 Measured curvature versus model-predicted curvature for three different PneuFLEX actuator geometries. 138

3.19 Applied pressure and RMS current input during constant pressure PneuSMA tests. 140

3.20 Measured electrical resistance in nitinol springs during constant pressure testing of the PneuSMA actuators. Dots represent actual measurements; solid lines are polynomials fit to the measured data. 140

3.21 Comparison of measured curvatures and model-predicted curvatures from constant pressure testing of PneuSMA actuators. Solid curves represent model prediction; discrete points represent measured curvatures. 142

3.22 Typical pressure input for constant heating PneuSMA tests. 143

3.23 Measured electrical resistance in nitinol springs during constant heating testing of the PneuSMA actuators. Arrows indicate the test starting points; dots represent actual measurements; solid lines are fit to smooth the measured data. 144

3.24 Comparison of measured curvatures and model-predicted curvatures from constant heating testing of PneuSMA actuators. Solid curves represent model prediction; discrete points represent measured curvatures. 145

3.25 Workspace comparison between PneuFLEX and PneuSMA actuators. The bottom row shows the minimum and maximum curvature configurations within a pressure range of 0-60 kPa (0-8.7 psig). 148

3.26 Demonstration of possible circuit design for independent current control in three segments of a nitinol spring using a single voltage source. 152

LIST OF TABLES

Page

2.1 Variable names and definitions. 45

2.2 Curve fit functions for detwinning and resistivity profiles. 67

3.1 Polynomial fits to Dragon Skin 10 FAST silicone mechanical test data. 110

3.2 Neo-Hookean hyperelasticity model parameters for Dragon Skin 10 silicone. 112

3.3 PneuSMA and PneuFLEX sample dimensions. 134

CHAPTER ONE

INTRODUCTION TO SOFT ROBOTICS

1.1 Motivation

With the steady advancement of robotics technology, autonomous solutions to manufacturing, assembly, mining, and packaging have become increasingly prevalent in the workplace. Robots are well-suited for repetitive tasks that require high speed and strength without compromise of precision and reliability. However, industrial robots are generally restricted to isolated environments due to their heavy, rigid design and their potential to harm humans in their vicinity.

Recently, researchers have strived towards a new goal of creating robots that are capable of collaborative operation alongside humans in less restricted environments. This objective requires robots to have excellent response to uncertainty in order to meet safety criteria and function in less predictable environments. With these aspirations, the field of soft robotics emerged, inspiring a surge of research over the last two decades. The soft robotics approach has shifted the entire paradigm around robot materials, structures, actuation, and control. Whereas traditional robots host a variety of heavy, rigid components driven by high power motors, soft robots feature soft materials such as gels, rubbers, and other elastomeric materials. The soft nature of these materials enables conformation to ill-defined surfaces, distribution of impact

forces, shock absorption, and other compliant behaviors that improve collision safety, as reviewed by Kim et al. [85]. Soft robotics is a multi-faceted field encompassing investigations on soft materials, morphological implications, and design/modeling challenges [76]. Laschi and colleagues note that the pairing of creative actuation strategies with the deformable nature of the soft materials enables soft robots with squeezing, stretching, climbing, and morphing capabilities that are unachievable by their rigid counterparts [90]. With the development of advanced soft materials, a new realm of applications for robots has become arisen, including wearable rehabilitation devices, soft grippers for fragile objects, prosthetics, and tools for minimally-invasive surgical procedures [18, 71].

1.2 Biological inspiration

Many soft robot designs are inspired by biological examples seen in nature. Soft tissue and musculature are the primary means of structure and actuation in many adept creatures which demonstrate the potential for advanced capabilities in biologically-inspired soft robots.

In natural hydrostatic mechanisms, fluid pressure gradients and geometric constraints control the configuration of a biological structure. Such mechanisms are seen in muscular hydrostats such as the elephant trunk, the human tongue, squid tentacles, and carnivorous plants such as the Venus flytrap. With their intelligent actuation capabilities, these flexible structures can morph into a variety of configurations

and exert substantial forces despite their lack of skeletal support [179, 134, 127, 30]. The working principles in muscular hydrostats—based on the pressure regulation between layers, muscle fiber arrangements, and fluid incompressibility—show particular promise for soft robotics applications where achieving high-strength manipulations with flexible materials is the main objective. Many research efforts have sought to mimic these remarkable capabilities in soft robotic devices [89, 31, 116, 115, 93, 155]. Other biological feats such as worm locomotion, frog jumping, and intestinal peristalsis have also served as inspiration for biomimetic soft robots [40, 168, 88, 60, 85].

Although mimicking intricately-designed biological organisms is a lofty objective, basic working principles from these adept plants and creatures can be incorporated in simplistic soft robotic devices.

1.3 Actuation

Whereas traditional robots typically use actuators to drive discrete joints between rigid links, soft robots form holistic actuator structures where actuation is distributed throughout the structure. Soft robot actuator structures are often referred to as continuum actuators. While the idea of continuous actuation promises improved spatial resolution, traditional rigid actuators such as electric motors are not suitable for these actuators. Kim et al. classifies approaches to continuous actuation in three main categories: dielectric elastomer actuators (DEA's), shape-memory alloy actuators (SMA's), and pressurized fluid actuators [85]. Numerous other approaches

to soft robot actuation have been explored, including gel actuators, shape-memory polymers, magnetic actuators, and fiber/yarn actuators as reviewed by Yang et al. [198], but these mechanisms lie outside the focus of this work.

1.3.1 Dielectric elastomers

Dielectric elastomer actuators (DEA's) are made up of a thin polymer film coated with flexible electrodes on both sides. When a potential difference is applied across the electrodes, the attraction between charges on electrodes causes a Maxwell stress on the polymeric material which results in compression of the polymer in the thickness direction. Since most dielectric polymers are nearly incompressible, the decrease in thickness must be accompanied by a lateral expansion. This conversion from electrical energy to mechanical energy has been harnessed in soft actuators capable of several different types of motions. By varying the arrangement of electrodes and passive, strain-limiting layers, contraction, twisting, expansion, bending, and gripping motions can be achieved [200, 160]. Common dielectric materials include polyurethanes, silicone, or acrylic elastomers, which offer intrinsic flexibility and biocompatibility [21]. Electrodes are usually made of carbon powder, graphite, or carbon grease [200, 67]. The dielectric effect can also be used to enable self-sensing through capacitive feedback signals [8]. Widespread usage of DEA's is limited by low payload capacity, slow response time, high voltage requirements, and susceptibility to dielectric breakdown when charge leaks across the dielectric [33, 68].

1.3.2 Shape-memory alloys

Shape-memory alloys (SMA's) are a unique class of materials characterized by their ability to recover substantial strain by thermal cycling. At low temperatures, SMA's are relatively soft and flexeible and can be easily deformed into a new shape or length. When heated, SMA's revert to their original shape due to a phase transformation, and they recover any previous deformation, up to about 6-8% strain. This effect, known as the shape-memory effect, can be used to deform structures and cause desirable motions. In soft actuators, SMA wires or springs are often embedded in a soft matrix material in some arrangement with eccentricity from the mid-plane. When the wires are heated—usually via Joule heating—they contract, producing an out-of-plane motion that can be bending or twisting depending on the arrangement and activation sequence [182, 148, 80, 63, 91, 186, 74, 184]. When the wires are cooled, the stiffness of the matrix or the addition of other biasing elements causes the SMA wires to elongate, and the structure returns to its original configuration. Because the SMA wires can be embedded in the soft robotics structure directly, the need for separate motors or drive trains is eliminated. Unfortunately, embedding the wires in an insulative matrix causes slow heat transfer, so response time is a common challenge in these configurations. Although SMA wires are limited to low strains, coiling the wire into springs enables significantly larger stroke at the expense of some strength reduction [84, 85, 21, 89, 156]. The most popular SMA materials include CuAlZn,

NiTiCu, NiTiNb, and most commonly NiTi due to its superior memory and superelasticity [29]. An in-depth explanation of SMA working principles and examples of SMA applications are given in Chapter 2.

1.3.3 Fluidic actuators

Fluidic actuators use pressurized air or other fluid to deform soft structures. Pneumatic actuators are typically designed with fabric or fiber constraints that direct the expansion in a particular direction to produce a desired motion [136, 181]. The well-known McKibben actuators—also known as pneumatic artificial muscles (PAM's)—feature a braided sleeve placed over the pneumatic chamber that converts the radial expansion to axial shortening upon inflation of the chamber [101, 87]. This contractile behavior mimics the function of human muscles, and much effort has been devoted to optimizing the weave angle for optimal force and stroke output [17, 175, 27]. Other motions, such as bending, twisting, and extension can be achieved by varying the fiber arrangement [5, 182, 162, 163]. Pneumatic bending actuators such as the PneuFLEX actuator by Deimel and Brock typically involve a silicone tube with a tightly-spaced circumferential fiber wrapping along the entire length of the tube [45, 59]. This configuration, on its own, causes extension when inflated as the circumferential fibers prevent radial expansion and direct the expansion in the axial direction. To induce bending, a strain-limiting element—such as an inextensible fabric or fiber–is embedded along one side of the tube such that only one side can elongate under an applied

pressure. Similar bending behavior can be achieved via anisotropic rigidity or by designing asymmetric cross sections where a thicker wall on one side serves as its own strain limiting element without need of fiber or fabric constraints [72, 170, 42]. Others have incorporated bellows to reduce bending stiffness and direct the expansion in a desired direction [145, 187, 49]. Fluidic actuation is a logical choice for soft actuation as the media involved—typically air and silicone or other low density elastomers—are intrinsically lightweight, yet they can produce large forces and displacements [189, 158, 181]. Fluidic actuators are subject to leaks and are generally limited by their inability to perform diverse manipulations without complicated networks of supply tubing [85].

1.4 Medical applications

One of the major motivations for soft robotics research lies in the promising medical applications of such devices. The idea of swapping traditional rigid instruments with flexible actuators made of soft, elastic materials could significantly reduce the risk of injury and discomfort in a variety of medical procedures [2, 178, 32]. The necessity of "compliance matching," as coined by Majidi, is especially relevant in the realm of medical devices where tools should closely match the stiffness of the tissue they are in contact with to prevent damage [111]. De Greef and colleagues point out three main areas of application where flexible medical instruments would prove beneficial: minimally invasive surgery (MIS), endoluminal surgery, and catheterization

procedures [42].

Minimally invasive surgery involves performing an operation through one or more small incisions by inserting a camera and tools through a small opening rather than cutting open an entire area [120]. The recent shift towards MIS techniques has significantly reduced trauma and recovery time for patients, but it has created a need for flexible instruments that can bend to reach different target locations without requiring multiple insertion points and hence additional incisions [14]. This is especially important for procedures in the chest cavity where tools must pass between ribs [41].

Endoluminal surgery involves passing tools through natural orifices such as the mouth, rectum, vagina, or ear canal to perform procedures such as dissection, suturing, or stapling [24]. These procedures allow internal organs to be accessed with reduced invasiveness compared to laparoscopic techniques. Many conditions such as gastric ulcers, gastro-esophageal reflux disease (GERD), gastro-intestinal tumors, and ear canal fistula or cysts may be identified and treated with endoluminal procedures [24]. Flexible instruments capable of snake-like motions are desirable for such applications [140].

Degreef et al. and Ikuta et al. use the term, "catheterization," to refer to the insertion of a thin tube into a vessel to diagnose and treat vascular system diseases [42, 78]. This technique may be used to collect blood samples, inject dye for imaging purposes, or treat blockages in the vascular network. Catheters are usually guided

to the area of interest from an insertion point in a peripheral vessel in the arm or leg. Traditional catheter devices use a guide-wire approach which enables some steerability of the tip, but the remainder of the device remains passive which can impose significant stress at branch locations as shown in Figure 1.1. Additionally, Ikuta and colleagues point out that accessing remote locations with traditional guide-wire catheters is difficult due to tight bends and branching of vessels, hence the need for active soft catheters with improved maneuverability [78].

1.4.1 Terminology

The term, "catheter," is often used more broadly to describe any flexible device guided through a small cavity, including urinary catheters, endoscopes, and any tools used for endoluminal surgeries, as well as vascular catheters. In this dissertation, the term, "catheter" will be used in this broad sense, and the term, "endoscopic," will refer to any procedure requiring navigation through a bodily channel, including both endovascular and endoluminal procedures in the gastro-intestinal tract, urinary tract, nasal cavity, ear canal, or vascular system.

1.4.2 Existing soft robotic catheter devices

Much effort has been devoted to the development of soft, flexible catheter devices to meet the needs of today's medical world. Whereas traditional, FDA-approved devices such as the Invendoscopy colonoscope [66] rely on manual pushing for insertion

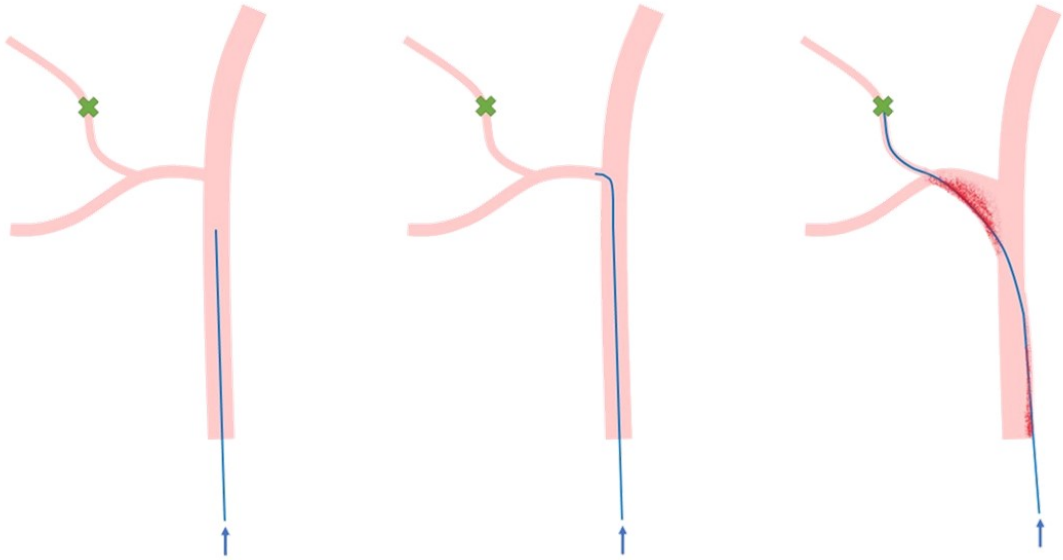

(a) Tip-steerable catheter device.

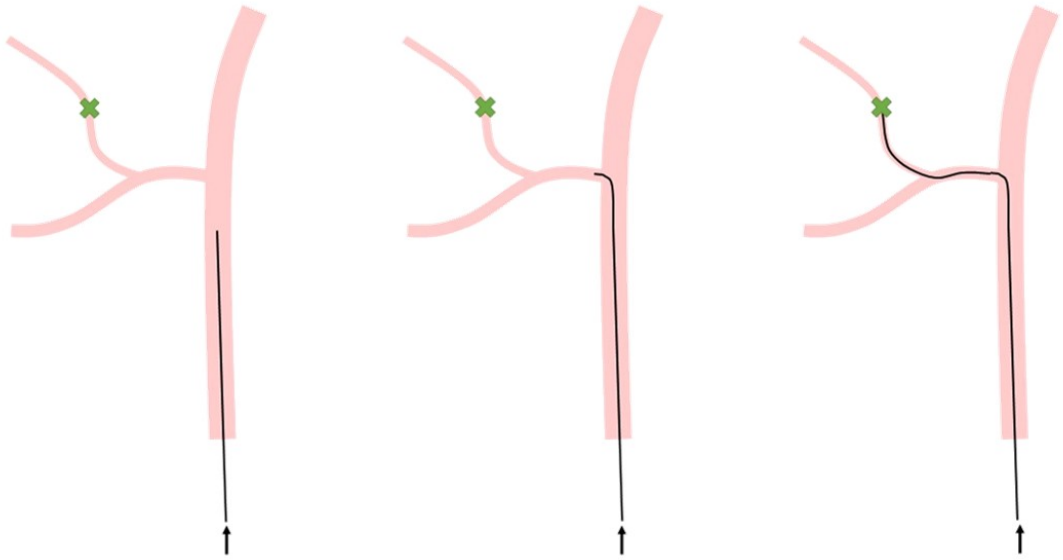

(b) Total-steerable catheter device

Figure 1.1: Comparison of tip-steerable versus total-steerable catheter devices and the resulting stress on tissue at branch points and sharp turns due to passive design of tip-steerable devices.

and only offer controlled bending at the tip, recent attempts with soft robotic catheter devices have veered towards the goal of total-steerability, where bending may be controlled at any point on the length of the snake-like device. The most common approaches to soft robotic catheter devices involve modular assemblies of pneumatic- or tendon-driven bendable segments.

Tendon-driven soft catheter devices include the MINIR robot by Kim et al. [86] and the Meshworm robot by Bernth et al [16]. The MINIR robot was designed specifically for endoscopic neurosurgery but could easily be applied more broadly in the medical field. This device consists of four disks connected in series by inner springs with opposing pairs of tendons used to induce bending in each of the three segments between disks. The tendons are actuated by SMA springs, and a continuous corrugated sheath encases the entire device with an outer diameter of 12.6 mm [86, 62]. The Meshworm robot is another example of tendon-driven flexible catheter technology, in this case designed for colonoscopy. This earthworm-inspired device is intended for peristaltic locomotion via anchoring, contracting, unanchoring, etc. against the colon wall. The device features a polyester mesh exterior with controllable bending/extension/contraction in three series segments. Opposing pairs of tendons wrapped around small pulleys are driven by DC motors that cause the desired peristaltic behavior [16, 62].

Influential fluidic soft catheter devices include the STIFF-FLOP soft robot by

Cianchetti et al. [34] with improvements by Fras et al. [55], and the modular soft manipulators by Gerboni et al. and Suzumori et al. [61, 171]. The design of the STIFF-FLOP robot for MIS was inspired by the working principles of the octopus arm. The initial design by Cianchetti et al. combines pneumatic actuation with granular jamming to enable both spatial maneuverabity and stiffness control. Bending is controlled by inflating—and hence elongating—one of three pneumatic chambers arranged in a triad within a 32 mm corrugated sheath which limits radial expansion [62]. An 8 mm diameter core of coffee grounds sealed in a latex membrane runs through the center of the device. Drawing a vacuum on the central chamber increases the stiffness of the device as the particles bind together under the vacuum [34]. Fras and colleagues later modified the STIFF-FLOP design, switching to cylindrical pneumatic chambers and including a fiber wrapping on each individual chamber to eliminate the need for an external sheath and its associated drawbacks. This modified design features a reduced outer diameter of 14.5 mm [55]. Both STIFF-FLOP designs encompass modular segments, each requiring four separate supply tubes to accommodate the coffee particle-jamming core and the three pneumatic chambers. The modular soft manipulators developed by Gerboni et al. and Suzumori et al. feature nearly identical designs to the STIFF-FLOP actuator, but exclude the particle-jamming core and thus do not offer variable stiffness capabilities [171]. The Gerboni manipulator is unique in that it includes a central fluidic distributor with miniature latching valves

for each branching chamber [61]. While the latching valves eliminate the bulk of numerous supply tubes running to each chamber from the base, including the valves within device also consumes space and adds weight to the device.

A further review of seminal works similar to the proposed catheter design is presented in the introduction to Chapter 3.

1.5 Objective and contents overview

Ultimately, both the tendon- and pneumatic-based approaches are limited by the same challenge: scalability. With each series segment requiring its own separate supply tubes or tendons, longer, multi-segmented devices are infeasible within the diameter constraint for endoscopic procedures. In addition to consuming space, fitting numerous supply tubes within the device also increases the bending stiffness, thus limiting the curvature capabilities. Routing separate tendons to each segment not only produces a complicated network but also applies undesirable compression and torque on proximal segments when tendons from distal segments are contracted [181]. The objective of the present work is to design a soft catheter device that is capable of multi-segmented bending without requiring excessive tendons or supply tubes.

The design of the pneumatic/shape-memory alloy (PneuSMA) catheter features a single, fiber-wrapped pneumatic chamber with pre-stretched SMA springs attached along the sides, as shown in Figure 1.2. Selected segments of the SMA springs may be heated to cause bending in any region of the device. Multiple segments in opposing

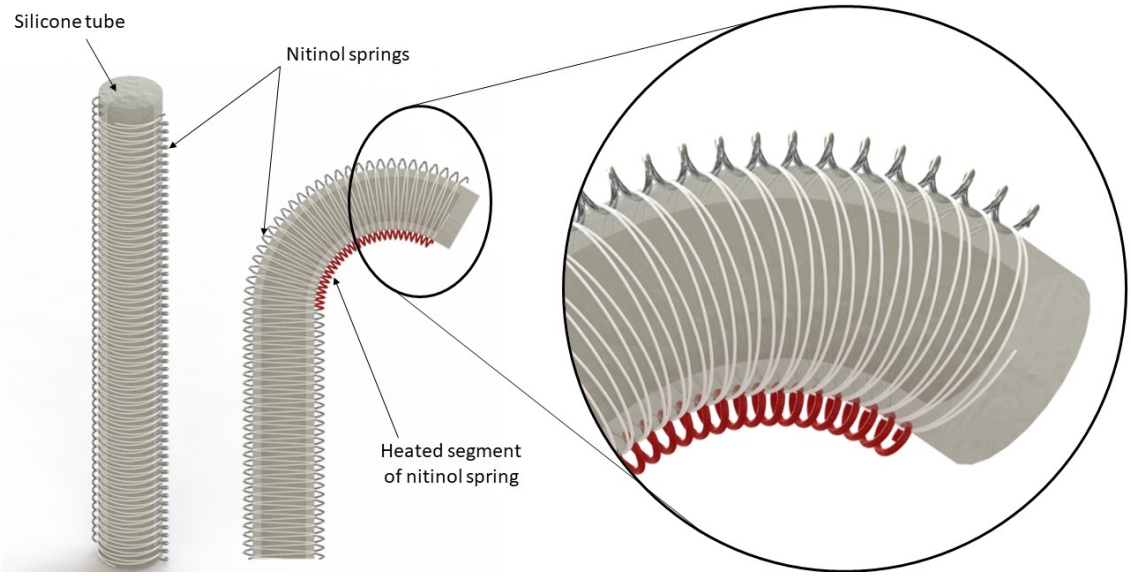

Figure 1.2: Diagram of pneumatic/shape-memory alloy (PneuSMA) actuation approach for a soft, steerable catheter device.

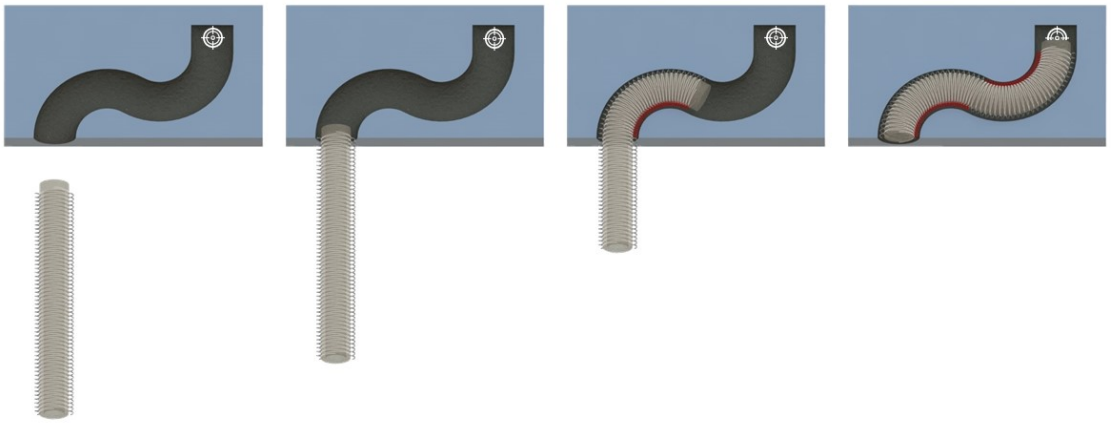

Figure 1.3: Insertion of active, total-steerable PneuSMA catheter device into a curved channel to reach a target location.

SMA springs may be activated simultaneously to produce snake-like manipulations through a tortuous lumen, as shown in Figure 1.3.

1.5.1 Summary of main contributions

The major contributions of the research presented in this dissertation are summarized as follows:

- Development of a resistance-based mechanical model for nitinol springs to enable more feasible control of soft devices with embedded SMA's. This model relies on electrical resistance as a surrogate for temperature measurement to eliminate the need for embedded temperature sensors and associated measurement errors.

- Design of a hybrid soft actuation approach for soft catheter devices with improved safety and maneuverability. The pneumatic/shape-memory alloy (PneuSMA) actuation method allows for multi-directional bending along the length of the device without need of numerous tendons or supply tubes.

- Development of a quasi-static analytical model to predict the configuration of PneuSMA-actuated devices based on the input pressure and measured resistance of the nitinol springs.

1.5.2 Contents organization

The remainder of this dissertation begins with a comprehensive characterization of nitinol springs in Chapter 2. An overview of shape-memory alloy applications and existing modeling/control strategies are presented, along with a review of the underlying principles involved. A resistance-based mechanical model is developed based on the spring mechanics and electrical properties of the nitinol. The experimental test methods and results are also given to validate the proposed model, and the implications and applications of the resistance-based model are discussed in the conclusion of Chapter 2. Chapter 3 focuses on the design and modeling of the PneuSMA catheter device, beginning with a summary of existing pneumatic actuators and associated modeling/control methods. The properties of the silicone material are measured experimentally to account for geometry-specific behaviors. The application of the resistance-based nitinol spring model to the pneuSMA actuator modeling is described, and further extensions are made to account for device-specific nuances. A quasi-static analytical model is developed for a single module of the PneuSMA catheter based on the mechanical models from each constituent material. The PneuSMA actuator fabrication process is described, and experimental validation of the analytical model is is conducted on several PneuSMA actuator variations. Implications of the PneuSMA catheter design and model are discussed in the conclusion of Chapter 3. A review of chapter-specific seminal works is included in the introduction to each chapter.

CHAPTER TWO

ELECTRO-MECHANICAL CHARACTERIZATION OF NITINOL SPRINGS

2.1 Abstract

The prevalence of shape memory alloy (SMA) actuators in robotics, aerospace, and biomedical fields has continued to rise, yet the complex modeling and control of such devices remains an obstacle to further democratization. Position control methods for SMA actuators such as nitinol have been well studied using several approaches but most rely on feedback of one or more external variables such as force or strain which can be difficult to measure, especially in small-scale or flexible devices. Previous studies have shown that electrical resistance is strongly correlated to the temperature, stress, and resulting phase transformations in SMA's. Hence, the electrical resistance can be used to monitor intrinsic microstructural changes without requiring additional information about temperature and loading conditions. This self-sensing feature has been utilized to enable position control via resistance feedback in many simplistic devices, but these control schema are often based on constant loading criteria, do not apply to the pseudo-plastic deformation region, or only apply to straight wire geometries. This article presents a generalized resistance-based mechanical model for nitinol springs that is normalized for application to other

spring geometries. The proposed resistance-based model offers an extension from the thermo-mechanical constitutive models by Brinson and An et al. with modifications to eliminate temperature-dependence and to account for interactions between multiple phases and variants in polycrystalline nitinol. Electro-mechanical testing of two different nitinol springs is used both for characterization of detwinning behaviors and associated resistivity profiles and for validation of the proposed model.

2.2 Introduction

Shape memory alloys (SMA's) have been widely used in robotic devices, with applications ranging from pinch valves to adaptive aerodynamics. Different alloy compositions, most commonly including blends of copper, aluminum, nickel, and/or titanium, offer different thermo-mechanical properties, but each exhibit the same fundamental shape-memory effect and pseudo-elastic capabilities. Because of its biocompatibility, corrosion resistance, and desirable mechanical and electrical properties, the most common choice of SMA is Nitinol, a blend of nearly equal parts nickel and titanium [25]. This unique material can recover large pseudo-plastic strains at low temperatures due to the shape-memory effect, and its pseudo-elastic properties at high temperatures enable substantial force and displacement without accrual of permanent deformation.

2.2.1 Applications of shape memory alloys

Many devices capitalize on the shape-memory effect for applications including continuum robots, grippers, medical devices [12], seismic protection [102], and even aerodynamic optimization. In robotic devices, nitinol wires or springs are often used as an actuation mechanism. The shape-memory alloy wires or springs can be embedded directly within a soft, deformable matrix, or positioned eccentrically around a bendable spine. In such applications, activation causes the SMA wire or spring to contract, inducing a desired motion. The thermal actuation is generally achieved by passing an electrical current directly through the wire wherein heat is generated due to the Joule heating effect. Shape-memory alloy actuators are often paired with biasing elements such as steel mechanical springs to return the element to the original configuration upon cooling and relaxing of the SMA [125]. This type of arrangement has been employed to cause bending in continuum robots or catheter devices [63, 148], deform a flat membrane in industrial vacuum grippers [123, 124], activate automotive latches [144], or alternately pinch and release a section of tubing for flow control [133]. In the aerodynamics field, SMA's have been used to improve aerodynamic performance by actively modifying the profile of aerodynamic features on aircraft and various land vehicles [154, 70]. These types of morphing capabilities have been achieved by using SMA wires to modify wing camber [197] or control the thickness of flexible wing skins [141], or using SMA springs to discretely actuate various points

on an airfoil [48]. Further applications of SMA's have been reviewed by Hartl and Lagoudas [70], Petrini and Migliavacca [135], Motzki and Seelecke [125], Barras and Myers [12], and Sadashiva [105].

2.2.2 Existing nitinol models

Shape memory alloys are prized for their compactness and ideal mechanical properties which make them superior to alternative actuation mechanisms in many scenarios [130]. However, their complicated thermo-mechanical properties make them difficult to implement and often limits their use to simplistic devices [70]. Much effort has been devoted to characterizing the mechanical properties of SMA's based on underlying thermodynamics, phase transformation kinetics, and microstructural behaviors. Cissé et al. organized existing modeling approaches into microscopic, micro-macro, and macroscopic categories based on the scale of the theories used in each model [35]. Microscopic models analyze lattice or grain crystal behaviors such as phase nucleation, interface motion, twinning, etc. using molecular dynamics or other theories. Early microscopic models such as [51, 52, 11, 13, 1] are derived from energy expressions, with later modifications presented in [94, 95, 96, 183, 47, 109, 185, 81]. These models capture important underlying principles, but are impractical to use due to their computational cost and inconvenient modeling scale [35]. Micro-macro models use micromechanics to explain the interaction of energy within the material at the micro scale, then macroscopic implications arise from averaging the behavior of

single grains and applying an appropriate scale transition. Commonly-used scale transition techniques include the Mori-Tanaka scheme [121], self-consistent schemes [132], uniform stress scheme [203], and finite element methods [58]. Micro-macro modeling approaches, demonstrated in [169, 73, 19, 151], often produce accurate simulations but rely on many state variables and material parameters, incurring computational cost and characterization challenges [35]. Macroscopic models seek to avoid the complexity of small-scale models by focusing on phenomenological behaviors, considerable simplification of micro-macro thermodynamics, or direct fits to experimental data. These approaches offer the most practical solutions to modeling challenges and have been the focus of most recent works.

Most macroscale models stem from the early work of Tanaka [172], who combined mechanical and kinetic law to describe the behavior of polycrystalline SMA's using a temperature-dependent constitutive model. The Tanaka model was the first to account for crystallographic structural changes using an internal state variable ξ to represent the amount of each phase present in the material [102]. Liang and Rogers [99] later revised the Tanaka model, representing ξ as a cosine function of temperature and stress instead of the exponential function proposed by Tanaka. Both of these models only apply to transformation from twinned martensite to austenite and vice versa; they fail to account for the detwinning behavior responsible for the shape-memory effect and pseudo-elasticity. This omission was later corrected by Brinson

who modeled the detwinning behavior by splitting ξ into two separate state variables to distinguish between temperature-induced (twinned) martensite and stress-induced (detwinned) martensite [23, 22]. A slight modification to the Brinson model was introduced by Chung et al. to prevent the occurrence of an inadmissible phase fraction where $\xi > 1$ [28]. The Brinson model is widely accepted, although it is limited to one dimension for application to simple straight wire SMA geometries. Most 3D constitutive models are too complicated for practical engineering applications as they require numerous parameters and advanced computations.

A significant factor in each of the major constitutive models is the description of the elastic modulus evolution. The stiffness of SMA's varies substantially with temperature and subsequent phase change, so the elastic modulus cannot be considered constant. Several functions for $E(\xi)$ were suggested by Auricchio and Sacco for nitinol alloys, based on the Mori-Tanaka scheme, Reuss scheme, and Voigt scheme [9]. The Mori-Tanaka scheme analyzes the distribution of stress with elliptical inclusions of martensite in an austenite matrix and vice versa; the Reuss scheme models nitinol as a periodic composite; and the Voigt scheme models nitinol as a parallel combination of marteniste and austenite, sharing the applied load. The Reuss scheme has proven most experimentally valid, with the Voigt scheme providing an upper bound [9].

2.2.3 Existing SMA control methods

Early SMA actuators rely on predictive modeling using on/off control with feed-forward architectures. These open-loop control schema are sufficent for many 2-state mechanisms such as valves, grippers, and bistable mechanisms, but they lack precision and robustness toward environmental perturbations and variable applied loads. More advanced applications require feedback control to successfully compensate for hysteresis effects and system disturbances [104]. Many PID controllers have been implemented for position control of SMA-actuated devices. Ikuta groups these SMA controllers into two groups: controllers with feedback of (1) external variables such as force or position, or (2) internal state variables such as temperature or electrical resistance [77]. Successful implementation of controllers from the first category have been proven in [63, 165]. Teh et al. developed a two-loop control architecture for simultaneous position and force control using two feedback variables [199]. Each of these controllers relies on position and/or force feedback from embedded sensors such as encoders, strain gauges, load cells, linear variable differential transformers, etc. Unfortunately, integrating position or force sensors adds considerable mass, volume, and complexity to otherwise light, simple devices. Additionally, SMA's are often embedded in a soft matrix to create intelligent material structures; measuring force or strain in this configuration proves challenging [192]. Ikuta also points out that the external variables feedback methods can cause overheating when loading fluctu-

ations or temperature disturbances are present [77]. To avoid these drawbacks, some researchers have incorporated temperature feedback into SMA control algorithms [50, 82, 106, 149]. A comparison of position feedback versus temperature feedback for SMA position control was conducted by Troisfontaine et al. [177]. The temperature feedback approach is impractical due to dramatic hysteresis during phase transformation and the difficulty in obtaining precise temperature measurements [139, 26, 166].

2.2.4 Electrical resistance feedback

Using electrical resistance as a feedback variable has been proposed by several researchers as a means of avoiding overheating, reducing hysteresis, and providing robustness against variable ambient conditions [77, 167]. It has been shown that the electrical resistance of SMA's is closely correlated to temperature, stress, and resulting phase transformations [3, 191, 159, 56, 129]. Crystallographic changes in SMA's can be caused by both temperature—which causes thermoelastic phase change—and applied stress—which causes variant alignment according to lowest Schmidt factor [3]. The electrical resistance of the alloy gives direct insight into the immediate microstructure without requiring in-depth analysis of the underlying heat and stress distributions. In SMA's like nitinol with multiple transformations at overlapping temperatures, monitoring the electrical resistance can help identify phase changes and the sequence of transformations [3].

A linear relationship between resistance and strain has been observed with only

modest hysteresis during the temperature-induced phase transformation of straight wire SMA's at constant temperature and constant stress [104, 3, 191, 159, 39, 57]. The slope and intercept of this linear relationship changes with different temperatures and applied loads. Additionally, the correlation between strain and resistance is due in part to the change in cross-sectional area of the wire when stretched. The relationship becomes nonlinear when other geometric configurations are employed [159] or when temperature and/or stress are non-constant. When the R-phase—an intermediate rhombohedral phase appearing in some nitinol alloys—is present, significant complexity and nonlinearity is introduced to the resistance, but this phase can be avoided by selecting appropriate treatment processes [129, 39].

Despite these limitations, the relationship between resistance and strain has been exploited to enable self-sensing capabilities in many SMA-actuated devices, for example [56, 92, 150, 69, 107]. In each of these applications, resistance feedback is used to successfully achieve position control of an SMA actuator. However, these models are limited as many lack consideration of hysteresis effects, lack geometric generalization, do not apply to variable loads, or are based on experimental measurements unique to a particular device. Lynch et al. addressed the issue of variable loads by developing a family of linear curves for heating/cooling paths with coefficients defined by polynomial functions of stress [104]. Lynch and colleagues successfully achieved position control with varying loads and filled a significant gap in the literature, but their model

is still limited to one particular wire geometry and requires feedback of applied stress which can be difficult to measure in many practical applications. Although SMA's are frequently used in helical spring geometries, only a few studies have investigated the electrical resistance trends in SMA springs [79, 46], and these studies are limited to a particular device. There exists a need for a generalized resistance model for SMA springs that accounts for variable loads and varying geometric parameters while incorporating only quantities that can be easily measured or obtained from material or manufacturer data sheets.

2.2.5 Resistance-based nitinol spring model

Brinson's one-dimensional thermo-mechanical model correlates the applied stress/strain in Nitinol alloys based on the temperature and several material parameters, including four critical transition temperatures, temperature-dependent moduli, and critical stress parameters [23]. The relationship between Brinson's constitutive model and nitinol coil springs in the fully-autenitic and fully-martensitic phases is explained by An et al. [7]. In the models of Brinson and An et al., the fundamental properties that define the nonlinear behavior of shape memory Nitinol are the shear modulus of austenitic Nitinol G_A, the shear modulus of twinned martensitic Nitinol G_M, and the percentage of detwinned martensitic nitinol in the sample ξ_s. In the following, the nitinol coil derivations of An and colleagues are presented and extended by (1) adding a correction term for small spring index coils, (2) presenting an alternative

formulation of the volume fraction of detwinned martensitic nitinol based on measureable parameters, and (3) using electrical resistance as a surrogate for temperature in the model. These modifications allow for predictive modeling and position control of nitinol springs of any geometry without need of temperature, force, or position measurements. This simplification is particularly advantageous for soft robotics applications where loads are variable and the additional weight and complexity of embedded force/position/temperature sensors is undesirable. While this paper includes all the necessary equations and considerations for modeling nitinol springs based on their electrical resistance, both Brinson and An et al. should be credited for the subtleties and methodologies underpinning the proposed model.

Contents and layout

The remainder of this paper begins with a review of relevant principles underlying nitinol phase transformations and electrical resistivity followed by presentation of the spring mechanics model by An et al. with proposed modifications. The application of Brinson's thermo-mechanical model to helical springs by An et al. is then presented along with several critical modifications and extensions for the resistance-based model. Section 2.4 outlines the experimental setup and procedures for characterizing the electro-mechanical properties of the nitinol springs and validating the model with experimental results presented throughout. Section 2.4.6 discusses the implications of the proposed resistance-based model with steps for application to new

spring geometries or different alloys. Key findings are then summarized in Section 2.5.

2.3 Background and modeling

In order to describe the development of the resistance-based nitinol model, we must first lay out the relevant underlying mechanical and electrical principles. We begin by describing the microstructure and phase transformation properties of the alloy, then describe the factors affecting the electrical resistance before presenting the nitinol spring model developed by An et al. [7] and introducing the necessary modifications to this model.

2.3.1 Nitinol phase transformations

The unique properties of nitinol, including the shape-memory effect and pseudo-elasticity, are caused by changes in the crystal structure triggered by different temperature and loading conditions, as shown in Figs. 2.1 and 2.2. At cold temperatures, prior to applying stress, nitinol exists in the twinned martensite phase. This phase consists of a monoclinic crystal structure with twin boundaries (mirrored interfaces between atomic planes). As stress is applied to the twinned martensite, the bonds stretch and the material deforms elastically (Figure 2.2 region 1).With further application of stress, a detwinning process occurs where atomic planes are aligned into an ordered monoclinic structure. This realignment causes a pseudo-plastic deforma-

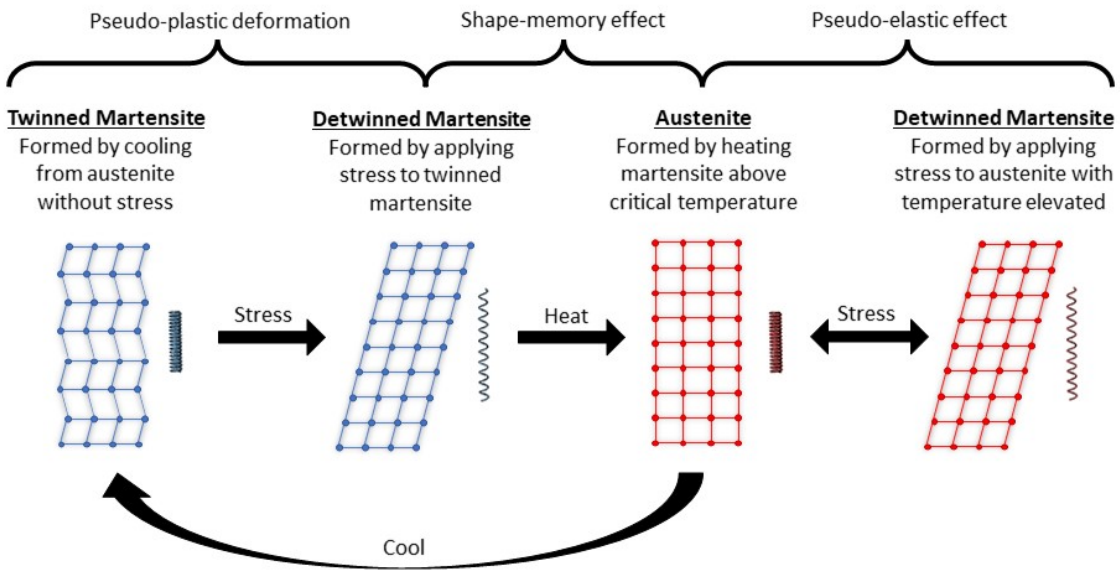

Figure 2.1: Nitinol phase transformations.

tion region as the stress/strain curve flattens during the detwinning process (Figure 2.2 region 2). Because the detwinned martensite is thermodynamically stable at low temperatures, it does not "re-twin" and follow the same path upon unloading, but rather recovers only a small elastic strain. After detwinning, the unloading path (Figure 2.2 region 4) follows a line roughly parallel to the elastic loading curve, retaining a pseudo-plastic strain of up to 6-8% (Figure 2.2 point 5). Unlike a true plastic deformation, this residual strain can be recovered upon heating above a critical transformation temperature at which point the material assumes a cubic crystal structure as it transforms to the high-temperature phase, austenite. This transformation occurs over a range of temperatures; it begins transforming at the austenite

start temperature A_s and is completely austenitic when the austenite finish temperature A_f is reached. When martensitic Nitinol transforms to austenite, it returns to its original, shape-set cubic crystal structure, regardless of whether the martensite was previously deformed (detwinned). This attribute enables the shape-memory effect, allowing residual pseudo-plastic strains to be recovered when heated above the transition temperature (Figure 2.2 region 6).

The high-temperature phase, austenite, has a much higher stiffness than the martensite phase. When stress is applied to the austenitic nitinol, it follows a steep elastic loading curve as the bonds are stretched (Figure 2.2 region 7). When a critical stress is reached, detwinned martensite begins to form due to the applied stress (Figure 2.2 region 8). This phase is often referred to as stress-induced martensite, although it is identical in structure to the detwinned martensite formed at low temperatures in region 2 from Figure 2.2. However, the martensite phase is unstable at temperatures above the transition temperature, so it reverts immediately back to austenite upon unloading. As a result, the high temperature nitinol retraces the same path back to zero strain when unloaded (Figure 2.2 regions 7 and 8). This effect is known as pseudo-elasticity where the material can recover substantial strain—even beyond the elastic limit—due to the reversible conversion between austenite and stress-induced martensite. When cooled in the absence of stress, the austenite transforms back to twinned martensite, beginning at the martensite start temperature M_s until the

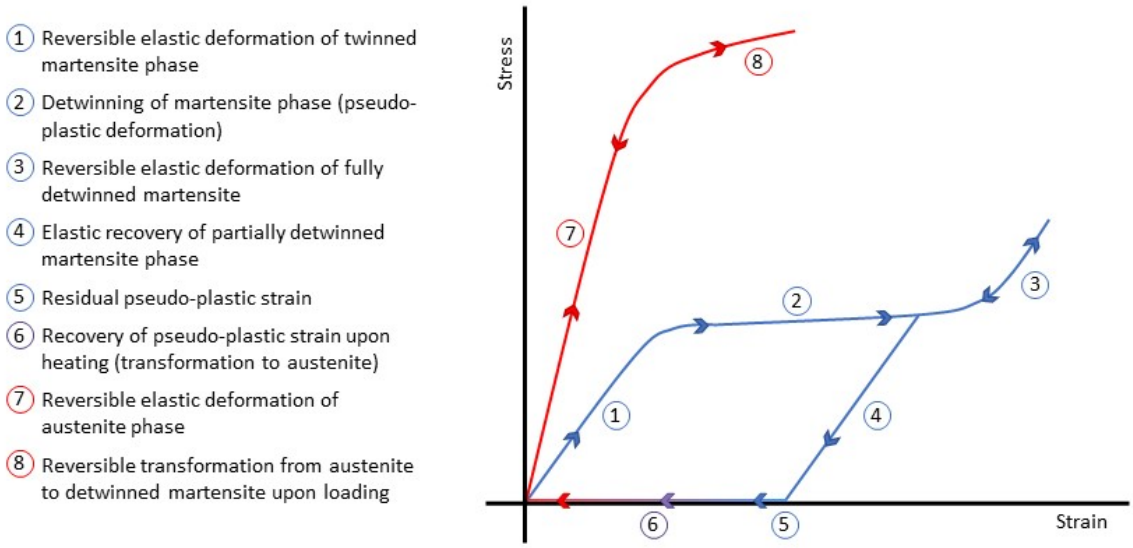

Figure 2.2: Stress/strain diagram of nitinol phase transformations.

martensite finish temperature M_f is reached. Although the transition between the high- and low-temperature phases of nitinol is technically defined by four transition temperature parameters (A_s, A_f, M_s, and M_f) which form a hysteresis loop, these critical temperatures are often lumped into a single transition temperature listed by the manufacturer which represents the temperature at the center of the transformation hysteresis loop or the average temperature at which transformation occurs.

2.3.2 Electrical resistivity in metallic materials

In order to understand the relationship between temperature and resistance in nitinol, one must first recall the fundamental mechanism by which electrical current flows through metallic materials. In solid metals, cations are arranged in an organized

crystal structure that is surrounded by a "sea" of electrons. Conduction occurs when electrons travel from one side of the material to another; resistivity is the resistance to the flow of electrons through the material.

As shown in Figure 2.3, several factors affect the resistivity of metallic materials, including temperature, geometry, microstructure, plastic deformation, and elastic deformation. Increasing temperature causes the electrical resistivity to increase due to increased electron-phonon scattering [100]. As heat is added to a metal, vibrations of the atomic lattice intensify, thus increasing the number of collisions between phonons and electrons, which reduces the mean free path for electron travel. The resistivity is inversely proportional to the cross-sectional area, so any decrease in geometric parameters—such as thinning of a wire as it is stretched—cause the resistance to increase. The microstructural arrangement of atoms certainly affects the resistivity. Most metals have only a single solid phase, but some unique materials—such as iron, carbon, and shape memory alloys—can transition between multiple solid phases. Crystal structures with regularly-spaced ions and straight channels offer direct pathways for electrons and thus promote conductivity, whereas zig-zagged structures have tortuous electron pathways with higher resistance to electron flow due to lattice scattering [152]. As plastic deformation occurs, the formation of dislocations further obstructs the pathways for electron travel as lattice imperfections increase electron scattering, causing increased resistivity with higher levels of plastic deformation. Fi-

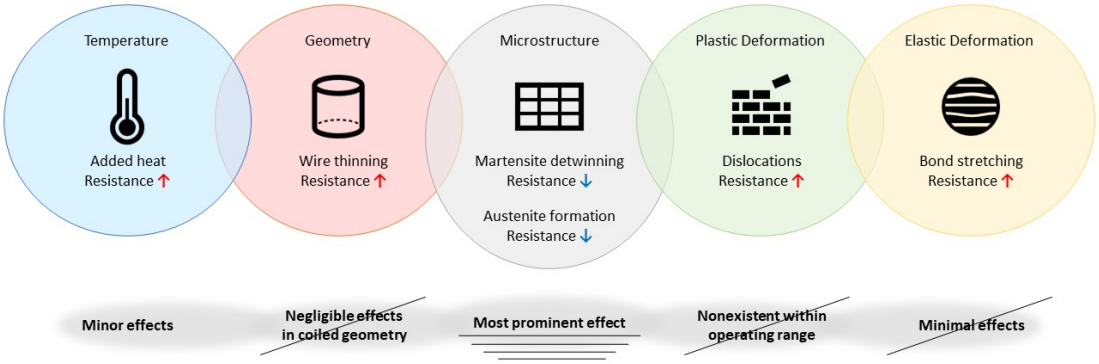

Figure 2.3: Factors affecting nitinol resistivity.

nally, the stretching of chemical bonds during elastic deformation tends to cause a slight increase in resistivity as the alignment of conductive pathways is disrupted.

When considering specifically a coiled shape-memory alloy such as Nitinol, some of the above-mentioned factors are more significant than others. In a coiled geometry, there is no significant change in cross-sectional area as the spring is stretched, provided that it is not pulled to the point of becoming completely straight. Some elastic deformation (bond stretching) does occur prior to the formation of detwinned martensite, but this has minimal effect on the material's resistivity. True plastic deformation causes permanent damage to the material and is generally avoided by placing stress or strain limits on the operating range. Temperature affects the electrical resistance of the nitinol springs in two ways: (1) as mentioned before, added heat increases vibration and collisions with electrons, causing a slight increase in resistance, and (2) heating nitinol above its critical transition temperature instigates a phase transformation from martensite to austenite. The latter causes a dramatic

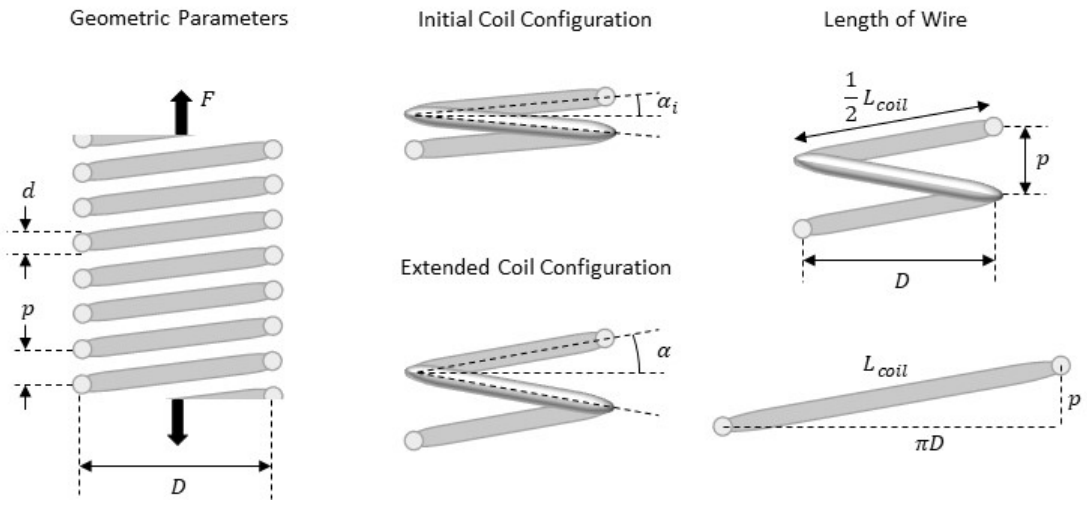

Figure 2.4: Helical spring coil parameters.

drop in resistance as the crystal structure changes from monoclinic to cubic upon heating (or vice versa upon cooling below the transition temperature). The change in microstructue between the three phases – twinned martensite, detwinned martensite, and austenite – has the most prominent effect on resistivity variation and is thus the primary focus of this analysis. The twinned martensite phase has the highest resistivity due to the twin boundaries between atomic planes; the austenite and detwinned martensite phases have much lower resistivities.

The resistance R measured experimentally from a particular spring sample should be normalized by dividing by the total length of wire L to obtain the resistivity or resistance per unit length: $\rho = R/L$. The length of wire can be computed by evaluating a single coil laid flat as shown on the right side of Figure 2.4. The length

of a single coil is simply the hypotenuse of the triangle:

$$L_{coil} = \sqrt{(\pi D)^2 + p_i^2}, \tag{2.1}$$

where p_i is the initial pitch or distance between centers of consecutive coils. The total length of wire is then found by multiplying by the number of coils n; hence,

$$\rho = \frac{R}{n\sqrt{(\pi D)^2 + p_i^2}} \tag{2.2}$$

can be used to normalize resistance measurements.

2.3.3 Helical spring mechanics for large deformation

Nitinol and other shape-memory alloys are used primarily in two geometries: straight wire and helical springs. While straight wire is simple to form and supports higher loads, coiled geometries offer significantly higher stroke as a relatively small material strain corresponds to a large spring strain. Nitinol springs are formed by wrapping a straight wire tightly around a mandrel, then performing a heat treatment procedure to set the shape in the desired coiled geometry. The shape-setting heat treatment establishes the cubic crystal structure configuration that the alloy will revert to—or "remember"— each time it is heated above the transition temperature.

Spring mechanics model by An et al.

While characterization studies on straight wire can be easily scaled for different wire diameters, normalizing the force and strain in a spring requires more advanced analysis of the spring geometry and internal forces/bending moments. Factors such as coil angle and spring diameter reduction are typically neglected in standard mechanical spring analysis as their effects are negligible at small strains. However, these factors have substantial effects in SMA springs which can be designed for higher strains due to their ability to recover pseudo-plastic strains up to 6-8%. An et al. included these effects in [7] where the relationships between force/shear stress and coil angle/shear strain are explored in detail. The equations developed by An et al. are presented below, and the spring coil geometric parameters used for this analysis are shown in Figure 2.4.

First, the spring elongation δ as a function of the coil angle α can be written as

$$\delta(\alpha) = \frac{\pi n D_i}{\cos \alpha_i}(\sin \alpha - \sin \alpha_i), \tag{2.3}$$

where n is the number of coils, D_i is the initial mean spring diameter, and α_i is the initial coil angle. The spring force in the elastic region is then expressed in terms of α as

$$F(\alpha) = \frac{\pi d^4}{8 D_i^2} G \frac{\cos^2 \alpha_i (\sin \alpha - \sin \alpha_i)}{\cos^2 \alpha \left(\cos^2 \alpha + \sin^2 \alpha / [1 + \nu]\right)}, \tag{2.4}$$

where d is the spring wire diameter, and G and ν are the material's shear modulus and Poisson's ratio, respectively. The commonly-accepted Poisson's ratio for nitinol is $\nu = 0.33$ as reported by An et al [7]. Note that Eq. 2.4 only applies to the linear elastic regions for either martensitic or austenitic nitinol. The shear stress is then computed from the applied force using

$$\tau(F) = \frac{F(\alpha)\frac{D_i}{2}\frac{d}{2}}{J} = \frac{8CF(\alpha)}{\pi d^2}, \tag{2.5}$$

where C is the ratio of the coil diameter to wire diameter $C = D/d$, called the spring index. Equation 2.5 accounts for the spring diameter reduction, but does not account for the curvature effects and the force due to direct shear. A modification is proposed later using the Wahl factor to improve the accuracy of this result.

The shear strain γ is expressed in terms of the spring index C, Poisson's ratio ν, and coil angle α as

$$\gamma(\alpha) = \frac{1}{C}\frac{\cos^2\alpha_i(\sin\alpha - \sin\alpha_i)}{\cos^2\alpha\left(\cos^2\alpha + \sin^2\alpha/[1+\nu]\right)}. \tag{2.6}$$

Modification and extension of An spring model

As mentioned before, the An et al. model neglects the effects of curvature and direct shear in the relationship between force and shear stress. A simple modification to Eq. 2.5 can be made by adding the Wahl correction factor W in the shear stress equation

to account for the direct shear and curvature effects [180]:

$$W = \frac{4C-1}{4C-4} + \frac{0.615}{C}, \tag{2.7}$$

$$\tau(F) = \frac{8CWF(\alpha)}{\pi d^2}, \tag{2.8}$$

$$F(\tau) = \frac{\pi d^2 \tau}{8CW}, \tag{2.9}$$

where C is again the spring index. The effects of curvature on the shear stress become nontrivial when the spring index is small [ref Mechanical Springs, Wahl, 1944]. This is often the case in the design of SMA springs, especially for compact, high-force applications, so the Wahl factor should not be neglected when converting spring force to shear stress or vice-versa using Eqs. 2.8 and 2.9.

A second extension is made to the An et al. model in order to relate the material shear strain with the spring strain. First, we relate the coil angle α to the spring pitch p:

$$\alpha(p) = \tan^{-1}\left(\frac{p}{2D}\right). \tag{2.10}$$

The spring pitch can then be expressed in terms of the initial pitch p_i and the spring elongation δ or the spring strain ϵ:

$$p(\delta) = p_i + \frac{\delta}{n}, \tag{2.11}$$

$$p(\epsilon) = p_i(1+\epsilon). \tag{2.12}$$

Combining Eqs. 2.10 and 2.12 gives the coil angle as a function of spring strain:

$$\alpha(\epsilon) = \tan^{-1}\left(\frac{p_i}{2D}(1+\epsilon)\right). \tag{2.13}$$

Combining Eqs. 2.6 and 2.13 gives the following relationship between the spring strain and material shear strain:

$$\gamma(\epsilon) = \frac{1}{C}\frac{\cos^2\alpha_i(\sin[\alpha(\epsilon)]) - \sin\alpha_i)}{\cos^2[\alpha(\epsilon)]\left(\cos^2[\alpha(\epsilon)] + \sin^2[\alpha(\epsilon)]/[1+\nu]\right)}, \tag{2.14}$$

where the initial coil angle can be computed from the initial pitch p_i or the initial spring length L_0 using the following equations:

$$\alpha_i = \tan^{-1}\left(\tfrac{p_i}{2D}\right), \tag{2.15}$$

$$\alpha_i = \tan^{-1}\left(\tfrac{L_0}{2nD}\right). \tag{2.16}$$

Thus, the shear strain as a function of spring strain can be simplified to

$$\gamma(\epsilon) = \frac{h\left(\frac{p_i(1+\epsilon)}{\sqrt{h}} - \frac{p_i}{\sqrt{h_i}}\right)}{C\,h_i\left(\frac{4D^2}{h} + \frac{p_i^2(1+\epsilon)^2}{h(1+\nu)}\right)}, \tag{2.17}$$

where

$$h = 4D^2 + p_i^2(1+\epsilon)^2, \tag{2.18}$$

$$h_i = 4D^2 + p_i^2. \tag{2.19}$$

Using these modifications to the SMA spring model developed by An et al., the coil angle α can be used to relate the spring force and spring strain with their normalized counterparts shear stress and shear strain, respectively. Equations 2.8 and 2.17 can be used to normalize the spring force and spring strain measured from a particular geometry such that results may be applied to other spring geometries. Equation 2.9 and the reverse of Eq. 2.17 can then be used to compute the resulting spring force and spring strain for a different geometry from a normalized model, provided that the spring wire diameter and heat treatment are identical. These relationships are shown in Figure 2.5 where the solid blue curves are computed according to the geometric parameters from the springs used in the present experiments.

2.3.4 Nitinol spring force model

Brinson-An nitinol spring model

The Brinson thermomechanical model can be used to accurately describe the stress-strain relationship for 1-dimensional loading of nitinol based on the underlying thermodynamics and phase transformation kinetics [23, 22]. An et al. extended the

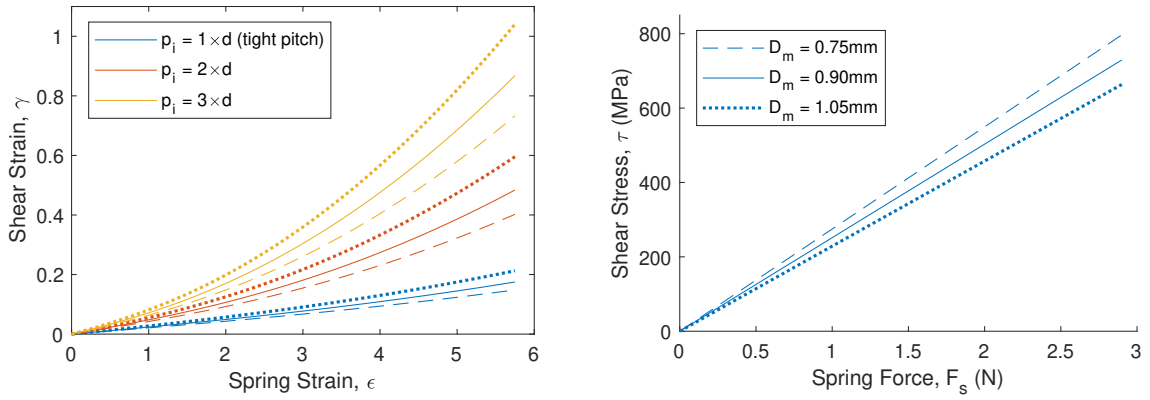

(a) Normalization of spring strain

(b) Normalization of spring force

Figure 2.5: Conversion from geometry-specific spring strain and spring force to normalized material shear strain and shear stress. Dotted and dashed lines show the effects of different mandrel diameters with the same 0.25mm wire diameter; different colors represent the effect of the initial spring pitch (based on shape-setting)

Brinson model and applied it to Nitinol springs at the two extremes: fully austenitic and fully martensitic nitinol. The model of Brinson and An et al. relies on the shear modulus of the austenitic nitinol G_a, the shear modulus of the martensitic nitinol G_m, the percent detwinned martensite ξ_s, the four critical transformation temperatures A_s, A_f, M_s, and M_f, and several critical stresses defining the start and end of the detwinning process in both the high- and low-temperature phases. The Brinson-An model is presented below, followed by several modifications/extensions to account for nonlinear formation of detwinned martensite from the austenite phase and incorporate resistance as a surrogate for temperature in the existing model.

A linear relationship is expected between the shear stress and shear strain within

the range of elastic deformation. Thus, we can expect

$$\tau = G\gamma \tag{2.20}$$

to hold true for small deformations, where the slope or shear modulus is dependent on the temperature and hence phase, such that

$$\tau = G_a\gamma \qquad T > A_f \tag{2.21}$$

$$\tau = G_m\gamma \qquad T < M_f \tag{2.22}$$

Departure from the linear elastic behavior occurs when the twinned martensite begins detwinning at some critical stress. This nonlinear detwinning process is described by An et al. by adding a second term to Eq. 2.22, which gives

$$\tau = G_m\gamma - G_m\gamma_L\xi_s. \tag{2.23}$$

Here the deviation from the linear elastic model is a function of the percentage of detwinned martensite ξ_s. The parameter γ_L represents the maximum residual strain, in other words, the maximum pseudo-plastic strain which can be achieved if the martensite is 100% detwinned. The Brinson-An model only considers the linear elastic region of the austenite phase, so Eq. 2.21 is used to model this linear behavior without

need of a second term. However, many SMA devices operate beyond this range, delving in to the pseudo-elastic region where the austenite converts to detwinned martensite under sufficient stress. A modification is proposed in the following section to account for the nonlinear formation of stress-induced martensite at temperatures above A_f.

An et al. express the percentage of detwinned martensite as a function of the shear stress in the spring and the critical stresses at which point detwinning starts and finishes:

$$\xi_s = f(\tau, \tau_s^{cr}, \tau_f^{cr}). \tag{2.24}$$

In most devices, however, the axial forces/shear stresses in the coils cannot be easily measured or controlled. Instead, most control algorithms center around strain or spring displacement as a control input. Given the sensory systems typically employed in SMA devices, it makes sense to express this quantity in manner that is more easily implemented. This proposed modification is discussed further in the following section.

Model modifications

The work presented by An et al. thoroughly outlines the application of the Brinson model to SMA springs that are fully austenitic or fully martensitic [7, 23, 22]. While this paper is useful for basic SMA spring selection, further extensions are needed to model Nitinol springs in all regions of temperature/deformation using independent

variables that can be easily measured and incorporated in feedback control algorithms. These modifications are proposed in the following sections.

Distinction between martensite phases. First, the model by An et al. only considers the case of 100% austenitic or 100% martensitic nitinol. While this simplification is sufficient for determining the stress-strain behavior at both extremes, the behavior between these bounding curves significantly affects the response of many SMA devices. Since the cycling time for SMA's is notoriously slow, much time is spent in this "middle region," even for devices designed to be used in the on/off regions alone. Thus, it is worth characterizing the stress-strain behavior under conditions that cuase the simultaneous existence of both the austenite and martensite phases.

Shape-memory alloy constitutive models—such as those developed by Boyd and Lagoudas [20], Liang and Rogers [99], and Brinson [23, 22]—rely on internal variables such as the martensite fraction ξ to characterize the phase transformation kinetics. These internal variables were first introduced by Tanaka and Nagaki [173]. Brinson proposed and justified the separation of the martensite fraction into two components to distinguish between temperature-induced (twinned) martensite ξ_t and stress-induced (detwinned) martensite ξ_s [23]. Still, at intermediate temperatures where both martensite and austenite phases are present, the use of ξ_t and ξ_s fails to distinguish between the detwinned martensite that is formed from austenite vs. that

Table 2.1: Variable names and definitions.

Variable	Definition
ξ_0	Fraction of nitinol that would be martensite if unstressed (temperature-dependent)
ξ_{s_m}	• Fraction of ξ_0 that is detwinned due to applied stress (stress-dependent)
$\xi_{t_m} = 1 - \xi_{s_m}$	• Fraction of ξ_0 that remains twinned (stress-dependent)
$\alpha_0 = 1 - \xi_0$	Fraction of nitinol that would be austenite if unstressed (temperature-dependent)
ξ_{s_a}	• Fraction of α_0 that is converted to detwinned martensite due to applied stress (stress-dependent)
$\alpha_a = 1 - \xi_{s_a}$	• Fraction of α_0 that remains austenitic (stress-dependent)
G_m	Shear modulus of low-temperature nitinol ($\xi_0 = 1$)
G_a	Shear modulus of high-temperature nitinol ($\xi_0 = 0$)
γ_L	Maximum residual strain with fully detwinned martensite ($\xi_0 \xi_{s_m} = 1$)
ρ_m	Resistivity function for low-temperature nitinol ($\xi_0 = 1$)
ρ_a	Resistivity function for high-temperature nitinol ($\xi_0 = 0$)
P_{m_t}	Resistivity of twinned martensite phase ($\xi_0 \xi_t = 1$)
P_{m_s}	Resistivity of detwinned martensite phase ($\xi_s = 1$)
P_a	Resistivity of austenite phase ($\alpha_0 \alpha = 1$)

which is formed by detwinning of the twinned martensite phase. Although these two phases have exactly the same aligned monoclinic crystal structure, one is thermodynamically unstable and reverts back to austenite when unloaded. For this reason, a further distinction is proposed by introducing the internal variables ξ_{s_a} and ξ_{s_m}.

The variables used in the proposed model are described in Table 2.1. The onset martensite volume fraction ξ_0 represents the percentage of nitinol that would exist in the martensite phase at a particular temperature under zero stress conditions. The complement of ξ_0 is the onset austenite fraction $\alpha_0 = 1 - \xi_0$, which describes the percentage of nitinol that would exist in the austenite phase at a particular temperature under zero stress conditions. Note that α_0 also includes any fraction of

the material that has been converted to detwinned martensite due to applied stress. For example, at temperatures above A_f, $\xi_0 = 0$ and $\alpha_0 = 1$. However, this does not necessarily imply that the material is 100% austenitic as some amount of α_0 may exist as detwinned martensite, depending on the applied stress. The internal variables ξ_0 and α_0 then are functions of temperature alone. Meanwhile, the variables ξ_{s_a} and α represent the fraction of α_0 that manifests as detwinned martensite (due to applied stress) or remains austenitic, respectively. Similarly, the variables ξ_{s_m} and ξ_t represent the fraction of ξ_0 that is detwinned (due to stress) or remains twinned, respectively. Note that the internal variables $\xi_{s_m}, \xi_t, \xi_{s_a}$, and α have no temperature-dependence but are solely functions of stress (or strain). Drawing these distinctions allows us to more easily separate the effects of stress and temperature in the modeling process.

The proposed internal variables can be easily related back to the internal variables ξ and ξ_s employed by Brinson using the following relationships:

$$\xi_s = \xi_0 \xi_{s_m} + \alpha_0 \xi_{s_a}, \tag{2.25}$$

$$\xi_t = \xi_0 \xi_{t_m}, \tag{2.26}$$

$$\xi = \xi_s + \xi_t = \xi_0 + \alpha_0 \xi_{s_a}, \tag{2.27}$$

$$\alpha = \alpha_0 \alpha_a. \tag{2.28}$$

With the introduction of these internal variables, we can now express the temperature-

dependence of the shear modulus according to the Voigt scheme by expressing G as a function of ξ_0:

$$G(\xi_0) = \xi_0 G_m + [1 - \xi_0] G_a, \tag{2.29}$$

where G_m and G_a are the respective shear moduli of the martensite phase and austenite phase.

Inclusion of pseudo-elastic region. The second proposed modification to the model by An et al. is the inclusion of the pseudo-elastic region. While An et al. accounted for the detwinning of the martensitic nitinol, their model was limited to the linear elastic region of the austenite phase. As a result, this model is limited to relatively low loads and strains at high temperatures. To enable exploitation of the pseudo-elastic region, we propose the addition of a term to the shear stress equation that captures this nonlinearity. Similar to the nonlinear detwinning term in Eq. 2.23, a second term added to Eq. 2.21 causes the necessary flattening of the stress-strain curve as a function of the detwinned martensite fraction ξ_{s_a}. Using the internal variables established in Table 2.1, the shear stress at the two extreme temperatures can be expressed as:

$$\tau_{cold} = G_m \gamma - [G_m \gamma_L] \xi_{s_m} \qquad \xi_0 = 1 \tag{2.30}$$

$$\tau_{hot} = G_a \gamma - [G_a \gamma_L] \xi_{s_a} \qquad \xi_0 = 0, \tag{2.31}$$

where ξ_{s_m} and ξ_{s_a} are functions of shear strain γ.

Modeling at transitional temperatures Another extension to the Brinson-An model is the inclusion of transitional temperatures in the stress-strain model. At temperatures between M_f and A_f, the martensite and austenite phases can coexist as the material transitions from one phase to the other. While the An model focused exclusively on the extreme cases (100% austenite or 100% martensite), here a phenomenological model is proposed to compute the stress-strain relationship at transitional temperatures by linearly interpolating between the bounding curves using ξ_0 as the interpolation variable:

$$\tau(\xi_0) = \xi_0 \tau_m + [1 - \xi_0]\tau_a, \tag{2.32}$$

$$\tau(\xi_0) = \underbrace{G(\xi_0)}_{\substack{\textit{linear} \\ \textit{elastic}}} - \underbrace{\xi_0[G_m\gamma_L]\xi_{s_m}}_{\substack{\textit{nonlinear} \\ \textit{martensite} \\ \textit{detwinning}}} - \underbrace{[1-\xi_0][G_a\gamma_L]\xi_{s_a}}_{\substack{\textit{nonlinear conversion} \\ \textit{from austenite to} \\ \textit{detwinned martensite}}}, \tag{2.33}$$

where ξ_{s_m} and ξ_{s_a} are functions of shear strain, as discussed in the following section. Note that substituting $\xi_0 = 1$ and $\xi_0 = 0$ in Eq. 2.33 yields the same results as Eqs. 2.30 and 2.31 for the cases of 100% martensite and 100% austenite, respectively.

Percent detwinned martensite from shear strain. Another important modification to the Brinson-An model is made to represent the detwinned martensite fractions ξ_{s_m} and ξ_{s_a} as functions of shear strain. In the Brinson-An model, the per-

centage of detwinned martensite is defined as a function of critical stresses and the current stress, as shown in Eq. 2.24 [7]. However, these fractions can alternatively be defined as a function of the shear strain by rearranging Eqs. 2.30 and 2.31 to solve for the detwinned martensite fractions formed from martensite and from austenite, respectively:

$$\xi_{s_m} = \frac{G_m \gamma_{cold} - \tau_{cold}}{G_m \gamma_L}, \tag{2.34}$$

$$\xi_{s_a} = \frac{G_a \gamma_{hot} - \tau_{hot}}{G_a \gamma_L}. \tag{2.35}$$

By collecting shear stress versus shear strain data at both a low temperature (below M_f) and a high temperature (above A_f), these functions can be determined for a particular nitinol alloy. Experimental results and sigmoidal fits to ξ_{s_m} and ξ_{s_a} for two different alloys are presented in the experimental results section.

Martensite fraction from resistivity. The last and most significant extension to the Brinson-An model is the incorporation of electrical resistivity as a surrogate for temperature. Brinson's model relies heavily on temperature for the phase transformation kinetics. Temperature is the main driving force behind the transformation between martensite and austenite phases and thus plays an important role in nitinol constitutive models. However, changes in electrical resistivity also evidence changes between phases.

Nitinol has a different electrical resistivity in each of the three phases—twinned martensite, detwinned martensite, and austenite. The resistivities in these phases are denoted as P_{m_t}, P_{m_s}, and P_a, respectively. While other factors such as temperature and elastic deformation can affect resistivity within any of the three phases, these other factors are relatively minor—less than 6% compared to the dramatic effects of phase changes. Thus, we consider these values to be constant, such that any change in resistance is attributed to a phase change.

In the previous section, we showed how $\xi_{s_m}(\gamma)$ and $\xi_{s_a}(\gamma)$ could be obtained from mechanical testing at two extreme temperatures. If resistance is also measured during these tests, the resistivity as a function of percent detwinned martensite can also be determined for both extremes, such that

$$\rho = \rho_m(\xi_s) \qquad \xi_0 = 1 \tag{2.36}$$

$$\rho = \rho_a(\xi_s) \qquad \xi_0 = 0, \tag{2.37}$$

where $\rho_m(\xi_s)$ is sigmoidal and $\rho_a(\xi_s)$ is linear. By interpolating between these two curves, a surface is obtained that represents the resistivity of the nitinol as a function of ξ_0 and ξ_s, as shown in Figure 2.6.

A linear interpolation between these two curves would take the form

$$\rho(\xi_0, \xi_s) = \xi_0 \rho_m(\xi_s) + [1 - \xi_0]\rho_a(\xi_s). \tag{2.38}$$

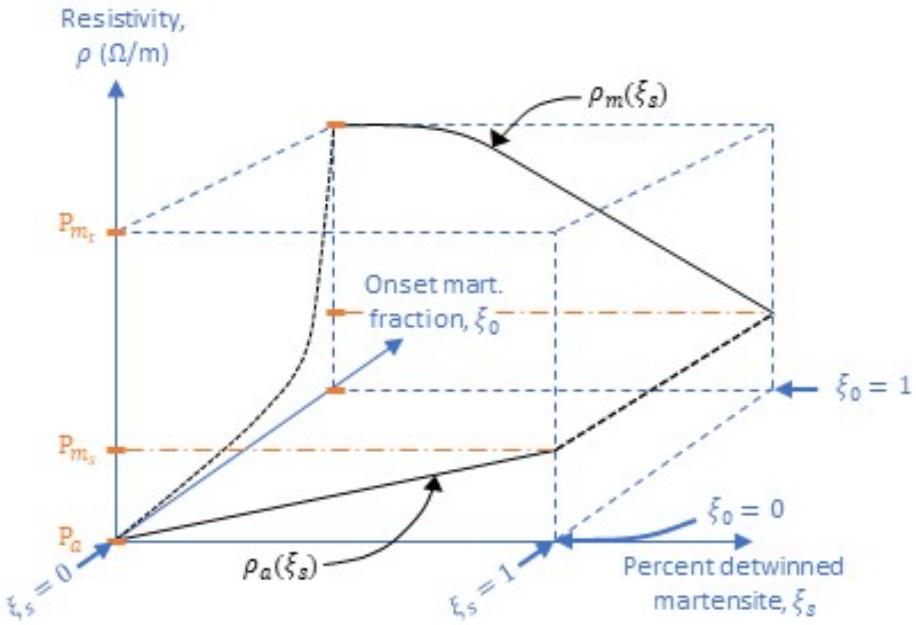

Figure 2.6: Resistivity variation between phases.

Or, since ξ_s are functions of γ, we can write the linear interpolation as

$$\rho(\xi_0, \gamma) = \xi_0 \rho_m(\xi_{s_m}(\gamma)) + [1 - \xi_0]\rho_a(\xi_{s_a}(\gamma)). \tag{2.39}$$

However, in reality, the resistivity does not scale linearly with ξ_0 between the two bounding curves. When multiple phases are present, the different crystal structures interact at boundary layers in an unpredictable manner. In some cases, good alignment of atomic planes may preserve electron pathways across a boundary between two phases. In other cases, the interaction between phases may result in severe misalignment that causes the electrical resistance to spike.

In this work, we propose an interpolation function $A(\xi_0, \gamma)$ that accounts for this phenomenological interaction between the electrical resistivity of multiple phases. A is a power law function of ξ_0 and becomes linear as $\gamma \to \gamma_{max}$. Using A, we can rewrite Eq. 2.39 as

$$\rho(\xi_0, \gamma) = A(\xi_0, \gamma)\rho_m(\xi_{s_m}(\gamma)) + [1 - A(\xi_0, \gamma)]\rho_a(\xi_{s_a}(\gamma)), \tag{2.40}$$

where the interpolation function A takes the form

$$A(\xi_0, \gamma) = \xi_0^{a+[1-a][\gamma/\gamma_{max}]^b}, \tag{2.41}$$

and γ_{max} is the shear strain corresponding to $\xi_s = 1$. Note that the interpolation function A satisfies the following conditions:

$$A(0, 0) = 0, \tag{2.42}$$

$$A(1, 0) = 1, \tag{2.43}$$

$$A(\xi_0, \gamma_{max}) = \xi_0, \tag{2.44}$$

$$A(\xi_0, 0) = \xi_0^a. \tag{2.45}$$

The constants a and b are determined using a least squares fit to shear stress versus shear strain data measured at an intermediate temperature where $\xi_0 \neq 0$ and $\xi_0 \neq 1$.

The values of a and b, optimized from two different nitinol alloys, are presented in the experimental results section.

The onset martensite fraction ξ_0 can then be determined directly from the resistivity and shear strain by rearranging Eq. 2.40

$$A(\rho,\gamma) = \frac{\rho - \rho_a(\xi_{s_a}(\gamma))}{\rho_m(\xi_{s_m}(\gamma)) - \rho_a(\xi_{s_a}(\gamma))} \tag{2.46}$$

to solve for A, then converting A to ξ_0 by reversing Eq. 2.41:

$$\xi_0(A,\gamma) = A^{(a+[1-a][\gamma/\gamma_{max}]^b)^{-1}}. \tag{2.47}$$

Alternatively, Eqs. 2.46 and 2.47 can be combined to solve for ξ_0 directly using

$$\xi_0(\rho,\gamma) = \left[\frac{\rho - \rho_a(\xi_{s_a}(\gamma))}{\rho_m(\xi_{s_m}(\gamma)) - \rho_a(\xi_{s_a}(\gamma))}\right]^{\left(a+[1-a][\gamma/\gamma_{max}]^b\right)^{-1}}. \tag{2.48}$$

Note that temperature is not included in Eq. 2.48. Although ξ_0 is strongly correlated to temperature, it can be determined entirely from resistivity and shear strain.

Finally, combining Eqs. 2.33 and 2.48 gives the relationship between shear stress and shear strain for any resistivity:

$$\tau(\rho,\gamma) = G\Big(\xi_0(\rho,\gamma)\Big) - \xi_0(\rho,\gamma)\Big[G_m\gamma_L\Big]\xi_{s_m}(\gamma) - \Big[1-\xi_0(\rho,\gamma)\Big]\Big[G_a\gamma_L\Big]\xi_{s_a}(\gamma), \tag{2.49}$$

where G, ξ_0, ξ_{s_m}, and ξ_{s_a} are found from Eqs. 2.29, 2.48, 2.34, and 2.35, respectively.

2.4 Characterization from measured data

The model proposed in the previous section relies on several experimentally-determined functions and parameters, including the detwinning and resistance profiles at both a high and a low temperature, as well as the interpolation parameters that describe the interaction between phases in the overall resistivity at transitional temperatures. By observing the behavior at both extremes ($\xi_0 = 0$ and $\xi_0 = 1$), the behavior at intermediate temperatures can be determined if the resistivity is known. The procedure for measuring these profiles and parameters is outlined in the sections below, with results presented in normalized form such that they may be applied to springs of different geometries without having to repeat the characterization process described below.

2.4.1 Experimental setup

Characterizing the thermo-electro-mechanical properties of nitinol springs requires a robust experimental setup capable of simultaneously measuring and controlling the temperature, resistance, force, and elongation of the springs.

To measure the mechanical properties, the springs were mounted on a Mark 10 Test Stand fitted with a 25N force gauge. The springs were fixed to the test stand using copper hooks that fit snugly inside the first few coils on each end, as shown in

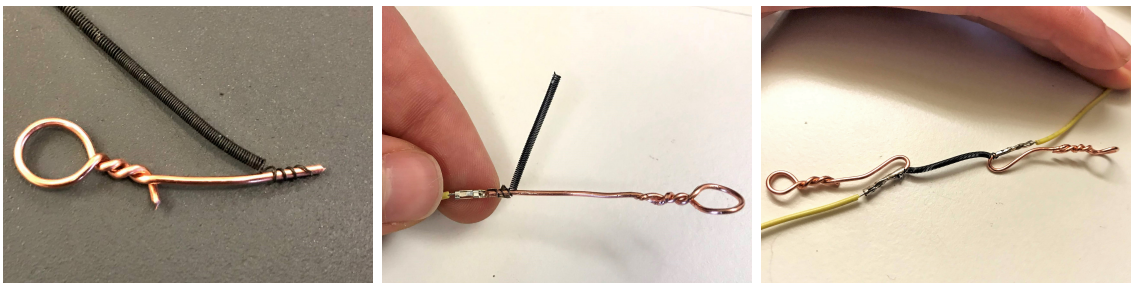

(a) Insertion of copper wire. **(b)** Placement of Molex crimp. **(c)** Formation of copper hooks

Figure 2.7: Process of mounting nitinol springs on copper hooks using Molex crimp terminals to connect electrical wires.

Figure 2.7. The number of active coils is then counted between hooks. The Mark 10 Test Stand allows for control of the travel and strain rate while measuring force and travel simultaneously.

Measuring the temperature of a thin nitinol wire is nontrivial. Traditional temperature sensors such as thermistors, thermocouples, and resistance thermal detectors (RTD's) are typically soldered or mounted with an adhesive directly onto the object whose temperature is to be monitored. Due to the thick oxide layer formed on the surface of the Nitinol where exposed to air, it is nearly impossible to solder or adhere a temperature sensor to the surface of the nitinol springs, especially with the small-scale geometry used in these experiments. Infrared (IR) temperature sensors are an alternative option that does not require constant contact with the nitinol. However, care must be taken to ensure that the IR sensor is focused on the coils themselves, not to the left or right or through gaps in the coils. For these experiments, an IR temperature sensor was mounted to the base of the test stand, pointed at an angle

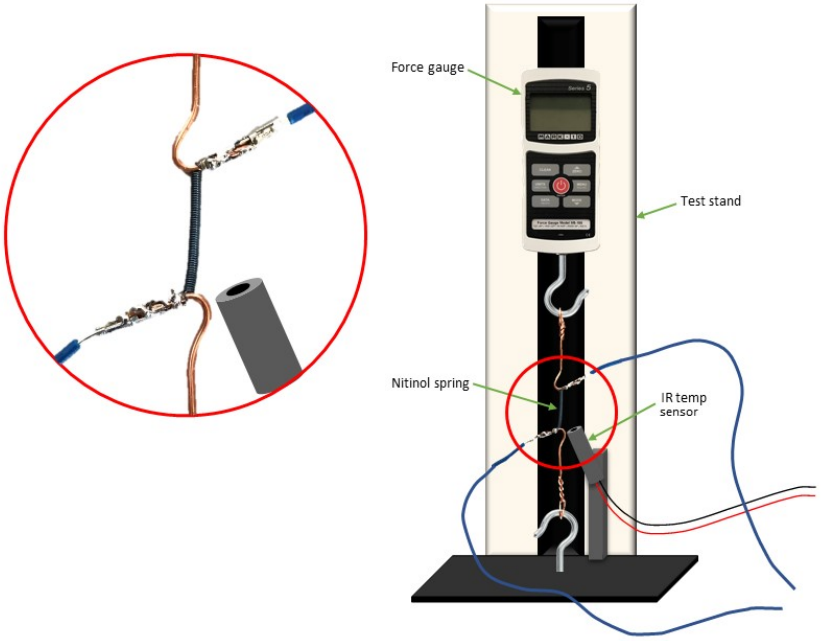

Figure 2.8: Experiment setup for electro-mechanical testing of nitinol springs.

towards the spring, as shown in Figure 2.8. This mounting angle ensures that the coils appeared overlapped from the perspective of the sensor, even when the spring is stretched and gaps are formed between coils.

The most complicated aspect of the experimental setup is the resistance measurement and heating control. An Arduino Mega microcontroller was used to integrate the temperature sensor and resistance measurement circuitry, with the wiring connections shown in Figure 2.9. First, a voltage regulator (LM2941) was used to control the current through the coils via pulse width modulation (PWM). This device supplies whatever voltage is needed to the "OUT" pin such that a constant current determined

by V_{ADJ}/R_{set} flows through the Nitinol spring. This current can be scaled via PWM input to the "ON/OFF" pin of the LM2941. Since the voltage at the "ADJ" pin is constant, measuring the voltage from the "OUT" pin gives the resistance of the nitinol spring from Ohm's Law:

$$R_n = \frac{V_{OUT} - V_{ADJ}}{I} = \frac{V_{OUT} - V_{ADJ}}{V_{ADJ}/R_{set}}. \tag{2.50}$$

For the size and length of springs tested, resistance measurements fall on the order of $3.9 \pm 0.4\Omega$ which causes V_{OUT} to vary only slightly, with values between ~ 2.7 and 3.1 V. In order to measure such small voltage changes, an INA 125 amplifier was connected between V_{OUT} and an offset reference voltage V_{ref} from a simple voltage divider. The amplifier gain was set using a resistor between pins 8 and 9 on the amplifier to maximize the 5V analog range of the microcontroller. External power supplies were used to power both the amplifier and voltage regulator as the Arduino Mega cannot supply sufficient power to heat the springs.

Note that the resistance connot be measured without at least a small current flowing through the nitinol spring. Thus, the duty cycle for heating the coils can never be quite zero. A small trickle current during cooling mode does not significantly slow the cooling process, but a fan is used to help counteract this effect and speed the cooling process.

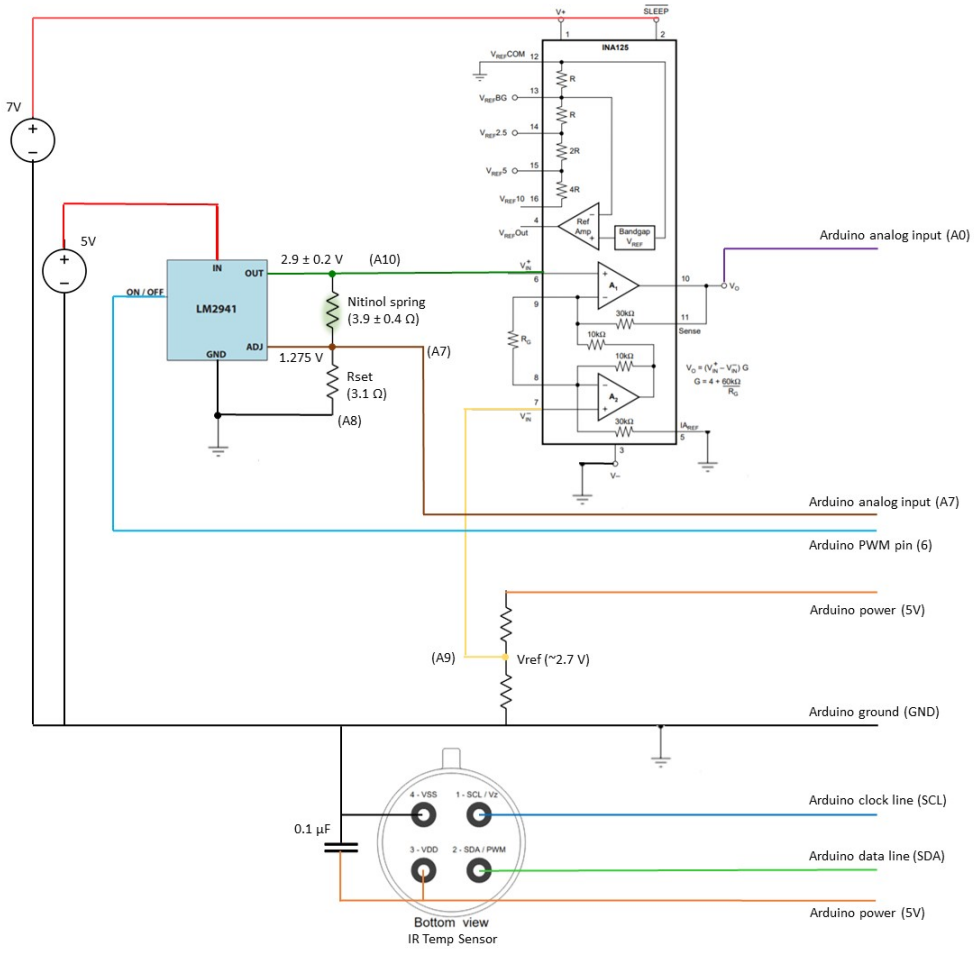

Figure 2.9: Circuit diagram for heating and measuring temperature/resistance of nitinol springs.

2.4.2 Methods

The goal of the experiments conducted was to characterize the thermo-electro-mechanical properties of nitinol springs and develop/validate a phenomenological model based on electrical resistance. Tests were conducted on two different nitinol alloys from Kellog's Research Labs with the same spring geometry: wire diameter $d = 0.25$mm, mandrel diameter $D_m = 0.9$mm, and tight pitch $p_i = 0.269$mm. The transition temperatures of the two alloys were listed as 35° C and 45° by the manufacturer; the critical temperatures M_f, M_s, A_s, and A_f were unknown. Although only a single spring geometry was tested, the results were normalized such that they may be applied to any spring and wire geometry provided that the same alloy composition and heat processing are maintained.

The springs were first held at a fixed length to observe the effects of temperature (and thus phase change) on the resistance of the coils. Next, mechanical tests were conducted on the springs at room temperature while the resistance was monitored. These tests reveal the martensite detwinning profile and the resistivity during this transformation. The same tests were repeated at the highest possible temperature (100% duty cycle) to reveal the austenite to detwinned martensite transformation profile and the associated resistivity. Finally, a PID controller was used to control the heating rate on the coils in order to hold them at constant resistivity during the mechanical testing process. These tests give information about the mechanical

behavior of the springs at intermediate temperatures, and they are used to validate the proposed model.

Each of the mechanical tests followed the same loading pattern, cyclically stretching and relaxing the spring according to the following spring strain sequence: $0\% \rightarrow 115\% \rightarrow 0\% \rightarrow 230\% \rightarrow 0\% \rightarrow 345\% \rightarrow 0\% \rightarrow 460\% \rightarrow 0\% \rightarrow 575\% \rightarrow 0\% \rightarrow 575\%$. At high temperatures, the springs were only stretched up to 345% spring strain so as to prevent permanent damage. These testing processes and results are described in more detail in the following sections.

The proposed model for predicting shear stress as a function of shear strain at each resistivity is then compared with the experimental data using the mean absolute error (MAE) and relative percent difference (RPD) to evaluate the goodness of fit. These error metrics are calculated using the following equations:

$$MAE = \frac{1}{n}\sum_{i=1}^{n} |\tau_{data_i} - \tau_{model_i}|, \tag{2.51}$$

$$RPD = \frac{\sum_{i=1}^{n}(\tau_{data_i} - \tau_{model_i})}{\sum_{i=1}^{n} \frac{1}{2}\left(|\tau_{data_i}| + |\tau_{model_i}|\right)}, \tag{2.52}$$

where n is the number of data points. Note that the relative percent difference is calculated from the difference between the model and experimental data divided by the average magnitude. This quantity is similar to the relative percent error, but is calculated in a way that eliminates divide-by-zero errors.

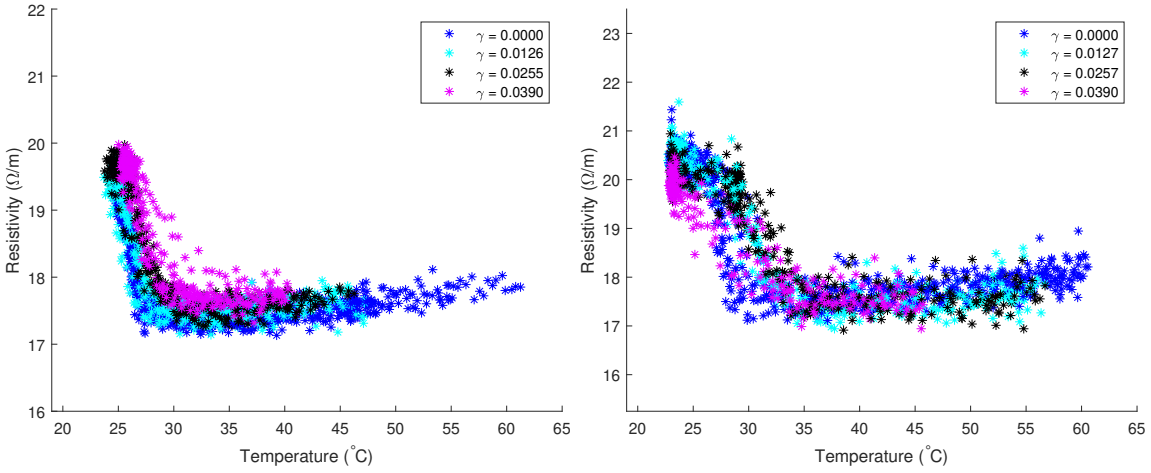

(a) 35°C transition temperature **(b)** 45°C transition temperature

Figure 2.10: Isometric measurements of resistance vs. temperature in two different Nitinol springs.

2.4.3 Temperature-resistance relationship

The temperature-resistance relationship was observed by holding the springs at a fixed length in the test stand while heating them to 60°C, then cooling them with a fan back to room temperature. These tests were repeated three times at four different spring lengths: L_0, $1.5L_0$, $2L_0$, and $2.5L_0$, which correspond to material shear strains of $\gamma = 0$, 0.0125, 0.0255, and 0.0390.

The measured temperature-resistance profiles for each alloy are shown in Figure 2.10. These plots show a sharp drop in resistivity as the nitinol is heated and transitions from martensite to austenite. Following the transformation to austenite, there is a slight increase in resistance as additional heat is added. This slight increase in resistance can be attributed to increased lattice vibrations and collisions with electrons.

However, this effect is minor—especially in the practical temperature range—relative to the substantial change in resistance caused by the phase transformation. The 35°C wire resistivity drops by 2.5 Ω/m between 20 and 30°C due to the phase transformation. Further heating up to 40°C only increases the resistivity by 0.14 Ω/m. Similarly in the 45°C wire, the resistivity drops by 3.5 Ω/m between 22 and 34°C during the phase transformation. Further heating up to 45°C increases the resistivity by 0.20 Ω/m. In both wires, this increase in resistivity due to temperature is less than 6% compared to the drop in resistivity due to phase change.

No significant differences were seen between the heating and cooling paths. However, there is a noticeable flattening of the contour as strain is increased. At zero strain, the resistance drops, then turns a sharp corner becoming abruptly flat following the transformation to austenite. At the higher strain tests, this corner becomes more and more rounded. This feature becomes important when we model the mechanical behavior at intermediate temperatures.

2.4.4 Strain-resistance relationship

The resistance of nitinol is not only a function of temperature, but also depends on strain. Just as an increase in temperature causes a phase transformation from martensite to austenite, so an increase in strain (caused by an applied stress) causes a phase transformation from twinned martensite to detwinned martensite or from austenite to detwinned martensite, depending on the temperature. Figure 2.11 shows the gradual

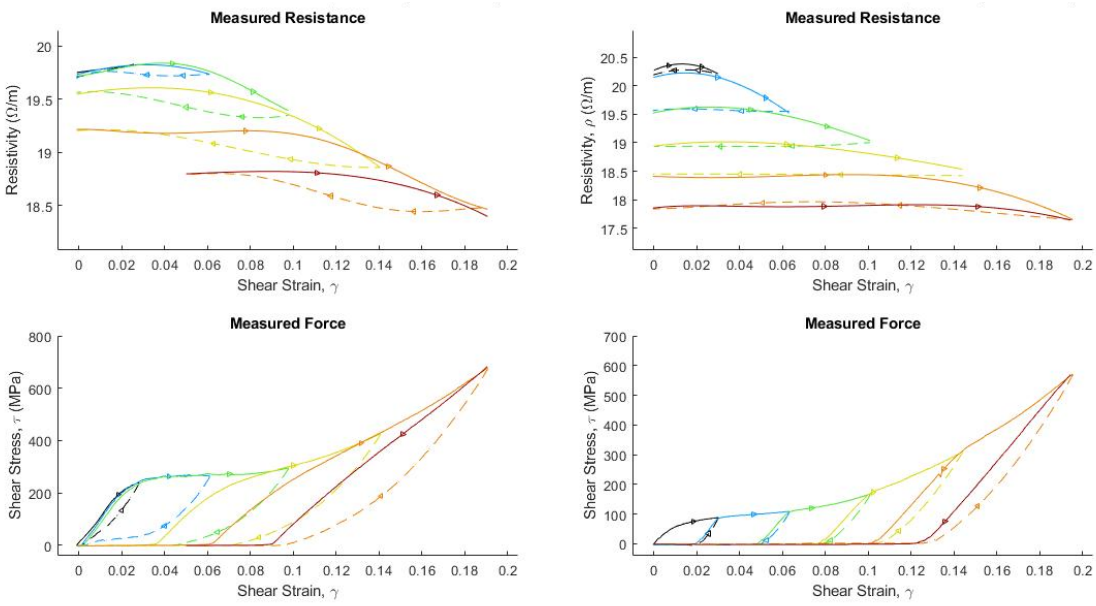

(a) 35°C transition temperature

(b) 45°C transition temperature

Figure 2.11: Isothermal measurements of resistance vs. strain at room temperature in two different nitinol springs.

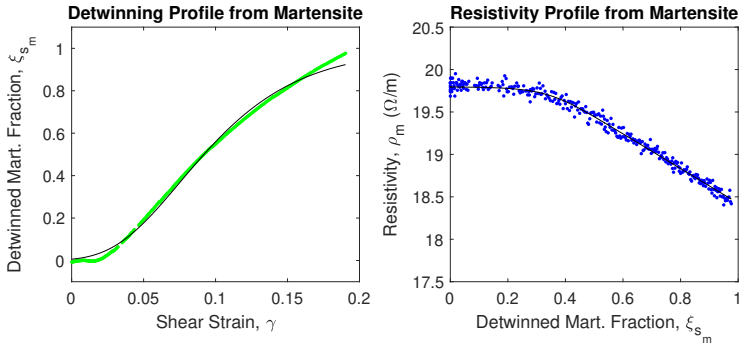

(a) 35°C transition temperature

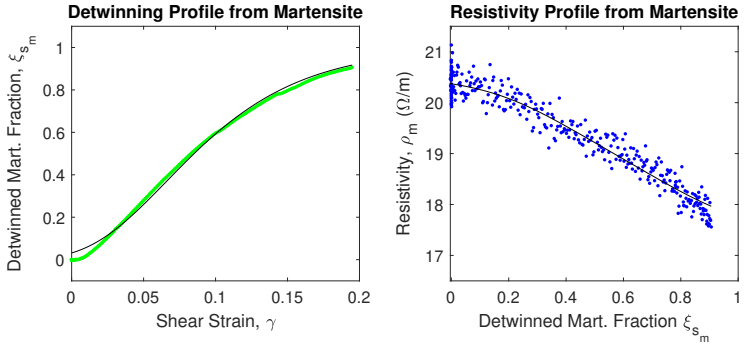

(b) 45°C transition temperature

Figure 2.12: Conversion from twinned to detwinned martensite as a function of shear strain from room temperature test where ξ_0 is assumed to be one (pure martensite when $\gamma = 0$).

drop in resistivity during an increasing cyclic tensile test. As the twinned martensite accumulates psuedo-plastic deformation—caused by martensite detwinning—the resistivity gradually falls off. To quantify the effects of strain on the electrical resistance, we first evaluate the detwinning profile to determine the percent detwinned martensite as a function of shear strain.

A spring of each alloy was tested under the specified increasing cyclic load in the test stand, up to 575% spring strain. This test was conducted at both room

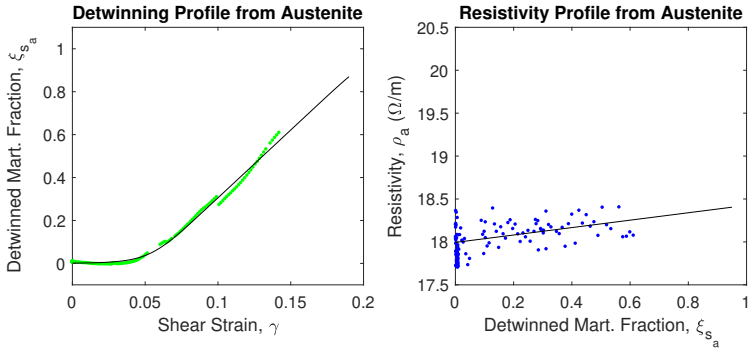

(a) 35°C transition temperature

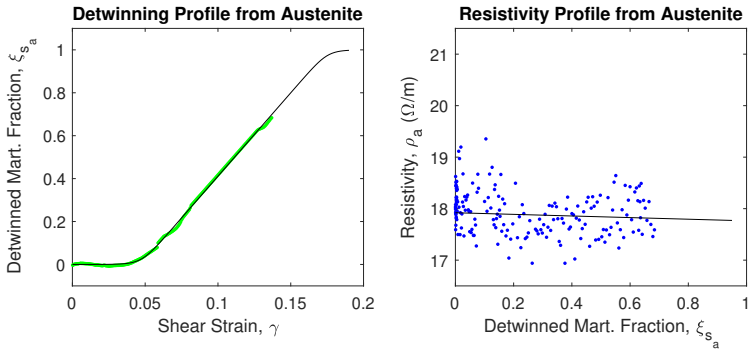

(b) 45°C transition temperature

Figure 2.13: Conversion from austenite to detwinned martensite as a function of shear strain from highest temperature test where ξ_0 is assumed to be zero (pure austenite when $\gamma = 0$).

temperature (no heating) and at maximum temperature (100% duty cycle heating). We assume that the nitinol was 100% martensitic during the room temperature test and 100% austenitic at the start of the high-temperature test. Using Eqs. 2.34 and 2.35, we can then plot the detwinned martensite fraction as a function of shear strain for each alloy at both the hot and cold temperatures. These detwinning profiles are shown on the left-hand side of Figs. 2.12 and 2.13. Generalized logistic sigmoid and algebraic sigmoid curves were fit to the detwinning profiles from the low- and high-temperature tests, respectively. The resistivity versus percent detwinned martensite from the same tests are also shown in Figs. 2.12 and 2.13 on the right-hand side. Algebraic sigmoid and linear functions were fit to resistivity curves from both the low- and high-temperature tests, respectively. These function types were chosen as they track best with the experimental data. The function form and parameters for these curve fits are shown in Table 2.2.

2.4.5 Isoresistive mechanical tests

To characterize the mechanical behavior of the nitinol springs at intermediate temperatures, mechanical tests were conducted at seven different resistivities ranging from ρ_{max}, corresponding to the resistivity at room temperature where the nitinol is 100% martensitic, to ρ_{min} which corresponds to 100% austenitic nitinol at the maximum attainable temperature with constant heating at 100% duty cycle. a PID controller was used to control the heating rate such that a constant resistance was

Table 2.2: Curve fit functions for detwinning and resistivity profiles.

Function Type	Function Form	Curve Fit Parameters 35°C Alloy	Curve Fit Parameters 45°C Alloy
Gen. Logistic Sigmoid	$\xi_{s_m}(\gamma) = \left[1 + e^{-\beta_1\gamma - \beta_2}\right]^{\beta_3}$	$\beta_1 = 21.9987$ $\beta_2 = 2.8458$ $\beta_3 = 90.5096$	$\beta_1 = 18.9749$ $\beta_2 = 3.7937$ $\beta_3 = 155.2259$
Algebraic Sigmoid	$\xi_{s_a}(\gamma) = \frac{1}{2}\left[1 + \frac{k_1\gamma + k_2}{(1+\lvert k_1\gamma + k_2\rvert^{k_3})^{1/k_3}}\right]$	$k_1 = 12.6422$ $k_2 = -1.6532$ $k_3 = 8.0373$	$k_1 = 15.5459$ $k_2 = -1.7322$ $k_3 = 13.9375$
Algebraic Sigmoid	$\rho_m(\xi_{s_m}) = \overline{\rho} + \frac{1}{2}\rho_{span}\left[\frac{k_1\xi_{s_m} + k_2}{(1+\lvert k_1\xi_{s_m} + k_2\rvert^{k_3})^{1/k_3}}\right]$	$\overline{\rho} = 18.8697\Omega/m$ $\rho_{span} = 2.1034\Omega/m$ $k_1 = -2.2045$ $k_2 = 1.7241$ $k_3 = 7.2000$	$\overline{\rho} = 18.9763\Omega/m$ $\rho_{span} = 3.1742\Omega/m$ $k_1 = -2.0476$ $k_2 = 1.1748$ $k_3 = 3.4851$
Linear	$\rho_a(\xi_{s_a}) = \alpha_1 + \alpha_2\xi_{s_a}$	$\alpha_1 = 65.1884\Omega/m$ $\alpha_2 = 1.5648\Omega/m$	$\alpha_1 = 64.9255\Omega/m$ $\alpha_2 = -0.5693\Omega/m$
n^{th} root	$\xi_0(A,\gamma) = A^{\left(a+[1-a][\gamma/\gamma_{max}]^b\right)^{-1}}$	$\gamma_{max} = 0.195$ $a = 7.8613$ $b = 0.6906$ $\overline{a} = 7.8947$ $\overline{b} = 0.7697$	$\gamma_{max} = 0.195$ $a = 7.9280$ $b = 0.8488$ $\overline{a} = 7.8947$ $\overline{b} = 0.7697$

maintained throughout the cyclic mechanical tests. The measured shear stress versus shear strain from each resistance setpoint is shown in Figure 2.14, where the color mapping indicates the resistivity at each point along the curves.

Note that controlling the resistance to constant value does not imply constant temperature. As the springs are stretched during mechanical testing, the resistance naturally approaches P_{m_s} as detwinned martensite is formed. For example, to hold the spring at an intermediate resistance value requires some heating at the beginning of the tests to bring the resistance down to the setpoint; however, as the spring is stretched and begins forming detwinned martensite, this phase transformation brings the resistance down, so the controller stops heating to bring the resistance back up to the setpoint. Thus, the temperature may vary substantially throughout the mechanical testing process as it is used to compensate for changes in resistance due to the formation of detwinned martensite.

Another important feature to note is that constant resistance cannot always be maintained throughout the mechanical tests. This is because the resistivity necessarily approaches P_{m_s} at high strains where ξ_s approaches 1. Thus, at high strains, no amount of heating or cooling can cause significant deviation from P_{m_s}. This behavior is seen in Figure 2.15 which shows the measured resistivity during the loading paths from the isoresistive mechanical tests. While the resistivity in each subplot begins at the setpoint value, it always approaches P_{m_s} at high strains as ξ_s approaches 1.

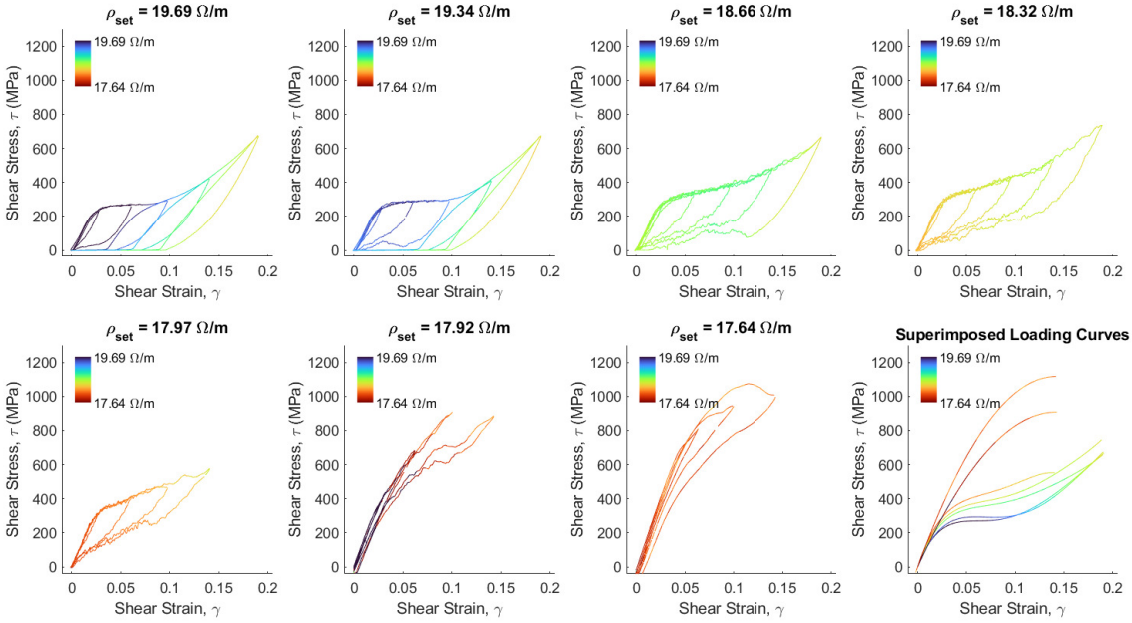

(a) 35°C transition temperature

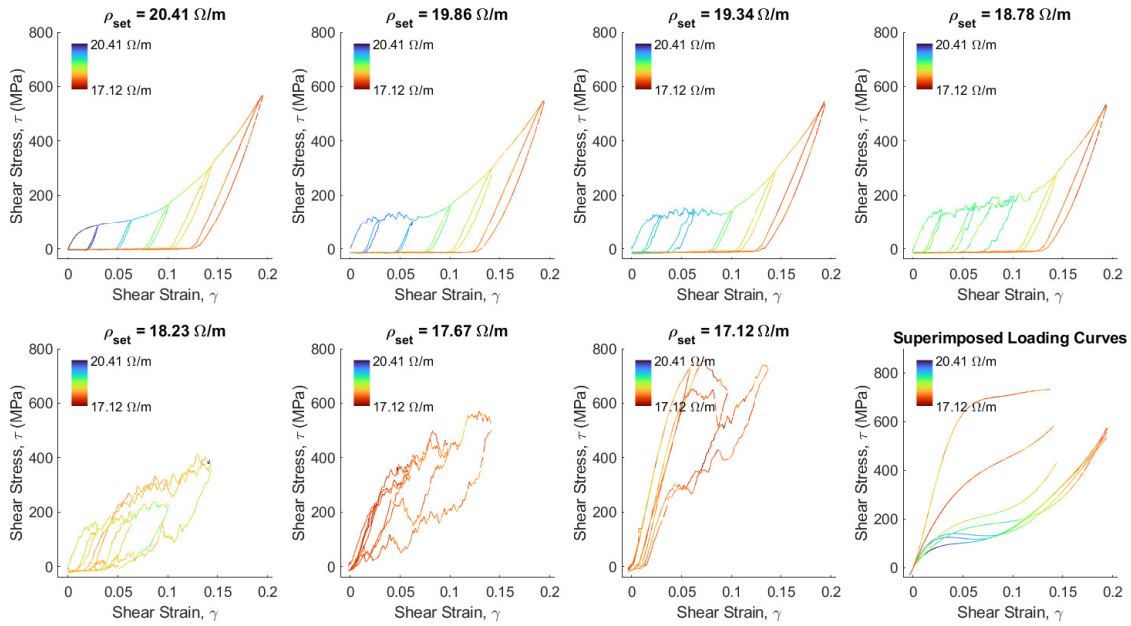

(b) 45°C transition temperature

Figure 2.14: Measurements of shear stress versus shear strain at constant resistance in two different Nitinol springs.

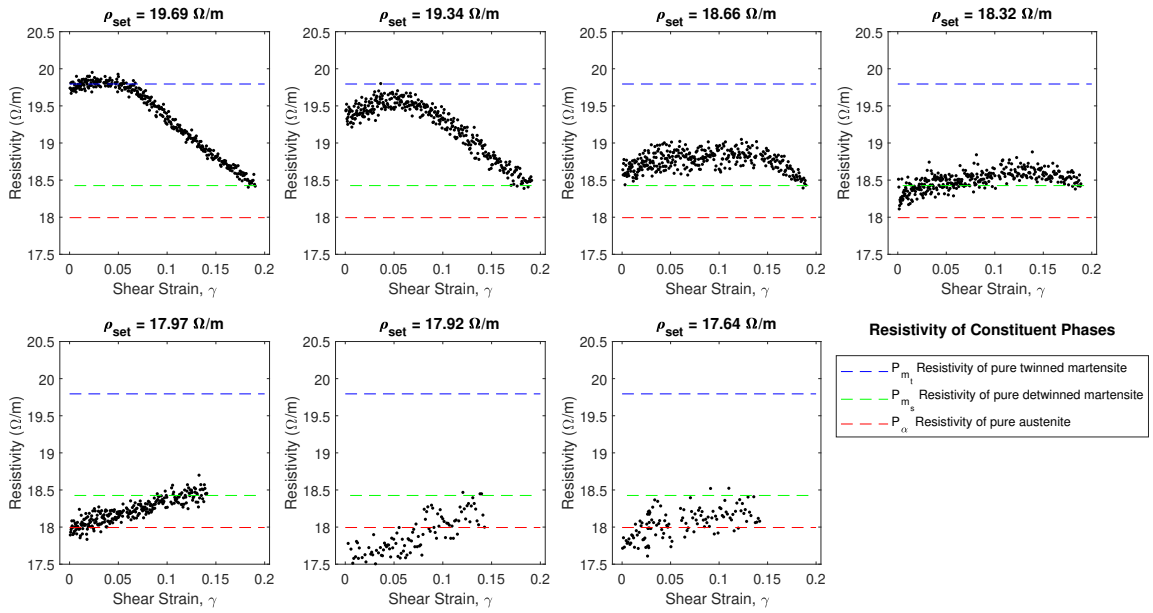

(a) 35°C transition temperature

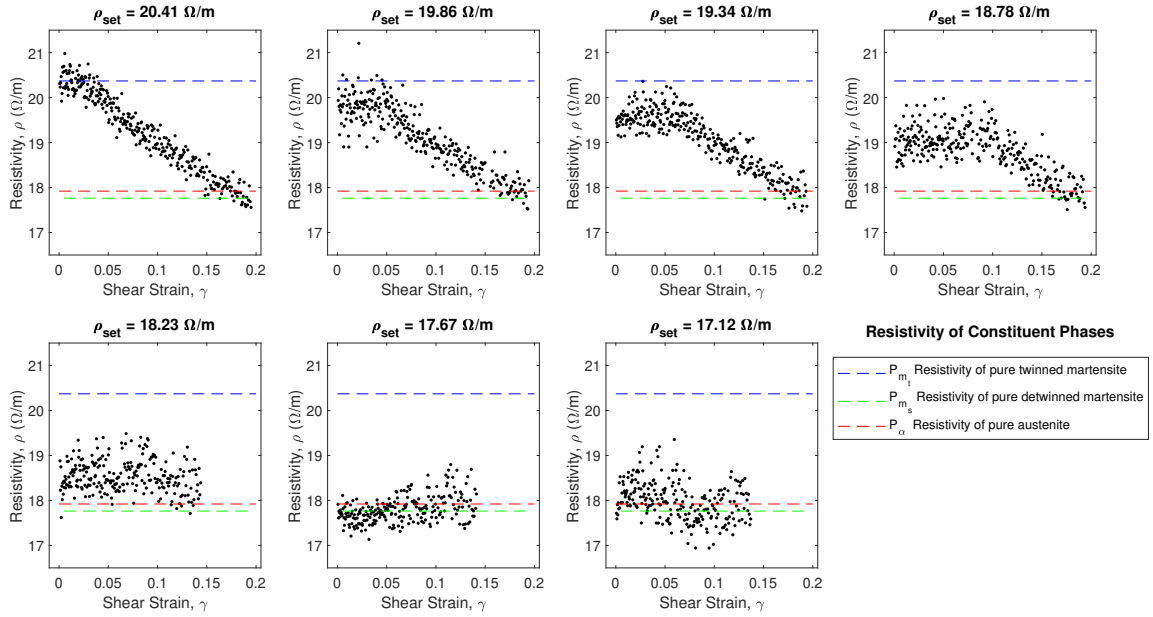

(b) 45°C transition temperature

Figure 2.15: Measurements of resistivity during loading from isoresistive tests in two different Nitinol springs.

Using the phase fraction interpolation function proposed in the modeling section, the phase fractions are computed from the shear strain and electrical resistivity using Eqs. 2.48, 2.25, 2.26, 2.27, and 2.28. These phase fractions calculated from the loading portions of the isoresistive mechanical tests are shown in Figure 2.16.

After calculating the phase fraction ξ_0 from the resistivity ρ, the shear stress as a function of shear strain can be calculated using Eq. 2.33. This shear stress model is plotted alongside the loading data from the isoresistive mechanical tests in Figure 2.17. The interpolation function parameters for Eqs. 2.47, 2.41, and 2.48 were found by minimizing the residuals in the model fit to the loading data from the intermediate resistance tests. The same values of a and b in the interpolation function were used to interpolate between the low- and high-temperature data from both alloys. These interpolation function parameters are listed in Table 2.2.

As seen in Figure 2.17, the proposed model based on electrical resistivity shows good agreement with the experimental data for both alloys. The mean absolute error (MAE) and relative percent difference (RPD) were calculated from the shear stress versus shear strain data from each isoresistive test individually and again for the entire series of tests from each alloy. The overall relative percent difference between the experimental data and the model fit for the 35°C and 45°C alloys were 9.6% and 12.4%, respectively.

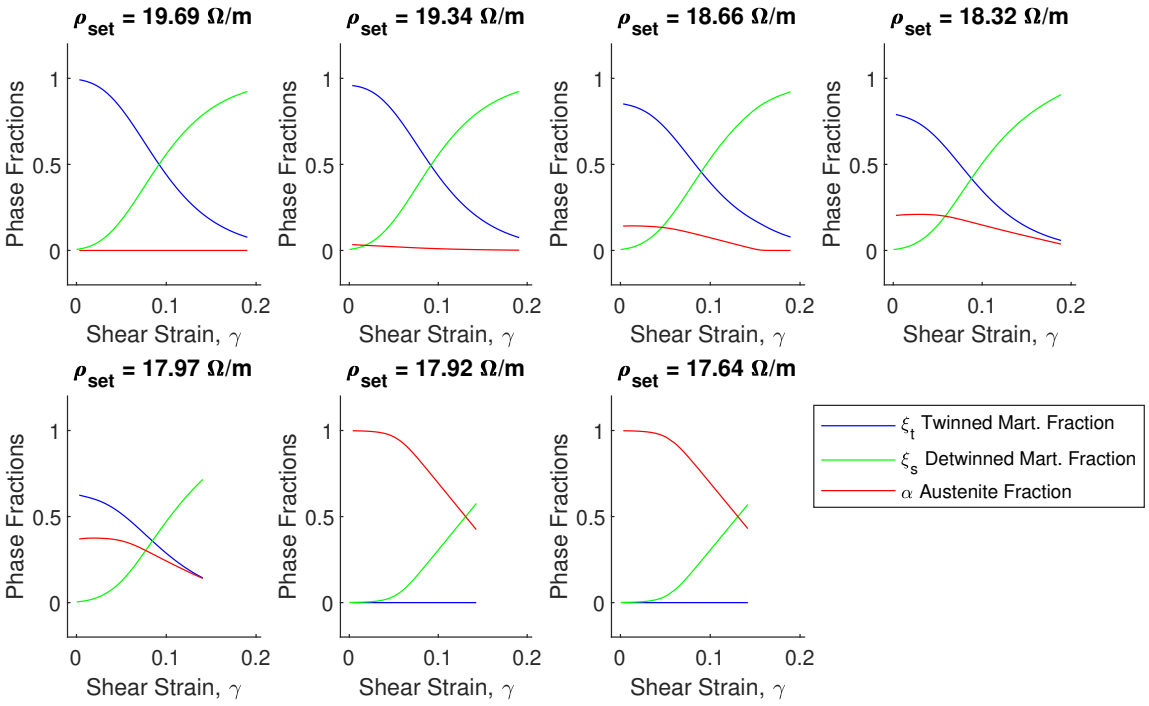

(a) 35°C transition temperature

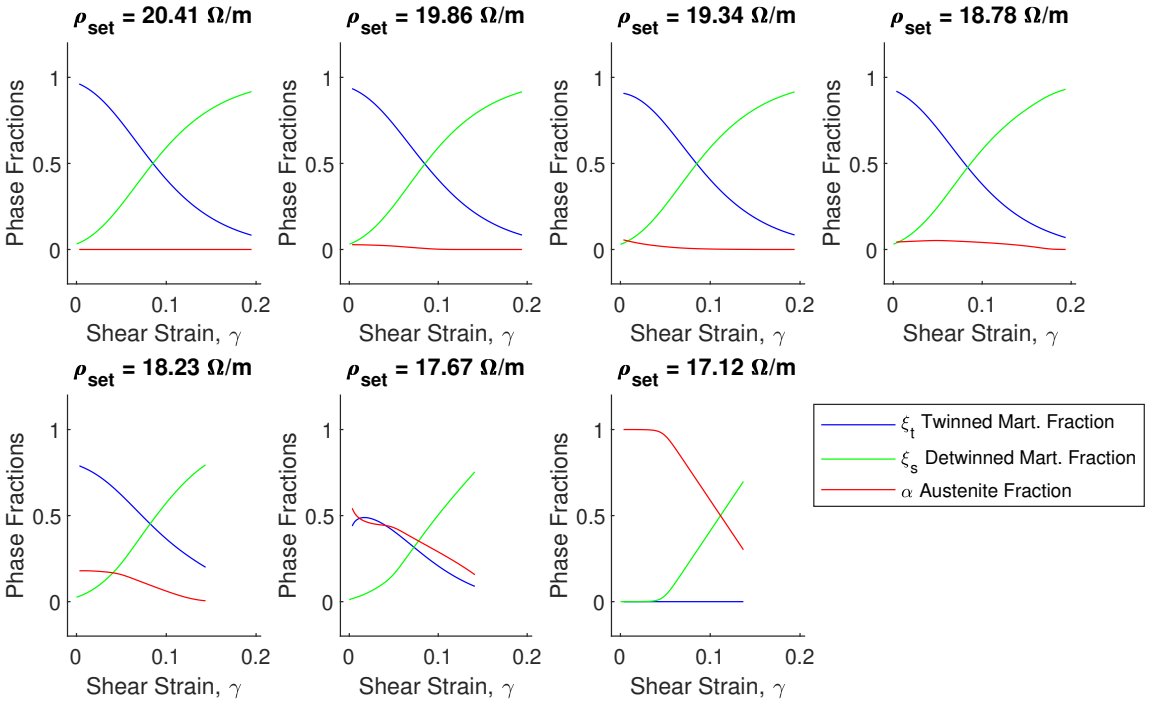

(b) 45°C transition temperature

Figure 2.16: Phase fraction evolution during isoresistive testing of two different nitinol springs.

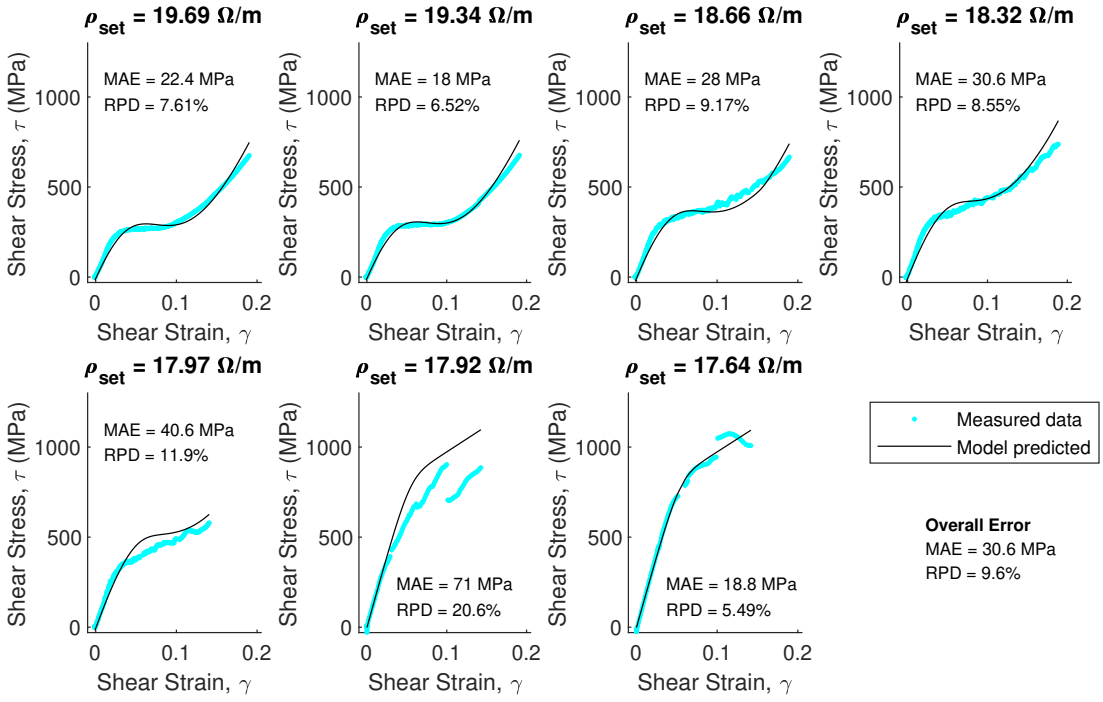

(a) 35°C transition temperature

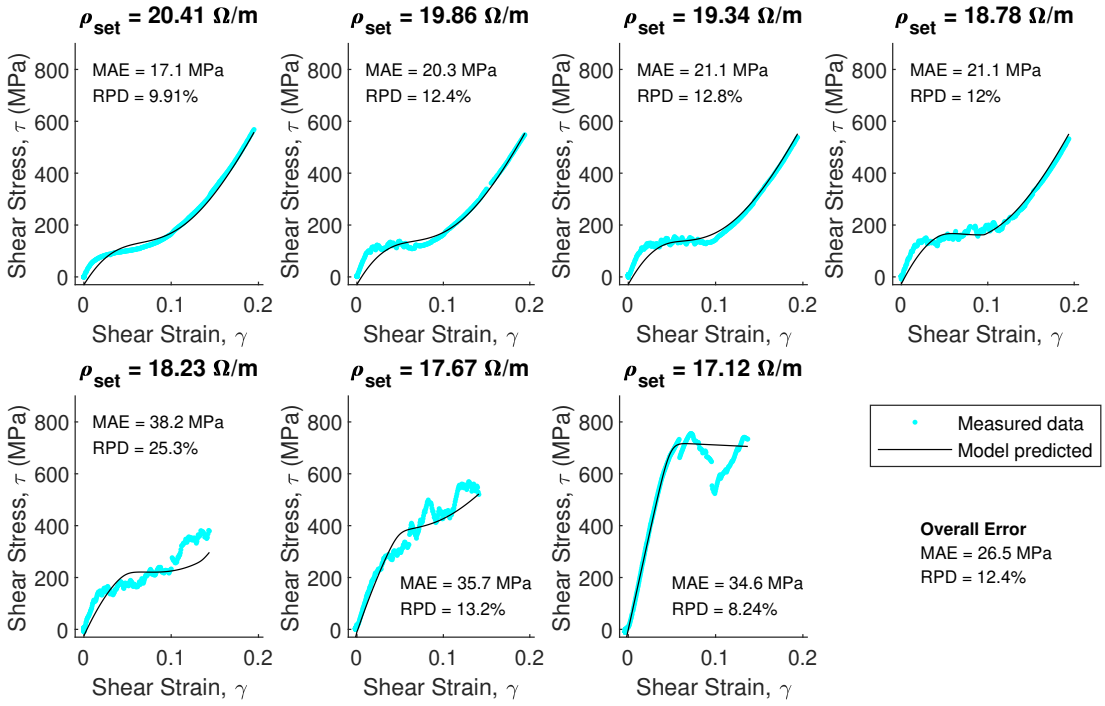

(b) 45°C transition temperature

Figure 2.17: Model fit to loading data from two different nitinol springs.

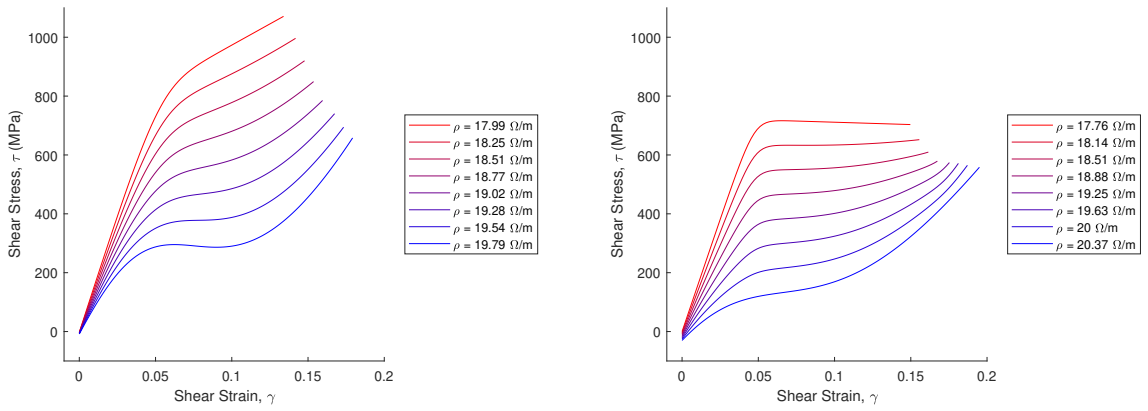

(a) 35°C transition temperature **(b)** 45°C transition temperature

Figure 2.18: Families of isoresistive loading curves for two different nitinol springs.

2.4.6 Model implications

Using the resistance-based model developed in this work, families of isoresistive stress-strain curves can be generated, as shown in Figure 2.18. These curves enable observation of the nitinol's behavior at intermediate temperatures based on its electrical resistance. If the resistivity is known, the model can predict the loading path that will be followed. Similarly, a surface can be generated from the model to show the loading path for all resistivity values, as shown in Figure 2.19. Note that the domain of these surfaces is limited by the bounding curves $\rho_m(\gamma)$ and $\rho_a(\gamma)$, thus excluding resistivity values that are impossible to achieve at high strains.

The following paragraphs outline steps for applying the resistance-based model to different spring geometries and/or different SMA's or nitinol alloys.

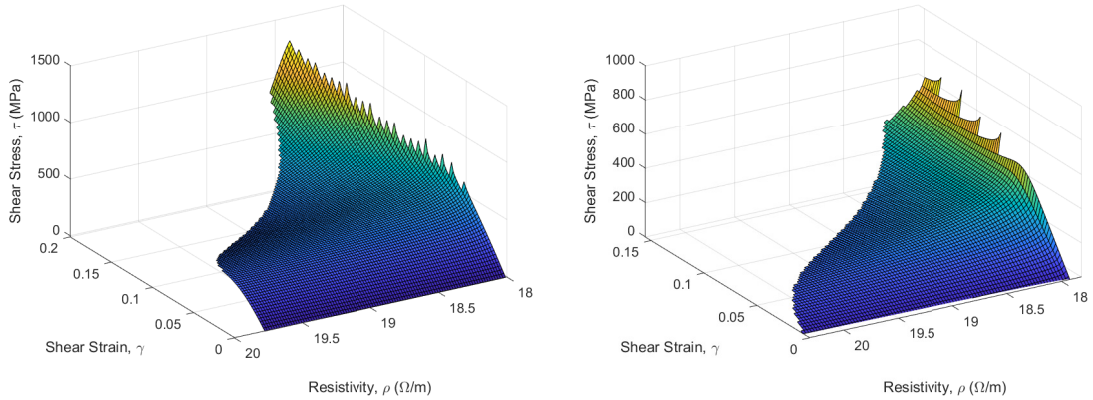

(a) 35°C transition temperature **(b)** 45°C transition temperature

Figure 2.19: Loading surface as a function of resistivity for two different nitinol springs.

Extending to different spring geometries

The model developed in this work can easily be applied to any spring geometry if the same alloy composition and heat treatment are used. To predict the force-strain relationship for a 35°C or 45°C transition temperature nitinol alloy with a new spring geometry, the functions for $\xi_{s_m}(\gamma)$, $\xi_{s_a}(\gamma)$, $\rho_m(\xi_{s_m})$, $\rho_a(\xi_{s_a})$, and $\xi_0(A, \gamma)$ determined from these experiments (presented in Table 2.2) may be directly used. These functions can be used to compute the martensite fraction and relate the shear stress and shear strain during loading at any given resistivity, according to Eq. 2.49. Equation 2.9 and the reverse of Eq. 2.17 can then be used to convert the normalized shear stress and shear strain to find the actual spring force and corresponding spring strain for any spring geometry.

Extending to different nitinol alloys

Applying the resistance-based model to different nitinol alloys requires some experimental characterization on the new alloy as varying the composition affects both the transition temperature and the resistivity of each phase. Still, not every test need be repeated. The process for applying the model to springs of a new nitinol alloy simply requires running tensile tests on the springs at a low temperature (below M_f) and a high temperature (above A_f) while monitoring the resistance of the coils. The measured force and spring strain can then be converted to shear stress and shear strain using Eqs. 2.8 and 2.17. The detwinned martensite fraction from each test can then be plotted against the shear strain using Eqs. 2.34 and 2.35. The measured resistance should be normalized using Eq. 2.2 then plotted for each test against the detwinned martensite fraction. The detwinning and resistivity profiles should follow the same sigmoidal and linear patterns observed in the 35°C and 45°C alloys, so the curve fit functions for $\xi_{s_m}(\gamma)$, $\xi_{s_a}(\gamma)$, $\rho_m(\xi_{s_m})$, and $\rho_a(\xi_{s_a})$ from Table 2.2 can be fit to the measured data with appropriate new curve fit parameters. The interpolation function $\xi_0(A, \gamma)$ was used with the same averaged fit parameters $\overline{a}$ and $\overline{b}$ from Table 2.2 for both the 35°C and 45°C alloys in this work and produced good agreement between the model and experimental data for τ versus γ. These parameters would likely hold true for other nitinol alloys, especially those with transition temperatures within 10-20 C° of those tested in this work.

Extending to different SMA's

When applying the resistance-based model to other, non-nitinol shape-memory alloys, the same procedure described in the previous paragraph should be followed to characterize the detwinning and resistivity profiles at both extremes (100% martensite and 100% austenite). However, the interactions between phases and resulting effects on electrical resistivity in other SMA's may not follow the same pattern observed in the nitinol material. Thus, the interpolation function $\xi_0(A, \gamma)$ may have an entirely different form or noticeably different fit parameters. To determine the form of this function, at least one additional mechanical test should be conducted at an intermediate temperature where $\xi_0 \neq 0$ and $\xi_0 \neq 1$. Once the interpolation function has been determined, the model can be applied as usual to predict the shear stress and shear strain relationship for any resistivity within the allowable range.

2.5 Conclusions and future work

In this paper, a resistance-based mechanical model for the stress-strain behavior of nitinol springs was presented. The proposed model successfully captures the variation in elastic stiffness and detwinning behaviors at both extreme and intermediate temperatures where martensite and austenite phases coexist. Although the mechanical properties of nitinol are highly temperature-dependent, we found that the stress-strain paths can be determined from the electrical resistance alone, without knowing

the temperature.

The resistance-based model stems from Brinson's thermo-mechanical model, which was adapted by An et al. to apply to SMA springs in fully-austenitic or fully-martensitic states. The Brinson-An model was modified and extended in this work to broaden its applicability and simplify its expression. The modifications/extensions made to the Brinson-An model are as follows:

- The Wahl correction factor was included to account for curvature effects in springs with small spring indices.
- Terms were added to the shear stress equation to account for nonlinear detwinning of martensite and nonlinear formation of detwinned martensite from austenite—both of which occur outside the linear elastic regions.
- The martensite fraction was expressed as a function of resistance and strain rather than temperature, critical stresses, and current stress which are difficult to measure.
- An interpolation function was presented to model the nonlinear effects of interaction between multiple phases/variants on the overall electrical resistance. This function allows the phase fraction to be computed directly from resistance.

With these modifications, the model can be applied to springs of various geometries in any temperature and strain region without direct knowledge of temperature or

internal stresses.

The model was validated against data from electro-mechanical testing of two nitinol springs with different transition temperatures: 35°C and 45°C. A series of isoresistive stress-strain curves were obtained from increasing cyclical loading of the springs while appropriate Joule heating or convective cooling was used to maintain constant resistance. Data from the room temperature tests (maximum resistance) and the maximum temperature tests (minimum resistance) were used to determined the detwinning profiles and resistivity profiles in the fully-martensitic and fully-austenitic states. The phase fractions could then be determined at intermediate temperatures using a power law interpolation function. Hence, the stress-strain behavior at intermediate temperatures can be obtained from the electrical resistance alone.

This model may be used for nitinol position control with electrical resistance feedback in a variaty of SMA-actuated devices. While most existing SMA resistance models require input of temperature and applied stress, the resistance-based model relies solely on resistance feedback. This feature shows particular promise for microrobot and soft robot applications where embedding additional sensors is impractical due to their relative size, weight, and complexity. It is possible that other functions may replace or improve upon the power law interpolation function presented in this paper. As more alloys are tested, a more generalized interpolation function may be developed. Nevertheless, the results of this study prove the feasibility of modeling

the stress-strain behavior of nitinol springs based on electrical resistance alone.

CHAPTER THREE

PNEUSMA ACTUATOR DESIGN AND MODELING

3.1 Abstract

The surge in soft robotics research in recent years has encouraged the development of many soft actuation systems to enable high dexterity and maneuverability in soft, flexible devices. The motivation for such devices stems largely from the medical field where the potential to replace traditional, rigid instruments with more flexible, maneuverable devices could significantly improve safety and accessibility for endoluminal and endovascular procedures. Among the most common soft actuation methods is pneumatic actuation where pressurized air is used to deform a soft device with the deformation mode predetermined by the geometric anisotropy of the device. Standard pneumatic actuators offer limited maneuverability on their own as each pneumatic chamber can only perform a simple bending, twisting, elongation, or contraction motion. Improved maneuverability can be realized by combining multiple pneumatic actuators in series and parallel combinations, but these arrangements require complicated networks of supply tubing to control each pneumatic chamber independently. In this chapter, a novel, hybrid pneumatic/shape-memory alloy (PneuSMA) actuation method is proposed where multi-directional bending can be achieved throughout the entire length of the actuator with a single pneumatic chamber. The resistance-

based mechanical model from the previous chapter is used to describe the forces in the SMA springs which are incorporated in a quasi-static analytical model for the PneuSMA actuator. Characterization of the silicone's geometry-specific mechanical properties is also conducted in this chapter with results incorporated in the analytical model. Comparison of the analytical model with experimental curvatures from several variations of the PneuSMA actuator confirms the viability of predicting the configuration of PneuSMA actuator devices based on the input pressure and SMA spring resistivities.

3.2 Introduction

Soft robotics is a trending research field that seeks to enable functional robotic manipulations using soft, elastic materials that can easily deform upon impact to prevent damage of delicate objects/surroundings. The last two decades have seen enormous advancements in the materials and actuation mechanisms involved in soft robotic devices. State-of-the-art soft robots capable of grasping, squeezing, jumping, peristalsis, and snake-like manipulations have been demonstrated in [85, 112, 190, 176, 38, 181, 131]. These features lend themselves particularly well to medical applications where their compliant nature can reduce risks of puncturing or damaging sensitive organs and other tissue during various medical procedures [198, 2, 178, 32].

There is a need for highly-maneuverable flexible devices for endoscopic medical procedures which require navigation through various lumens or vasculature to

treat conditions such as gastric lesions, colorectal polyps, or atherosclerosis [78, 42]. Whereas traditional catheters and endoscopes rely on manual pushing to advance a tip-steerable device, improved steerability throughout the entire length of a flexible instrument would help prevent incomplete or painful procedures [113]. Various approaches to soft actuation for flexible catheter/endoscope devices have been explored, the most prominent mechanisms being pneumatic- and tendon-driven actuation [62]. A review of tendon-driven catheter devices was given in Chapter 1; the remainder of this section will focus on pneumatic soft actuators.

3.2.1 Pneumatic soft actuators

Pneumatic soft actuators typically consist of one or more elastomeric pneumatic chambers where some form of anisotropy causes bending, twisting, extension, or contraction with pressurization [194]. Bending actuators are the most suitable for standalone steerable medical devices as steerability is primarily achieved through bending motions. The bending of pneumatic soft actuators is accomplished through asymmetric geometry, usually realized by inflatable voids along one side [193, 65], combinations of multiple materials with different stiffness properties [170, 103], or asymmetric arrangements of inextensible fibers [137, 36]. Two common approaches include PneuNET actuators where a network of serial chambers are inflated to cause extension on one side while the other side maintains its original length [122, 158]; and PneuFLEX actuators which feature a double helical fiber wrapping to prevent radial expansion

and a strain-limiting fiber or fabric along one side to induce bending upon inflation [45, 44, 119].

Each of these approaches are limited as they can only bend in one prescribed directions, and they lack the ability to perform more diverse manipulations [45, 44]. Some attempts at pneumatic actuators with multi-directional bending capabilities have been explored. Most commonly, directional control is achieved using a parallel triad arrangement of bellows actuators [83, 202, 49, 196], contractile pneumatic actuators [195], or extensional pneumatic actuators [143, 201, 171]. These arrangements offer three degrees of freedom (pitch, yaw, stretch) as pressurizing any one of the chambers on its own causes bending while simultaneous activation of all three chambers causes elongation [194]. Other novel approaches include combined tendon/pneumatic actuation [146, 126, 161, 108] or tendon-driven deformation of pre-charged pneumatic chambers [98, 97]. Each of these methods can successfully achieve multi-directional bending in a single pneumatic actuator, but these designs are impractical for larger scale systems as connecting multiple actuation modules in series would require an impractical number of supply tubes or tendons to independently control each segment.

3.2.2 SMA's in soft actuators

Shape-memory alloys (SMA's) are often used as standalone actuators, but they can also be incorporated in soft actuators to provide intrinsic deformation capabilities in soft robotic structures. Examples similar to the proposed work include the

flexible artificial muscle by Taniguchi and the inflatable, tendon-driven actuator by Maghooa et al [174, 108]. Taniguchi's artificial muscle includes two opposing SMA springs encased in a sealed chamber. Bending in either direction is achieved by heating/contracting one of the SMA springs. The pneumatic component is used to speed the cooling of the SMA springs and hence improve the response time of the device [174]. The inflatable, tendon-driven actuator by Maghooa and colleagues features a triad arrangement of SMA springs in a sealed chamber to enable multi-directional bending while the pneumatic chambers may be pressurized to enable peristaltic motion [108].

3.2.3 PneuSMA actuator design

The PneuSMA actuator combines the advantageous features of both pneumatic soft actuators and SMA actuators in a single device with improved maneuverability compared to simple fiber-reinforced pneumatic bending actuators [6]. The PneuSMA actuator consists of a thin silicone tube with pre-stretched SMA springs placed along the sides of the tube as shown in Figure 3.1 (a). A tightly-spaced circumferential wrapping of polyester thread secures the SMA springs to the actuator and prevents radial expansion with inflation. Heating any particular region of one of the SMA springs causes bending in that region due to the uneven forces between the hot and cold springs on opposite sides. Pressurization of the tube can further increase the curvature or cause the actuator to straighten slightly, depending on the SMA spring

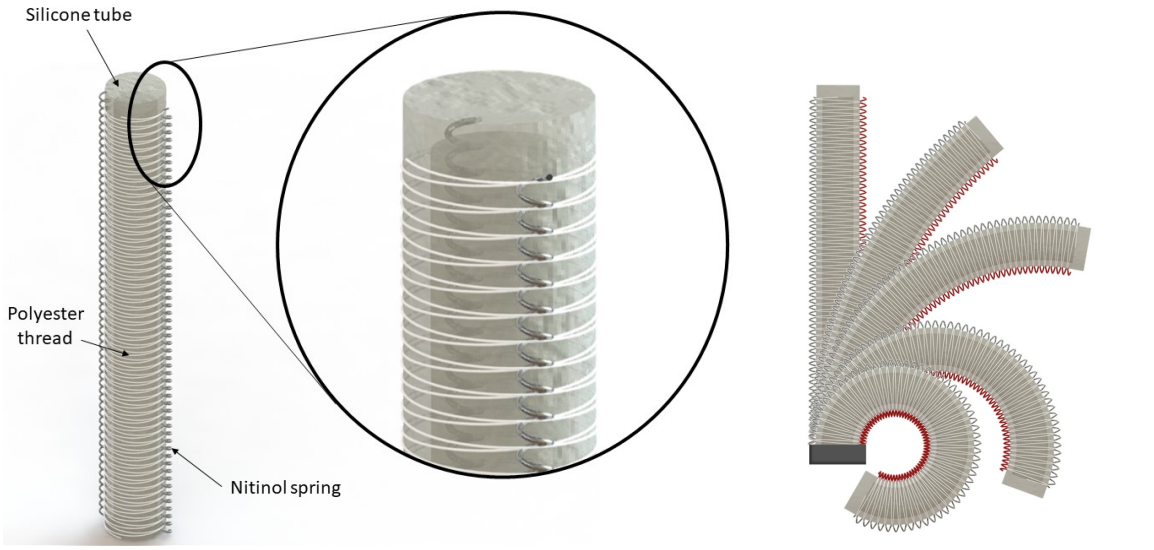

(a) Closeup diagram of PneuSMA actuator with two opposing SMA springs.

(b) Illustration of bend angle and curvature variation in PneuSMA actuator.

Figure 3.1: PneuSMA actuator design and bending capabilities.

arrangement and activation states. Varying the pressure has relatively minor effects on the curvature and is primarily used to prevent tube buckling and enable independent stiffness control.

As shown in Figure 3.1 (b), the curvature and bend angle of the actuator can be controlled by adjusting the heating rate and hence the contraction of the nitinol springs. Figure 3.2 shows some of the many configurations that can be achieved by heating select regions of the nitinol springs to cause multi-segmented bending. While simple fiber-reinforced bending actuators can only exhibit continuous, uniform bending in a single direction, the PneuSMA actuator can bend in multiple directions with independent control of different segments with a single pneumatic chamber.

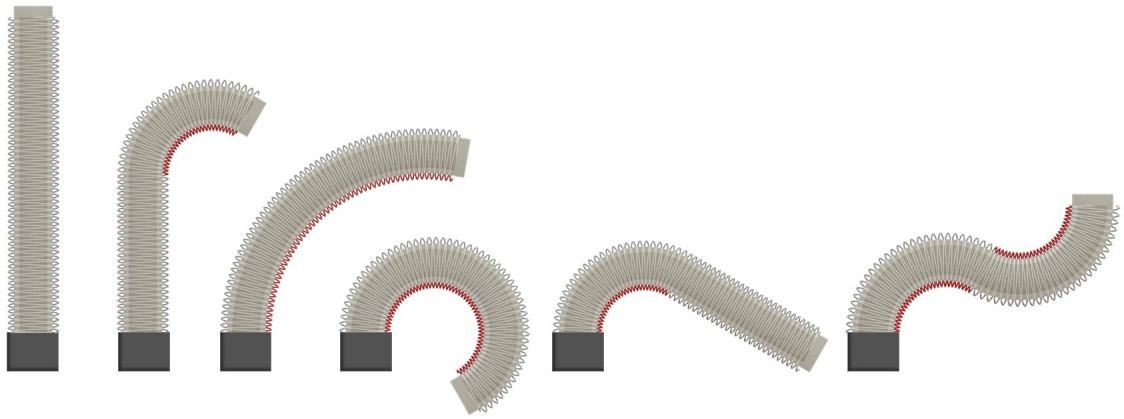

Figure 3.2: Illustration of various PneuSMA actuator configurations achievable by heating select regions of nitinol springs.

This prevents the need for the numerous supply tubes that would be required for fiber-reinforced bending actuators with multiple series segments, each with their own pneumatic cavities. Also note that the springs can be arranged in a triad arrangement or with alternating segments of springs in 90° offset planes to enable three-dimensional bending.

3.2.4 Soft actuator modeling/control methods

Polygerinos and colleagues point out that a lack of robust modeling for multi-material pneumatic actuators limits the potential promised by empirical approaches [138]. The complicated nature of hyperelastic materials and geometric configurations results in nonlinear response to applied pressure/activation which makes predictive modeling a challenge. Many pneumatic actuators can be modeled using a piecewise

constant curvature (PCC) assumption which involves modeling segments as a series of tangent curves with constant curvature in each segment [188, 194]. While this approximation is reasonable for most cases when inertial effects are minimal, the application of external loads and consideration of gravitational effects can cause significant deviations from true constant curvature deformations [43, 64, 128]. Nevertheless, variable curvature models add significant complexity, and the PCC approach is often sufficient for lightweight devices [10, 110, 75, 157, 164]. Polygerinos et al. presented a quasi-static modeling approach for simple fiber-reinforced bending actuators based on the PCC assumption [138]; this model serves as a foundation for the PneuSMA actuator model developed in the present work.

Contents and layout

The remainder of this chapter begins with a review of the fundamental principles underpinning the behavior of each material in the PneuSMA actuator. The mechanical properties of each material are discussed, and material characterization studies are presented in Section 3.4, including characterization methods for silicone buckling and nitinol residual strain. The analytical model for the PneuSMA actuator is then developed in Section 3.5, based on the material models presented in Section 3.4. Section 3.6 explains the process for fabricating PneuSMA actuators for experimental testing. The experimental setup and PneuSMA test samples are described in Section 3.7, followed by a comparison of the experimental results with the analytical model

in the same section. Implications of the analytical model as well as an overview of the next steps are provided in Sections 3.8 and 3.9, respectively.

3.3 Background

Before delving into specific modeling strategies for the PneuSMA actuator, it is necessary to understand the fundamental behaviors of each material involved. The following sections provide an overview of the unique properties of nitinol and silicone materials.

3.3.1 Properties of nitinol material

Nitinol is a metal alloy consisting of roughly equal parts of nickel and titanium. Nitinol is renowned primarily for its shape-memory and super-elastic capabilities which are enabled by transformations between different crystal structures and variant orientations within the solid phase. At high temperatures, above the critical transition temperature, nitinol takes on a cubic crystal structure called the austenite phase. Austenitic nitinol has a relatively high stiffness with elastic modulus around 11×10^6 psi [118]. When austenitic nitinol is cooled below the transition temperature, it transforms to a monoclinic crystal structure called martensite. In the absense of stress, the martensitic phase contains multiple self-accommodating variants and twins due to differing habit plane indices between grains. This multivariant martensite phase is referred to as twinned martensite and has a significantly lower stiffness than the

austenite parent phase with an elastic modulus of about 4×10^6 psi [118]. When stress is applied to the twinned martensite phase, the atomic planes begin to rearrange, eventually converting to a single variant with sufficient stress application. This unique process is known as detwinning. During this process, the monoclinic ctystal structure is preserved; the variants simply align based on the axis of loading. Upon unloading, the variants do not revert back to twinned martensite but maintain their new orientations, which causes substantial psuedo-plastic strain to be sustained after unloading. However, since the atomic bonds were not broken in the detwinning process, the material reverts to austenite and returns to its original shape when heated above the transition temperature. This feature is responsible for the shape-memory effect which allows significant pseudo-plastic strains (up to 6-8%) to be recovered with thermal cycling.

A similar conversion to detwinned martensite also occurs in the austenite phase at high temperatures. When austenitic nitinol is stressed beyond a threshold, it begins converting to single variant detwinned martensite, and the stress-strain curve begins to plateau. However, no plastic strain is incurred as the martensite phase is thermodynamically unstable at high temperatures and immediately reverts back to austenite when the load is removed. This reversible formation of detwinned martensite from austenite at high temperatures is responsible for nitinol's prized super-elastic behavior. The transition temperature and default configuration can be set by tuning

the alloy composition and selecting appropriate heat treatment processes.

Straight wire versus spring geometry

With the exception of occasional truss structures [4, 142] and lithographic thin films [15, 147], nitinol is used almost exclusively in two geometries: straight-drawn wire and helical springs. Straight wire is often preferred for its availability, low cost, high strength, compactness, and simplicity for modeling. However, the coiled geometry offers several advantages that make it preferable for many applications. Nitinol springs can be used in both tension and compression, and they provide significantly larger stroke than straight wire which is limited to 6-8 % recoverable strain.

Some manufacturers offer pre-made nitinol springs in a few select sizes, but users can create more sizes and pitch customization by shape-setting their own springs from straight nitinol wire. The shape setting process for helical springs involves wrapping the nitinol wire tightly around a heat-tolerant mandrel with the desired coil spacing. The clamped assembly is then placed in a furnace at $\sim$500°C for $\sim$5 minutes then cooled via water quench. Varying the shape-setting temperature, duration, and cooling conditions affects the transition temperature, peak force, and resistance to permanent deformation.

Mechanical Modeling and resistance feedback approach

The mechanical properties of nitinol are highly temperature-dependent due to the thermoelastic phase change that occurs over the transition temperature region. Several different approaches for modeling the thermomechanical behavior of nitinol have been developed, for example [1, 11, 13, 19, 51, 52, 73, 99, 102, 151, 169, 172], which characterize the stress-strain behavior based on temperature and phase transformation kinetics using microscopic, macroscopic, or mixed modeling methods [35]. Perhaps the most well-known is the one-dimensional thermomechanical constitutive model by Brinson which relies on temperature- and stress-dependent phase fractions to compute the strain in straight nitinol wire given the applied stress and several critical stress and transition temperature parameters [23]. In the previous chapter, several important modifications to the Brinson model were presented in order to replace the temperature dependence with electrical resistance and extend the model for application to helical spring geometries. The resistance-based mechanical model uses resistance measurement to monitor the internal phase transformation behavior and compute the resulting stress-strain relationship for any spring geometry. While a linear relationship between strain and resistance has been observed in straight nitinol wire [3, 191, 39, 159, 57], the coiled geometry causes significant nonlinearity that is not addressed in other works. The resistance-based model developed in the previous chapter bridges this gap and allows for modeling the mechanical behavior of nitinol

springs using more convenient variables that be measured in an actual soft robotic device.

In many soft robotic devices, including the PnueSMA actuator, measuring the temperature and/or force in the SMA springs is impractical due to space/weight limitations, nonuniform heating, transient response, and the need to maintain simplicity and flexibility. Thus, the use of resistance-based mechanical modeling for SMA's in such devices shows great promise. In order to apply the resistance-based model to soft robotic devices such as the PneuSMA actuator—where the springs may be pre-strained, loaded, relaxed, heated, and cooled in any order to reach a desired configuration—both loading and unloading conditions must be accounted for in the SMA model, including the pseudo-plastic deformation and residual strain responsible for the shape-memory effect. The resistance-based model developed in the previous chapter applies only to loading from zero pre-strain but can easily be extended for application to unloading and reloading after accruing pseudo-plastic deformation. These extensions to the resistance-based nitinol mechanical model are described in section 3.4.1.

3.3.2 Properties of silicone material

Silicone rubber is a popular choice for soft robotic actuators due to its flexibility, durability, temperature-resistance, and biocompatibility. Silicone is an elastomeric polymer containing silicon, carbon, hydrogen, and oxygen. Before curing, silicone is

a viscous liquid or gel. The curing process for generally involves an addition reaction where mixture with a complex catalyst causes the formation of ethyl bridges that convert the silicone to a solid. Silicones are available in a variety of hardness categories from Shore A 25-90, and are often formed by casting or injection molding.

Silicones are classified as hyperelastic materials as they can undergo large elastic deformations and the relationship between stress and strain can be derived from a strain energy density function. Several different hyperelasticity models—including Mooney–Rivlin, Yeoh, Neo–Hookean, Ogden, Humphrey, and Veronda–Westmann—are used to describe the stress as a function of principle stretches [117]. Different models provide better accuracy in different strain regions; an appropriate model is generally selected based on the anticipated range of operating strains.

Hyperelasticity model parameters for various elastomers have been reported in the literature, based on the assumptions of incompressibility and isotropy [37, 193, 153]. These parameters can be used to model the behavior of silicone rubber in tension, but they generally do not apply to stresses/strains under compression. In the PneuSMA actuator, the silicone tube is primarily in tension due to the positive internal pressure, but when heated, the nitinol springs contract and place regions of the silicone under compression. Strong activation of the nitinol springs paired with low internal pressure can also cause buckling of the silicone material. The behavior of the silicone material under compression and with buckling must be accounted

for when modeling the PneuSMA actuator. In section 3.4.2, a characterization of the tension/compression/buckling behavior of the Dragon Skin 10 FAST silicone is presented for incorporation in the PneuSMA analytical model.

3.4 Experimental characterization of constituent materials

Developing an accurate model for the PneuSMA actuator requires robust characterization of the materials involved. Extensive characterization of nitinol springs was conducted in the previous chapter, but further analysis to account for accumulation and recover of residual strain is presented in this section. Although the hyper-elastic properties of silicone materials have been well-studied, there are geometry-specific aspects—such as the buckling force and stress state in the fiber-reinforced tube—that require further study. The characterizations of the nitinol springs and silicone material for application to the modeling of the PneuSMA actuator are presented in this section.

3.4.1 Nitiol spring characterization

In the previous chapter, a resistance-based mechanical model was developed for nitinol springs. The resistance-based nitinol model is capable of computing the relationship between spring force and spring strain for any spring dimensions, given the electrical resistivity of the nitinol material. Figure 3.3 shows a family of stress-strain curves generated by the resistance-based nitinol spring model from the previous chap-

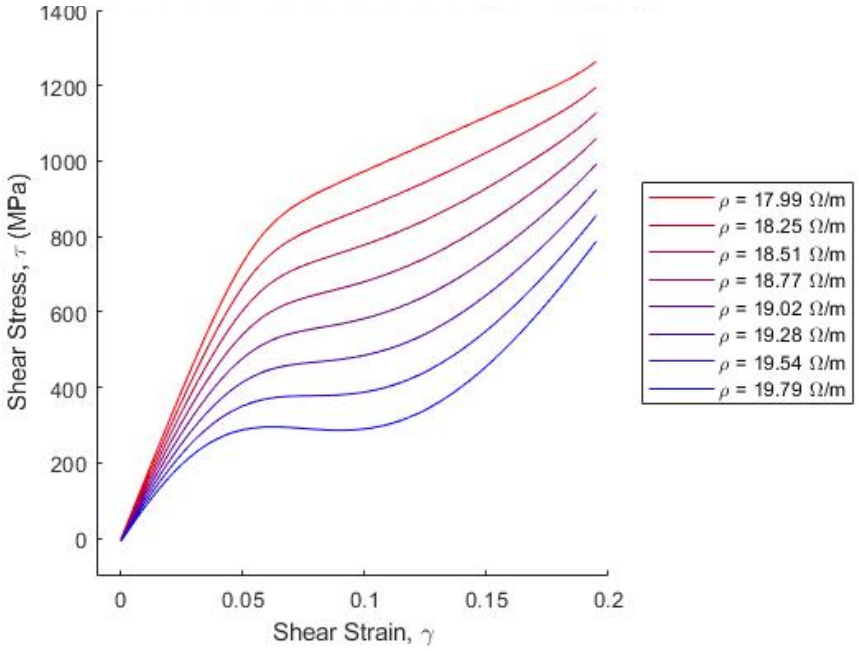

Figure 3.3: Isoresistive stress-strain curves generated by resistance-based model from the previous chapter for 35°C nitinol springs.

ter. It should be noted that this model does not account for the residual strain accrued when psuedo-plastic strain is accumulated upon loading and then unloading at low temperatures. In the PneuSMA actuator, the nitinol springs are pre-strained before being attached to the actuator, so the residual strain plays an imporant role in the spring forces acting in the actuator. In this section, a simple function for the residual strain is presented along with a linear model for the loading from a pre-strained state.

Accounting for residual strain and unloading behavior

The residual strain that remains after load removal is due to the stress-induced detwinning of the twinned martensite phase. After unloading, the detwinned marten-

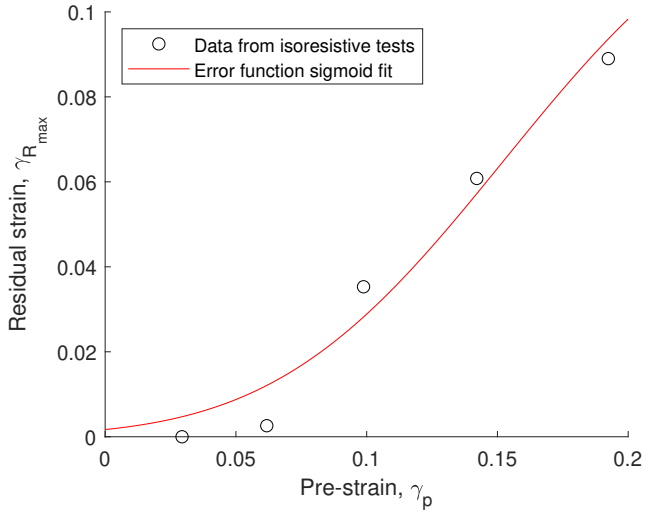

Figure 3.4: Residual strain as a function of pre-strain for 100% martensitic nitinol springs.

site does not "re-twin," so it does not return back to zero strain, but maintains some residual strain. At high temperatures, there is no residual strain as the detwinned martensite is not thermodynamically stable. Thus, when austenitic nitinol is loaded and then unloaded, the detwinned martensite reverts immediately back to austenite and no residual strain is sustained.

The residual strain can be modeled as a simple function of the onset martensite fraction ξ_0 and the pre-strain γ_p. The isoresistive mechanical test data for the 35C nitinol springs from the previous chapter show some residual strain in the low temperature (high resistance) tests. In the first isoresistive test, the onset martensite fraction is assumed to be one, and the maximum residual strain is observed. Isoresistive tests at higher temperatures have lower residual strains as ξ_0 is no longer one, and

conversion to austenite causes some recovery of residual strain. Figure 3.4 shows the residual strain in the 100% martensite springs as a function of the pre-strain γ_p. The circular data points were extracted from the first isoresistive test at room temperature where ξ_0 was assumed to be one. For example, when the spring was stretched to $\gamma_p = 0.1924$ then released, it maintained a residual strain of $\gamma_R = 0.089$. An error function sigmoid was fit to these data points such that the relationship between residual strain and pre-strain in the 100% martensitic nitinol can be expressed as

$$\gamma_{R_{max}}(\gamma_p) = 0.065 + 0.065erf(10.32\gamma_p + 1.57), \tag{3.1}$$

where the subscript max on the γ_R term denotes the fact that this function only applies to the case of 100% martensitic nitinol ($\xi_0 = 1$). As the martensite fraction decreases, some of the residual strain is recovered. Hence, the residual strain is a function of both γ_p and ξ_0.

Any slight presence of austenite causes a sharp decrease in the residual strain, as evidenced by the isoresistive test data from the previous chapter. For this work, a simple exponential function was used to describe the relationship between ξ_0 and γ_R. The exponential function parameters were found by selecting the best fit to the isoresistive mechanical test data from the previous chapter. The residual strain can

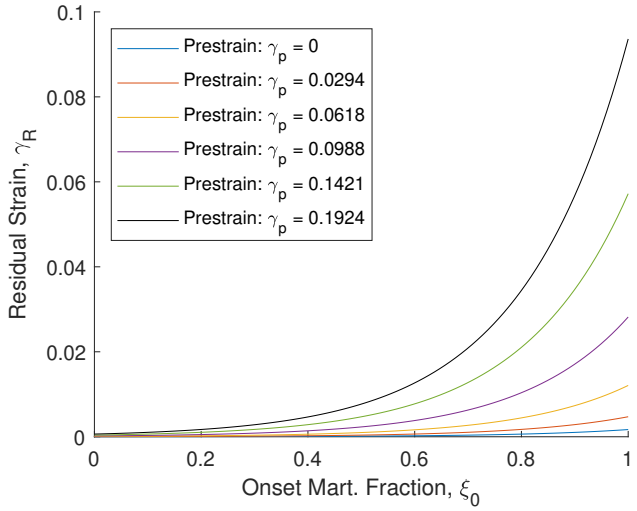

Figure 3.5: Residual strain in 35° nitinol springs from Eq. 3.2 as a function of pre-strain and onset martensite fraction.

then be calculated from the function

$$\gamma_R(\xi_0, \gamma_p) = \gamma_{R_{max}}(\gamma_p) e^{5(\xi_0 - 1)}. \tag{3.2}$$

As shown in Figure 3.5, this function accounts for the effects of both the martensite fraction and the amount of pre-strain causing the residual strain.

The unloading and reloading of martensitic nitinol after a pre-strain follows a nearly linear path, parallel to the elastic loading curve until this linear curve intersects the zero pre-strain loading curve. This intersection point is denoted by γ_i. The stress-strain curve for any martensite fraction ξ_0 and residual strain γ_R can then be computed with a piecewise function that accounts for the linear elastic region as well

as the nonlinear region at higher strains:

$$\tau(\xi_0, \gamma_R) = G(\xi_0)(\gamma - \gamma_R), \qquad \gamma < \gamma_i$$

$$\tau(\xi_0, \gamma_R) = G(\xi_0) - \xi_0[G_m\gamma_L]\xi_{s_m}(\gamma) - [1-\xi_0][G_a\gamma_L]\xi_{s_a}(\gamma), \qquad \gamma > \gamma_i \quad (3.3)$$

where $G(\xi_0)$ is defined according to the Voigt scheme as

$$G(\xi_0) = \xi_0 G_m + [1-\xi_0]G_a, \quad (3.4)$$

and the detwinning profiles $\xi_{s_m}(\gamma)$ and $\xi_{s_a}(\gamma)$ are defined in the previous chapter. By combining the residual strain function with the mechanical model from the previous chapter, the loading/unloading curves can be plotted as a function of the onset martensite fraction ξ_0 as shown in Figure 3.6.

The onset martensite fraction ξ_0 can be obtained from the shear strain and the electrical resistivity of the nitinol. As outlined in the previous chapter, the onset martensite fraction is given by

$$\xi_0(\rho, \gamma) = \left[\frac{\rho - \rho_a(\xi_{s_a}(\gamma))}{\rho_m(\xi_{s_m}(\gamma)) - \rho_a(\xi_{s_a}(\gamma))}\right]^{\left(a+[1-a][\gamma/\gamma_{max}]^b\right)^{-1}}, \quad (3.5)$$

with parameters a and b defined in the previous chapter.

To compute the actual spring force exerted at a given spring strain, the spring

strain ϵ can be converted to a material shear strain using the geometric relationships from the previous chapter. This spring strain, along with the measured electrical resistivity ρ can be substituted into Eq. 3.5 to obtain the onset martensite fraction. The onset martensite fraction, paired with the residual strain, can be used to calculate the shear stress in the nitinol, according to Eq. 3.3. Finally, the shear stress can be used to calculate the nitinol spring force using the equation

$$F_N(\tau) = \frac{\pi d^2 \tau}{8CW}, \tag{3.6}$$

with parameters explained in the previous chapter.

Recovery of residual strain with heating/cooling

Since the nitinol springs are pre-strained to $\gamma_p = 0.1924$ before being attached to the PneuSMA actuators, they begin with a residual strain of $\gamma_R = 0.089$, which corresponds to 300% spring strain. Thus, the initial heating and/or loading of the nitinol springs follows the black curves from Figure 3.6 which represent loading at different temperatures after an initial pre-strain of 0.1924.

It is important to note that heating the nitinol springs causes some of this inital residual strain to be recovered. For example, a PneuSMA actuator spring that is heated from $\xi_0 = 1$ to $\xi_0 = 0.4$ will transition between the black curves from Figure 3.6, also shown on the left side of Figure 3.7. When $\xi_0 = 0.4$ is reached, most of the

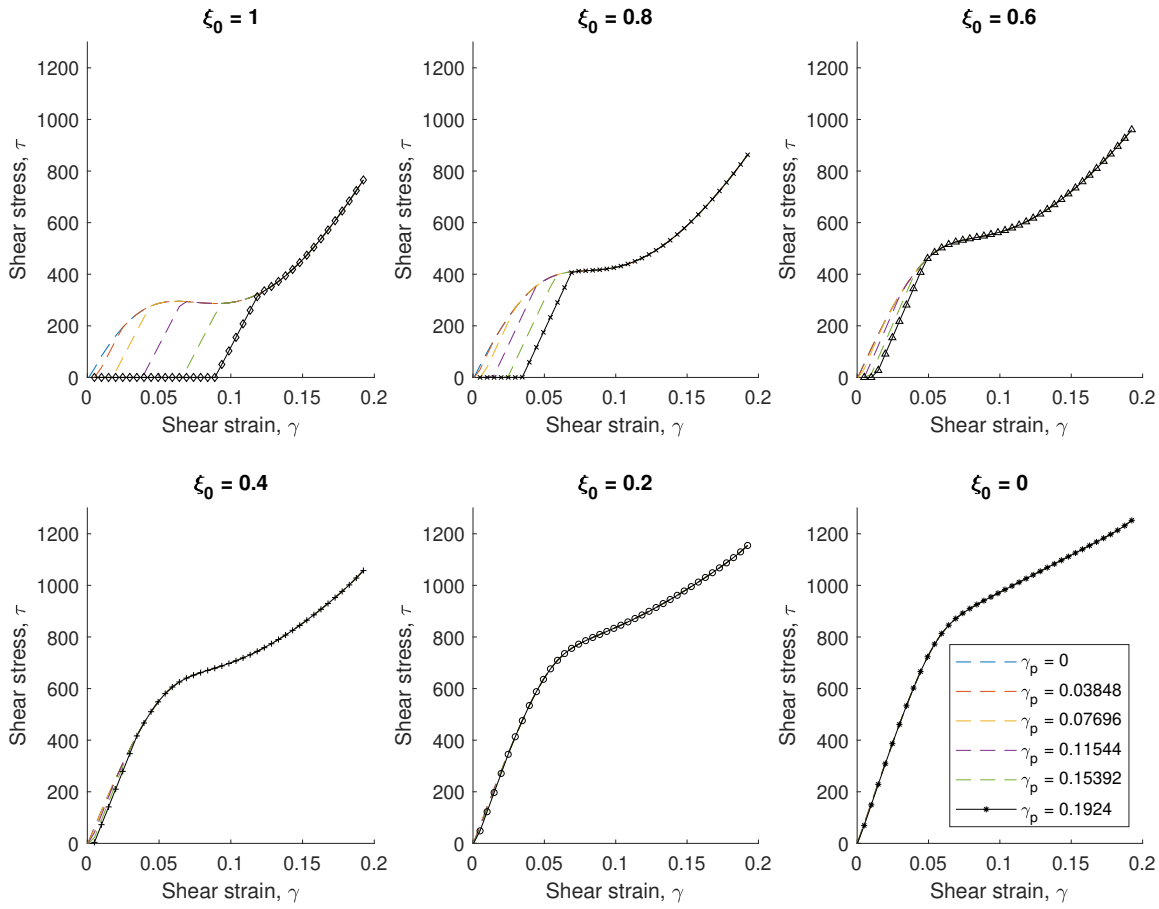

Figure 3.6: Stress-strain curves generated from Eq. 3.3 for various pre-strains at different onset martensite fractions. Bold black curves represent initial conditions in PneuSMA actuator springs which have been pre-strained to $\gamma_p = 0.1924$.

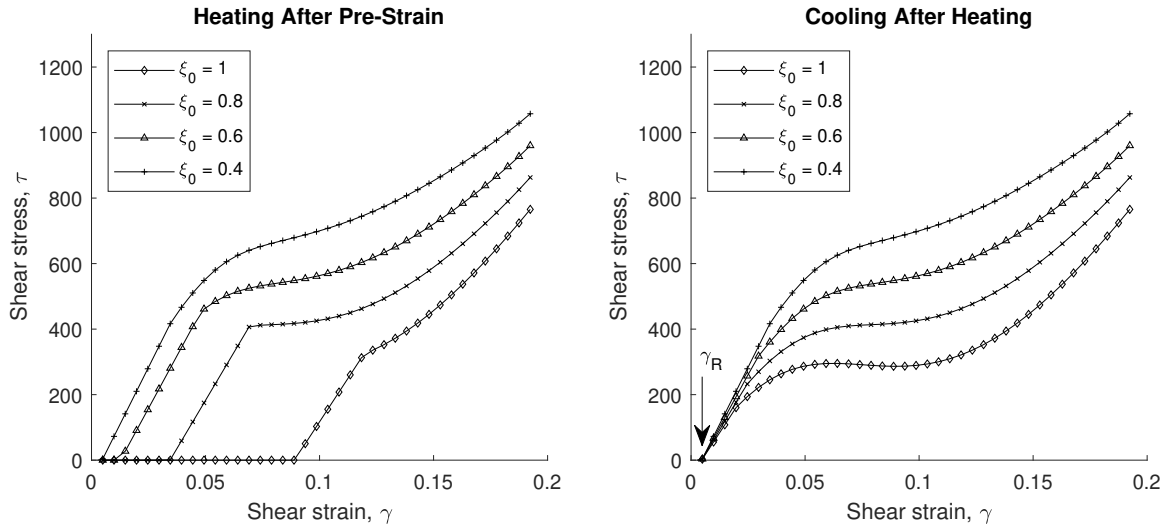

Figure 3.7: Stress-strain curves for PneuSMA actuator springs that are pre-strained to $\gamma_p = 0.1924$. Left: recovery of residual strain upon heating from $\xi_0 = 1$ to $\xi_0 = 0.4$. Right: keeping of residual strain γ_R during cooling from $\xi_0 = 0.4$ to $\xi_0 = 1$.

initial residual strain is recovered, leaving only 0.0049 residual strain, based on the residual strain function from Eq. 3.2, as shown in the leftmost curve in Figure 3.7. If the spring is then cooled, it does not revert to its original residual strain but instead resumes from its new residual strain of 0.0049 as it transitions from the $\xi_0 = 0.4$ to $\xi_0 = 1$ curves on the right side of Figure 3.7. This residual strain recovery must be accounted for in the modeling of the PneuSMA actuator.

3.4.2 Silicone characterization

As mentioned previously, various hyperelasticity models have been fit to experimental tension data from different silicone materials [114, 117]. While these hypere-

lasticity model parameters are readily available, they do not apply under compressive loadings. Thus, experimental characterization of the Dragon Skin 10 FAST silicone was conducted in this work. Each test was conducted using a Mark10 test stand to stretch/compress the samples and monitor the force throughout the tests.

Silicone mechanical test methods

Five different types of mechanical tests were conducted on the Smooth-On^{TM} Dragon Skin 10 FAST silicone to capture every aspect of its deformation behavior. First, standard uniaxial tension tests were conducted on thin dog bone samples and repeated with 5 different identical test specimens. Samples were cast with dimensions in accordance with the ASTM D412 standard for tensile testing of elastomeric materials [54], and the gauge length between the two tracking dots was measured using image processing from videos taken during testing. Samples were stretched to about 2.5 times their original length, then unloaded. Standard bulk compression tests were also conducted on solid cylindrical samples with 29mm diameter and 12.5mm thickness, in accordance with the ASTM D575 standard for testing rubber properties in compression [53]. The bulk compression samples were compressed down to about 40% of their original height while loaded between well-lubricated surfaces to prevent sticking and bulging of the sides. The bulk compression tests were repeated with five different identical samples for repeatability. The samples and test setup for the standard uniaxial tension and standard bulk compression tests are shown in Figure

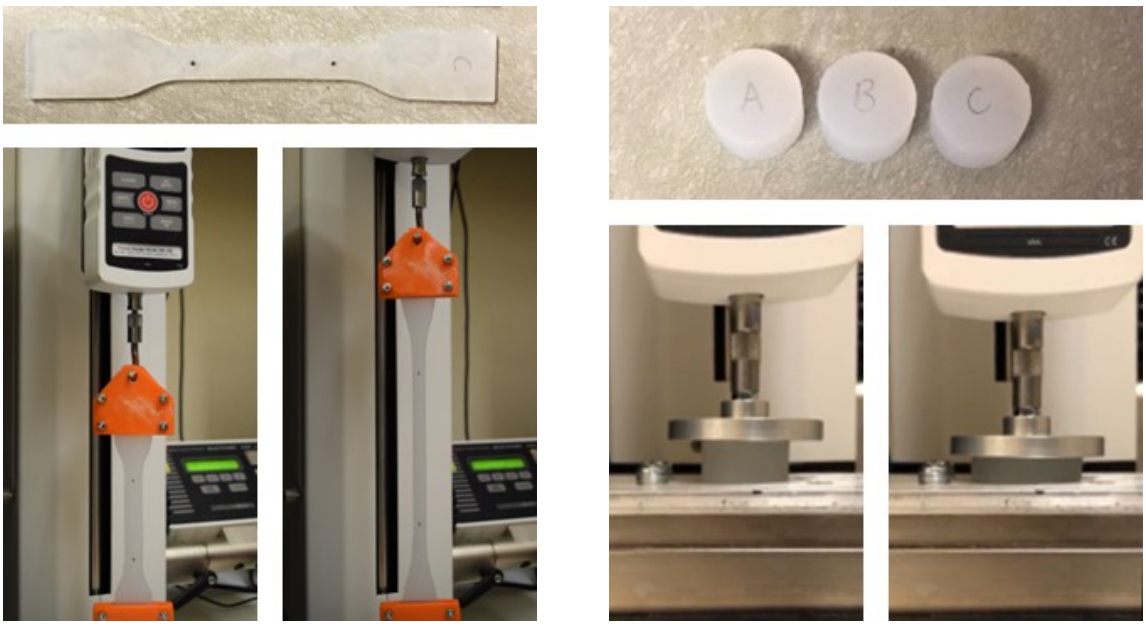

(a) Standard tension tests. **(b)** Standard bulk compression tests.

Figure 3.8: Samples and setup for standard tension and bulk compression testing of silicone material.

3.8.

To observe the effects of the fiber wrapping and the tube geometry, tension tests were also conducted on a silicone tube with circumferential fiber wrapping. The tension test tube was cast with a 10mm outer diameter, 1mm wall thickness, and 56mm length (not including end caps). Small neodymium magnets were placed inside, then the tube was sealed with silicone on both ends and wrapped with polyester fibers in the standard double helix pattern with 2mm between each wrap (3.6° fiber pitch). A small hollow needle was inserted in one end to vent the air during testing. The tube was secured to the test stand using magnets at each end, as shown in Figure

3.9 (a). The tube was then stretched to about 1.75 times its original length, then unloaded. This test was repeated three times with the same sample for repeatability.

To characterize the buckling behavior, buckling tests were conducted on fiber-wrapped silicone tubes with two different constraint types: a tube constraint and needle constraints. For the tube-constrained buckling tests, a silicone tube with 10mm outer diameter, 1mm wall thickness, 56mm length, and standard 3.6° fiber pitch was fabricated and placed inside an 11mm lubricated, rigid plastic tube. A 10mm rigid plastic cylinder was then lowered on the sample to compress/buckle the silicone inside the rigid tube, as shown in Figure 3.9 (b). The compression tube buckling tests were repeated three times with the same sample for repeatability. For the needle-constrained buckling tests, another silicone tube was created with the same dimensions. For this sample, the fibers were wrapped with with the same 3.6° pitch, but they were wrapped around two needles placed on opposite sides of the tube. The fibers were then secured with a thin layer of silicone applied just up to the needles such that the fibers could slide freely on the needles. The needle constraints were then loaded in a rigid 3D printed base, and a 10mm rigid cylinder was lowered to compress/buckle the tube as shown in Figure 3.9 (c). The compression needle buckling tests were repeated three times with the same sample for repeatability.

(a) Tube tension tests.

(b) Compression tube buckling tests.

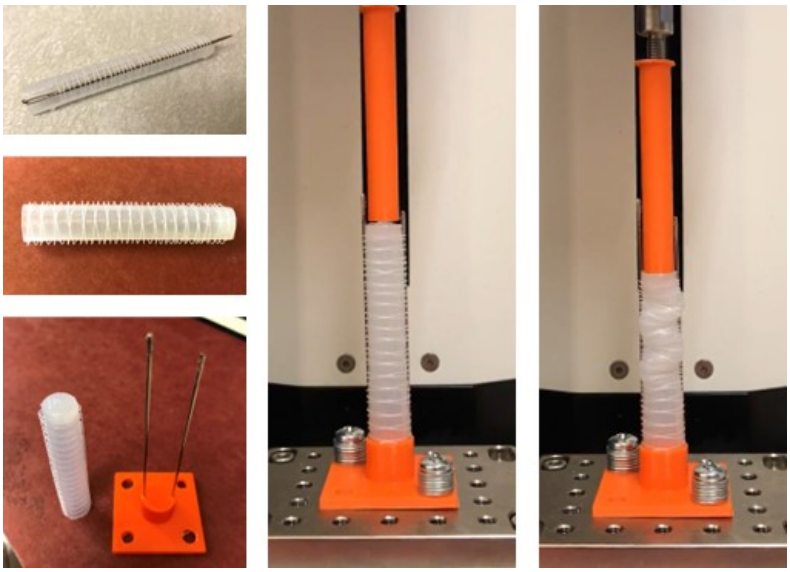

(c) Compression needle buckling tests.

Figure 3.9: Samples and setup for tension and buckling testing of fiber-wrapped silicone tubes.

Silicone mechanical test results

The stress-strain curves from each of the five silicone mechanical tests are shown in Figure 3.10, where dots represent data points and the solid curves are polynomial fits to each set of data. The polynomial fit coefficients for each curve are listed in Table 3.1, for the function form $\sigma = p_1\epsilon^n + p_2\epsilon^{n-1} + ... + p_n\epsilon + p_{n+1}$. In tension, the stress-strain curves from both the uniaxial tension and tube tension tests show the typical response of an elastomeric material with low stiffness, high toughness, and some strain stiffening as polymer chains align at higher strains. In compression, significant force is required to compress the solid cylindrical samples from the bulk compression tests; this is partly due to the incompressibility of silicone which requires significant radial expansion when the samples are compressed axially. When allowed to buckle, the force required to compress the silicone plateaus at a much smaller value as seen from both buckling tests. Note that the buckling behavior is highly geometry-dependent and was only measured for one particular tube geometry (10mm outer diameter, 1mm wall thickness, 56mm length, and 3.6° fiber pitch). Nevertheless, the same general flattening pattern can be expected in other geometries.

The Neo-Hookean hyperelasticity model is often used to characterize silicone tensile stress. Neo-Hookean model parameter for common silicone materials, including Dragon Skin 10 are reported in the literature [37, 193, 153]. The Neo-Hookean model parameter can also be obtained from a least squares fit to the experimental uniaxial

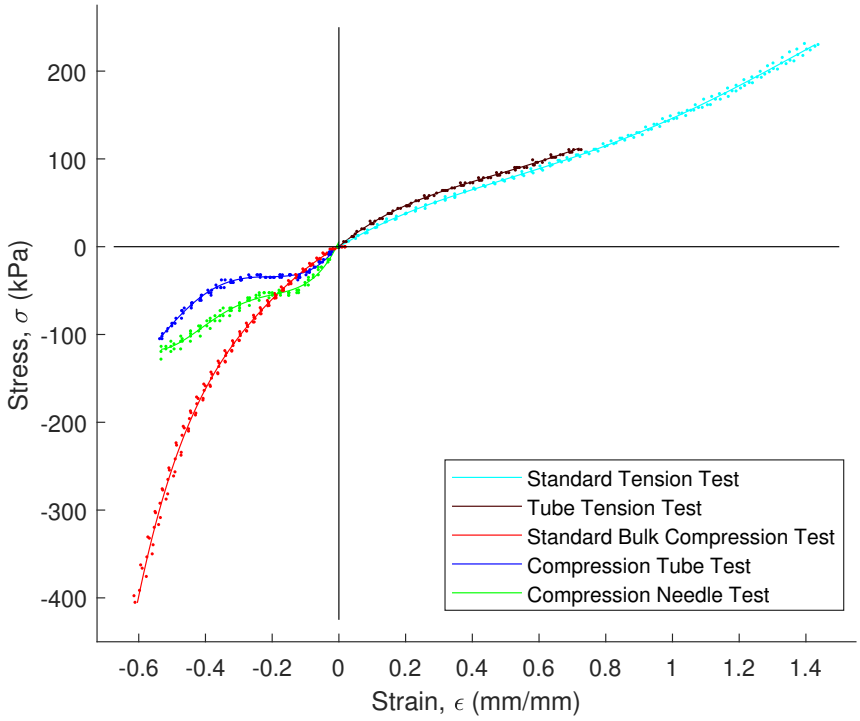

Figure 3.10: Stress-strain data from five different mechanical tests on Dragon Skin 10 FAST silicone.

Table 3.1: Polynomial fits to Dragon Skin 10 FAST silicone mechanical test data.

Test Name	Symbol	Polynomial Order	Polynomial Coefficients (kPa)	Strain Domain (mm/mm)
Standard uniaxial tension	$\sigma_{ST}(\epsilon)$	4	$p_{1_{ST}} = -63.4249$ $p_{2_{ST}} = 239.8487$ $p_{3_{ST}} = -264.5191$ $p_{4_{ST}} = 234.7951$ $p_{5_{ST}} = -0.3729$	[0,1.5]
Standard bulk compression	$\sigma_{SC}(\epsilon)$	4	$p_{1_{SC}} = -3295.1547$ $p_{2_{SC}} = -2066.7864$ $p_{3_{SC}} = -857.0668$ $p_{4_{SC}} = 180.3670$ $p_{5_{SC}} = -0.6563$	[-0.6,0]
Tube tension	$\sigma_{TT}(\epsilon)$	4	$p_{1_{TT}} = -194.6468$ $p_{2_{TT}} = 551.3092$ $p_{3_{TT}} = -519.7024$ $p_{4_{TT}} = 316.4992$ $p_{5_{TT}} = 0.2527$	[0,0.75]
Compression tube buckling	$\sigma_{CT}(\epsilon)$	5	$p_{1_{CT}} = -2446.9140$ $p_{2_{CT}} = 939.3898$ $p_{3_{CT}} = 5186.8161$ $p_{4_{CT}} = 2781.7816$ $p_{5_{CT}} = 547.5522$ $p_{6_{CT}} = 3.3046$	[-0.55,0]
Compression needle buckling	$\sigma_{CN}(\epsilon)$	4	$p_{1_{CN}} = 9176.3472$ $p_{2_{CN}} = 11193.7489$ $p_{3_{CN}} = 4470.7769$ $p_{4_{CN}} = 822.4502$ $p_{5_{CN}} = 5.7573$	[-0.55,0]

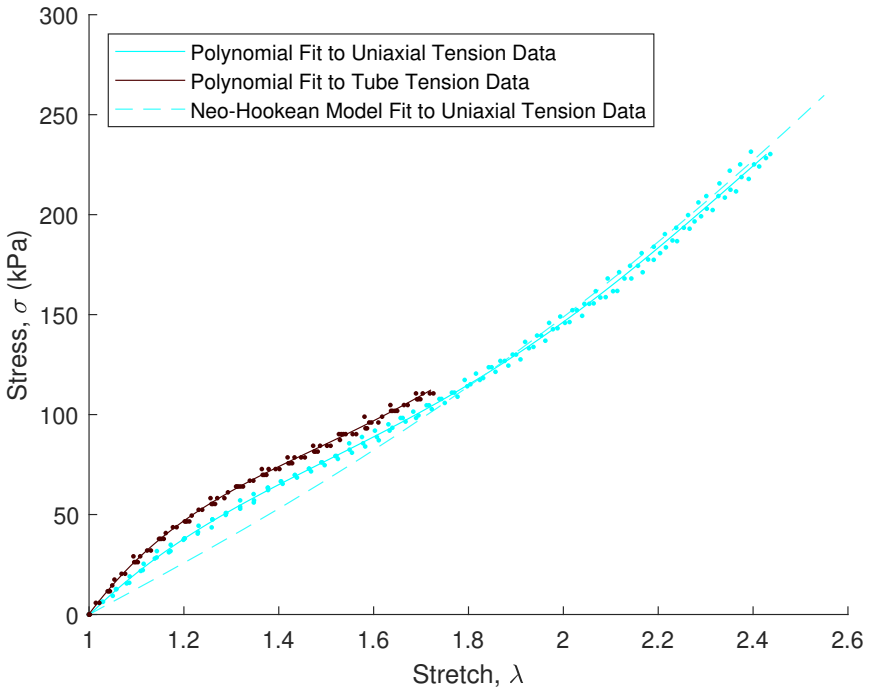

Figure 3.11: Stress-stretch data from uniaxial tension and tube tension tests, along with Neo-Hookean hyperelasticity model fit to uniaxial tension data.

tension data; the least-squares fit to the experimental data produced nearly identical model parameters, listed in Table 3.2. For comparison, the Neo-Hookean model with literature-accepted parameters is plotted with the experimental tension data in Figure 3.11. Some error is seen between the experimental data and the Neo-Hookean at low strains, but the model captures the general behavior of the material. A closer fit can be obtained using a polynomial fit to the uniaxial tension data; these polynomial coefficents are given in Table 3.1.

Table 3.2: Neo-Hookean hyperelasticity model parameters for Dragon Skin 10 silicone.

Strain Energy Function	Uniaxial Stress Function	Model Coefficients (MPa)	Source
$W = \mu(I_1 - 3)$	$\sigma_{uniax} = \mu(\lambda^2 - \frac{1}{\lambda})$	$\mu = 0.04250$ $\mu = 0.04237$	Literature-reported [37, 193, 153] Least squares fit to uniaxial tension data

Silicone tube elongation

It is also important to note that the silicone tube tension data follows almost exactly the same path as the uniaxial tension data, as seen in Figs. 3.10 and 3.11. This suggests that, under tension, the material in the silicone tube experiences nearly perfect uniaxial stress (i.e. circumferential and radial stresses are vanishing). To confirm the viability of the uniaxial stress assumption, the elongation of a fiber-wrapped silicone tube was measured while the internal pressure was swept from 0 to 50 kPa and back. Assuming uniaxial stress, the internal tensile force in the silicone walls can be computed from the polynomial fit to the uniaxial tension data from Table 3.1:

$$F_{sil} = \sigma_{uniax} A_{sil} = \left(p_{1_{ST}}\epsilon^4 + p_{2_{ST}}\epsilon^3 + p_{3_{ST}}\epsilon^2 + p_{4_{ST}}\epsilon + p_{5_{ST}}\right) \frac{\pi}{4}(d_o^2 - d_i^2). \tag{3.7}$$

The force on the end cap of the actuator from the internal pressure can then be calculated from

$$F_P = PA_{end} = P\frac{\pi}{4}d_i^2. \tag{3.8}$$

The resulting predicted length can then be determined by solving for the axial strain ϵ that balances the end force with the tensile force in the silicone walls by setting Eqs. 3.7 and 3.8 equal to one another:

$$Pd_i^2 = \left(p_{1_{ST}}\epsilon^4 + p_{2_{ST}}\epsilon^3 + p_{3_{ST}}\epsilon^2 + p_{4_{ST}}\epsilon + p_{5_{ST}}\right)(d_o^2 - d_i^2), \tag{3.9}$$

The expected length of the tube can then be computed from the strain using

$$L_{predicted} = L_0(1+\epsilon). \tag{3.10}$$

An alternative method for modeling the stress in the silicone material involves computing the principal stresses from the strain energy function. Using an incompressible Neo-Hookean model, the strain energy is given by

$$W = \frac{\mu}{2}(I_1 - 3), \tag{3.11}$$

where I_1 is the first invariant of the three principal stretches, given by

$$I_1 = \lambda_1^2 + \lambda_2^2 + \lambda_3^2, \tag{3.12}$$

where λ_1, λ_2, and λ_3 are the principal stretches in the axial, circumferential, and radial directions, respectively. Given the circumferential fiber constraint, the strain in the circumferential direction can be neglected; hence, $\lambda_2 = 1$. The strain in the radial direction can be determined by applying the incompressibility assumption, which requires that $\lambda_1\lambda_2\lambda_3 = 1$; hence, $\lambda_3 = 1/\lambda_1$. Assuming negligible stresses in the radial and circumferential direction then leaves the principal stress in the axial direction which is given by

$$\sigma_1 = \frac{\partial W}{\partial \lambda_1} - \frac{P}{\lambda_1} = \mu\left(\lambda_1 - \frac{1}{\lambda_1^3}\right), \tag{3.13}$$

where P is the Lagrange multiplier and μ is the effective initial shear modulus from the Neo-Hookean model. Using this silicone stress model, the expected elongation of the silicone tube can again be calculated by balancing the silicone tensile force $\sigma_1 A_{sil}$ with the force on the end of the tube due to the internal pressure. The following force balance equation can then be solved for λ_1:

$$P d_i^2 = \mu\left(\lambda_1 - \frac{1}{\lambda_1^3}\right)(d_o^2 - d_i^2). \tag{3.14}$$

After solving for λ_1, the resulting predicted length of the tube can be calculated from

$$L_{predicted} = L_0 \lambda_1. \tag{3.15}$$

Excellent agreement is seen between the measured length from the tube elongation tests and the predicted length from the uniaxial stress assumption from Eqs. 3.9 and 3.10, as shown in Figure 3.12. The predicted length from the Neo-Hookean model with plane strain assumption calculated from Eqs. 3.14 and 3.15 does not track as well with the experimental data. These results indicate that the effects of the pressure on the walls of the silicone and the circumferential force from the fiber wrapping have negligible effects on the stress in the silicone material, and the uniaxial stress assumption is more acurate for modeling the stress in the silicone tube. Thus, it is reasonable to use the polynomial fit to the uniaxial tension data for modeling purposes without needing to fit a hyperelasticity model or compute complicated stress states from a strain energy function.

3.5 Analytical model for PneuSMA actuator

In this section, a quasi-static analytical model is developed to describe the relationship between internal pressure, nitinol spring activation, and resulting length and bending of the PneuSMA actuator. The analytical model takes into account the silicone hyperelasticity, actuator geometry, and temperature-dependent properties of

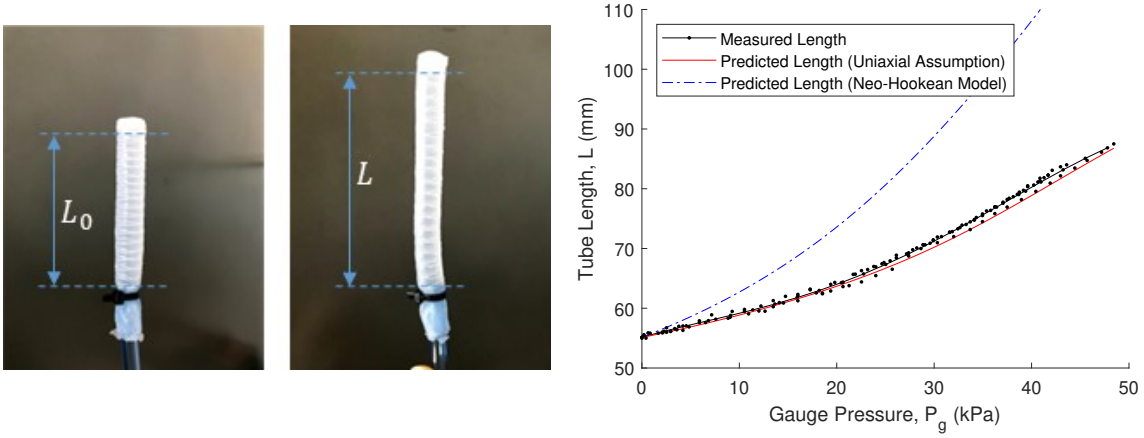

(a) Measurement of silicone tube elongation. **(b)** Silicone tube length versus internal pressure.

Figure 3.12: Silicone tube elongation tests compared with predicted elongation from uniaxial stress assumption and Neo-Hookean model.

nitinol using geometric dimensions and material parameters that were determined from characterization expriments in sections 3.4.1 and 3.4.2, and in the previous chapter. Polygerinos et al. presented a straightforward analytical modeling approach for tubular fiber-reinforced soft pneumatic actuators [138]. Substantial modifications and extensions to the Polygerinos model are necessary to incorporate the effects of the nitinol springs. Although the analytical model presented by Polygerinos et al. only applies to simple fiber-reinforced bending actuators, it undergirds the PneuSMA actuator model developed in this work and should be cited for its influence on the present work [138].

The analytical PneuSMA model presented below describes the bending of a single segment of a PneuSMA actuator. The PneuSMA actuator is capable of achieving

multi-directional bending and different curvatures along the length of the actuator by selectively heating different segments of the nitinol springs. To model this full behavior, the PneuSMA model must be applied separately to each discrete segment of the actuator. The model itself requires uniform heating (and hence uniform curvature) along the entire length considered.

3.5.1 State variables and curvature parameters

The state variables δ_1 and δ_2 are used to fully describe the configuration of the PneuSMA actuator under any given pressure and SMA activation conditions. As shown in Figure 3.13, δ_1 and δ_2 are the elongations of the left and right sides of the actuator, respectively. The elongation values can be positive or negative depending on the input conditions.

The configuration variables of interest are the curvature κ or radius of curvature r, and the bend angle θ_{end} or resulting length L. Although only two variables are required to fully define the configuration, all four represent useful quantities and are worth expressing. Each of the configuration variables can be related to the state variables δ_1 and δ_2 by simple geometric analysis.

First, the centerline length L of the actuator can be found by averaging the two side lengths:

$$L = L_0 + \frac{\delta_1 + \delta_2}{2}, \tag{3.16}$$

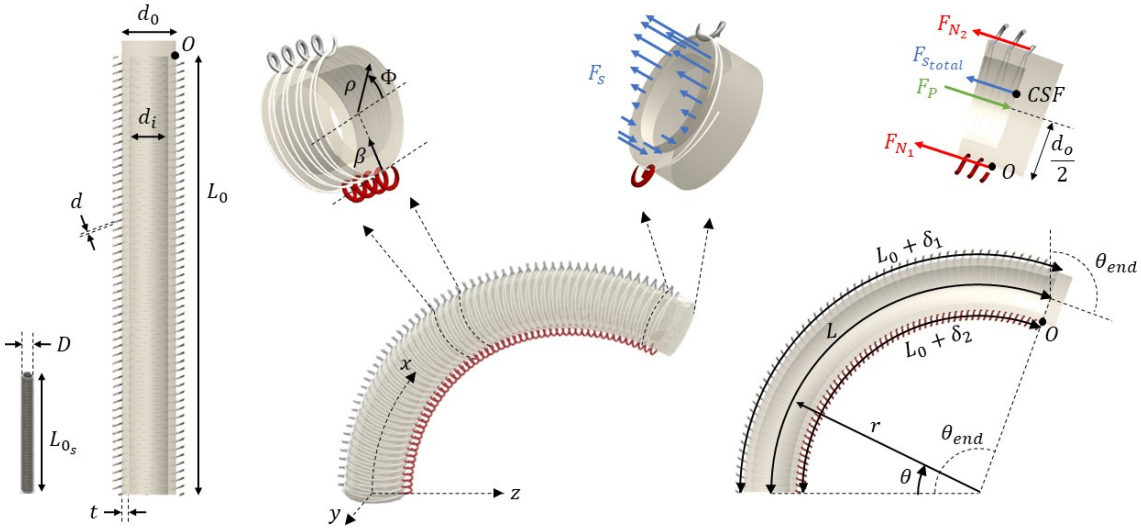

Figure 3.13: Left: dimensions of nitinol springs and silicone tube. Center: coordinate system used for analytical modeling. Top center: silicone force distribution throughout cross-section for bending actuation. Right: configuration variables and curvature parameters. Top right: force balance on actuator cap.

where L_0 is the initial length of the actuator, prior to heating/pressurization. The bend angle θ_{end} and radius of curvature r can be determined by analyzing the similar arcs formed by the left and right edges of the actuator, which share the same central angle θ_{end}. Applying the circular arc length formula to each arc gives

$$L_0 + \delta_1 = \left(r + \tfrac{d_o}{2}\right)\theta_{end}, \tag{3.17}$$

$$L_0 + \delta_2 = \left(r - \tfrac{d_o}{2}\right)\theta_{end}, \tag{3.18}$$

where d_o is the outer diameter of the silicone tube. Eliminating r from Eqs. 3.17 and 3.18 gives the bend angle formula

$$\theta_{end} = \frac{\delta_1 - \delta_2}{d_o}. \tag{3.19}$$

Similarly, eliminating θ_{end} from Eqs. 3.17 and 3.18 gives the radius of curvature r as a function of δ_1 and δ_2:

$$r = \frac{d_o(L_0 + \delta_2)}{\delta_1 - \delta_2}. \tag{3.20}$$

The curvature κ is defined as the inverse of the bend radius:

$$\kappa = 1/r = \frac{\delta_1 - \delta_2}{d_o(L_0 + \delta_2)}. \tag{3.21}$$

3.5.2 Silicone force distribution

The force in the walls of the silicone tube varies substantially thoughout the cross-section. The highest tensile force occurs along the edge with the highest elongation. The minimum tensile force, or greatest compressive force, occurs on the opposite side of the actuator where elongation is lowest (or negative) due to SMA activation or other strain limiting effect. The silicone force varies nonlinearly between these two extremes, as shown in the top middle of Figure 3.13.

In Section 3.4.2, it was shown that a uniaxial stress state provides a good representation of the axial stress in the silicone tube. Thus, the axial stress in the silicone can be calculated using the polynomial stress functions from Table 3.1 based on the elongation δ at any point, such that

$$\begin{aligned} \sigma_s(\delta) &= \sigma_{ST}\left(\tfrac{\delta}{L_0}\right), && \delta > 0 \\ &= p_{1_{ST}}\left(\tfrac{\delta}{L_0}\right)^4 + p_{2_{ST}}\left(\tfrac{\delta}{L_0}\right)^3 + p_{3_{ST}}\left(\tfrac{\delta}{L_0}\right)^2 + p_{4_{ST}}\left(\tfrac{\delta}{L_0}\right) + p_{5_{ST}}, && \delta > 0 \end{aligned} \tag{3.22}$$

$$\begin{aligned} \sigma_s(\delta) &= \sigma_{CN}\left(\tfrac{\delta}{L_0}\right), && \delta < 0 \\ &= p_{1_{CN}}\left(\tfrac{\delta}{L_0}\right)^4 + p_{2_{CN}}\left(\tfrac{\delta}{L_0}\right)^3 + p_{3_{CN}}\left(\tfrac{\delta}{L_0}\right)^2 + p_{4_{CN}}\left(\tfrac{\delta}{L_0}\right) + p_{5_{CN}}, && \delta < 0 \end{aligned} \tag{3.23}$$

Similarly, the differential silicone force at any point can be computed as a function

of the elongation δ at that particular location using

$$dF_s(\delta) = \sigma_{ST}\left(\frac{\delta}{L_0}\right) dA, \qquad \epsilon > 0 \tag{3.24}$$

$$dF_s(\delta) = \sigma_{CN}\left(\frac{\delta}{L_0}\right) dA, \qquad \epsilon < 0 \tag{3.25}$$

where $\sigma_{ST}(\delta/L_0)$ and $\sigma_{CN}(\delta/L_0)$ are the polynomial stress functions from Table 3.1 from the standard uniaxial tension and compression needle buckling test data.

The elongation as a function of β can be determined from interpolation between δ_1 and δ_2:

$$\delta(\beta, \delta_1, \delta_2) = \delta_2 + \beta\frac{\delta_1 - \delta_2}{d_o}. \tag{3.26}$$

The coordinate β can be exressed in terms of cylindrical coordinates ρ and ϕ as

$$\beta(\rho, \phi, \delta_1, \delta_2) = \frac{d_o}{2} + \rho\sin(\phi). \tag{3.27}$$

The elongation as a function of ρ and ϕ is then found by combining Eqs. 3.26 and 3.27 to obtain

$$\delta(\rho, \phi, \delta_1, \delta_2) = \delta_2 + \left[\frac{d_o}{2} + \rho\sin(\phi)\right]\frac{\delta_1 - \delta_2}{d_o}. \tag{3.28}$$

The total silicone force can then be calculated by integrating over the entire cross

section:

$$
\begin{aligned}
F_{s_{total}}(\delta_1, \delta_2) &= \int dF_s(\delta) \\
&= \int \left[\sigma_s \left(\frac{\delta(\rho,\phi,\delta_1,\delta_2)}{L_0}\right)\right] dA \\
&= \int_0^{2\pi}\int_{\rho_i}^{\rho_o} \left[\sigma_s\left(\frac{\delta_2+[d_o/2+\rho\sin(\phi)][\delta_1-\delta_2]/d_o}{L_0}\right)\right] r dr d\phi,
\end{aligned} \tag{3.29}
$$

where ρ_i and ρ_o are the inner and outer radii of the silicone tube, respectively, and the σ_s function calls Eqs. 3.22 and 3.23.

If desired, the silicone distributed load can be replaced by a point load of $F_{s_{total}}$ applied at the location of the centroid of the silicone distributed load. The β-coordinate of the centroid of silicone force (CSF) can be computed from

$$
\begin{aligned}
CSF(\delta_1, \delta_2) &= \frac{\int \sigma_s \beta dA}{F_{s_{total}}} \\
&= \frac{\int_0^{2\pi}\int_{\rho_i}^{\rho_o}\left[\sigma_s\left(\frac{\delta_2+[d_o/2+\rho\sin(\phi)][\delta_1-\delta_2]/d_o}{L_0}\right)\right]\left[\frac{d_o}{2}+\rho\sin(\phi)\right] r dr d\phi}{F_{s_{total}}(\delta_1,\delta_2)}.
\end{aligned} \tag{3.30}
$$

3.5.3 Bending moment balance

The quasi-static analytical model relies on the assumption that the deformation rate is slow enough that inertial force can be ignored and a static analysis can sufficiently capture the behavior of the device. Under this assumption, a moment balance about the fulcrum O provides a necessary constraint equation for the analytical model.

As seen in the top right of Figure 3.13, the nitinol spring force, silicone material internal force, and the force due to pressure on the end cap each contribute a bending moment about point O.

The moment due to the pressure on the end of the actuator can be expressed simply as

$$M_P(P) = PA_{end}\frac{d_o}{2} = P\left[\frac{\pi}{4}d_i^2\right]\frac{d_o}{2}. \tag{3.31}$$

The nitinol spring on the right side of the actuator does not contribute a bending moment about point O as point O lies on the line of action of the right-hand nitinol spring force F_{N_2}. The other nitinol spring does cause a bending moment about point O which can be expressed as

$$M_{N_1}(R_1, \delta_1) = -F_{N_1}(R, \delta_1)\, d_o, \tag{3.32}$$

where F_{N_1} is the temperature- and strain- dependent force in the left-hand nitinol spring. The nitinol spring force computation is outlined in Section 3.4.1, using Eqs. 3.1 through 3.6. The bending moment expression in Eq. 3.32 takes on a negative sign in keeping with the convention of positive clockwise bending moments.

The bending moment from the silicone material can be determined by integrating the distributed load and associated lever arm distances over the actuator cross section

using

$$M_s(\delta_1, \delta_2) = \int \sigma \beta dA$$

$$= \int \left[\sigma_s \left(\frac{\delta(\rho,\phi,\delta_1,\delta_2)}{L_0}\right)\right] \left[\beta(\rho, \phi, \delta_1, \delta_2)\right] dA$$

$$= \int_0^{2\pi}\int_{\rho_i}^{\rho_o} \left[\sigma_s\left(\frac{\delta_2+[d_o/2+\rho\sin(\phi)][\delta_1-\delta_2]/d_o}{L_0}\right)\right]\left[\frac{d_o}{2} + \rho\sin(\phi)\right] r dr d\phi, \tag{3.33}$$

or alternatively by using the total silicone force applied at the CSF from Eqs. 3.29 and 3.30:

$$M_s(\delta_1, \delta_2) = -F_{s_{total}}(\delta_1, \delta_2)\, CSF(\delta_1, \delta_2). \tag{3.34}$$

Equations 3.33 and 3.34 are interchangeable as they produce identical results.

Setting the sum of the moments about O equal to zero gives

$$M_P(P) = M_{N_1}(R_1, \delta_1) + M_s(\delta_1, \delta_2). \tag{3.35}$$

The state variables δ_1 and δ_2 must satisfy Eq. 3.35

3.5.4 Force balance

When modeling a simple fiber-reinforced bending actuator (with no SMA springs), a single state variable can be used to fully define the actuator's configuration as one side length is fixed by a strain-limiting fabric or fiber in the axial direction. Hence, the moment balance alone is sufficient for determining the state variable and modeling

the bending of simple fiber-reinforced bending actuators [138, 45]. The incorporation of SMA springs in place of simple fibers requires an additional state variable to fully describe the configuration of the actuator. Thus, modeling the PneuSMA actuator requires two equations in order to solve for the two state variables. Balancing the forces on the end of the actuator provides a second constraint equation that can be used in conjunction with the moment balance equation to solve for the two state variables.

From the top right of Figure 3.13, it can be seen that four forces act on the end of the actuator: the force from the pressure acting on the end of the silicone tube F_P, the force from the silicone tube $F_{s_{total}}$, and the forces from both nitinol springs F_{N_1} and F_{N_2}.

The force from the pressure acting on the end of the actuator was given previously in Eq. 3.8. The total silicone force was found by integrating the $\sigma_s(\delta)$ function across the cross section of the actuator, as shown in Eq. 3.29. The nitinol spring forces F_{N_1} and F_{N_2} are obtained from Eqs. 3.1 through 3.6, as outlined in Section 3.4.1. Setting the sum of the forces on the end of the actuator equal to zero gives the force balance equation

$$F_P(P) = F_s(\delta_1, \delta_2) + F_{N_1}(R_1, \delta_1) + F_{N_2}(R_2, \delta_2). \tag{3.36}$$

Solving the force and moment balance equations requires a numerical solver. The resulting configuration, as a function of pressure P and nitinol spring resistances

R_1 and R_2 can be obtained using a two-parameter minimization function such as MATLAB's $fminsearch$ function:

$$\begin{bmatrix} \delta_1(P, R_1, R_2) \\ \\ \delta_2(P, R_1, R_2) \end{bmatrix} = fminsearch \left(minFun(\delta_1, \delta_2), \begin{bmatrix} 0 \\ \\ 0 \end{bmatrix} \right), \tag{3.37}$$

where $minFun$ is the function to be minimized. The following minimization function it used to minimize both the sum of the moments and the sum of the forces:

$$\begin{aligned} minFun(\delta_1, \delta_2) &= [\Sigma F]^2 + [\Sigma M_O]^2 \\ &= [-F_P(P) + F_s(\delta_1, \delta_2) + F_{N_1}(R_1, \delta_1) + F_{N_2}(R_2, \delta_2)]^2 \\ &\quad + [-M_P(P) + M_{N_1}(R_1, \delta_1) + M_s(\delta_1, \delta_2)]^2 . \end{aligned} \tag{3.38}$$

Once the state variables δ_1 and δ_2 have been calculated using Eq. 3.37, the configuration can be expressed in more intuitive terms by converting to bend radius, curvature, actuator length, and/or bend angle using Eqs. 3.16, 3.19, 3.20, and 3.21.

3.5.5 Model adaptations for alternative designs

The PneuSMA quasi-static analytical model presented above was developed for a round PneuSMA actuator with two nitinol springs arranged opposite one another. With a few minor modifications, the model can easily be applied to a variety of different pneumatic actuator types, geometries, and spring arrangements.

PneuSMA actuator with single nitinol spring To model the bending of a PneuSMA actuator with a single spring on one side, the force and bending moment terms from one of the nitinol springs should be removed from the force and moment balance equations. In other words, F_{N_1} and M_{N_1} should be removed from Eqs. 3.35 and 3.36, as well as Eq. 3.38. Note that the single spring PneuSMA actuator is only capable of one-directional bending.

PneuSMA actuator with triad of nitinol springs The PneuSMA actuator is capable of three-dimensional bending when three nitinol springs are arranged in a triad configuration along the sides of the actuator. To model the 3D bending configuration, a third state variable δ_3 must be introduced to fully define the configuration. With each of the state variables tracking the elongation at each spring location, a third spring force term F_{N_3} must be added to the force balance equation. The silicone force and moment functions would need to be re-derived as their derivation relies on δ_1 and δ_2 being measured on opposite sides of the actuator. Additionally, the moment balance equation would need to include vector cross-products as the bending moments from the nitinol springs would no longer lie in the same plane.

Fiber-reinforced bending actuator with no nitinol springs The PneuSMA model can easily be simplified to predict the bending in a simple fiber-reinforced bending actuator with no nitinol springs. In these types of actuators, a strain-limiting fabric or fiber is embedded along one side to prevent axial elongation on one side.

The strain-limiting fiber is generally considered inextensible and can be modeled as a spring with infinitely high stiffness. Thus, the spring force and bending moment from one spring may be removed, and the force from the second spring can be replaced a Hooke's Law spring force equation. In other words, F_{N_1} and M_{N_1} should be removed from Eqs. 3.35 and 3.36, as well as Eq. 3.38, and the second spring force F_{N_2} can be replaced with

$$F_{N_2} = k_f \delta_2, \tag{3.39}$$

where the fiber stiffness k_f is sufficiently large to drive δ_2 to zero. A value of $k_f = 1 \times 10^6$ MPa was sufficient for the actuator geometry used in this work.

Pneumatic actuator with non-circular cross section A circular silicone tube was used as the basis for the PneuSMA actuators in this work as this geometry lends itself most easily to three-dimensional bending. However, other geometries with semi-circular, rectangular, or more advanced cross sections could also be used. Modifying the geometry would affect the force and moment from the pressure as the area of the end cap would change. Additionally, the silicone force would need to be integrated over a different cross-sectional area. Otherwise, the same modeling principles could be applied to different geometries, and the nitinol spring force and moment functions would remain unchanged.

3.6 Actuator fabrication

The fabrication process for the PneuSMA actuator has been refined after much trial-and-error to streamline the process and minimize opportunities for inconsistencies between samples. Figure 3.14 shows the step-by-step process for casting and assembling a PneuSMA actuator with two springs arranged opposite each other. As shown in Figure 3.14 (a), mold pieces of the desired dimensions are 3D printed using a rigid plastic material (ABS or PLA). The mold halves are designed with interlocking slots on both sides to ensure proper alignment. Two different mold cores are needed: one with a guide pin and one without. The guide pin is essential for keeping the core concentric with the outer mold pieces during the casting process to ensure uniform silicone wall thickness, and hence symmetric actuator bending. The pinless core is used later in the fabrication process when the pin hole is sealed.

The fabrication steps shown in Figure 3.14 are described below.

(a) Mold pieces, including two outer mold halves and two mold cores, are 3D printed using rigid plastic material (ABS or PLA) and sprayed with Mold Release spray.

(b) Mold halves are interlocked and clamped together (clamps not shown).

(c) Liquid silicone is mixed, degassed, and poured into the mold.

(d) The mold core with guide pin is inserted and clamped down (clamp not shown), and silicone is allowed to cure.

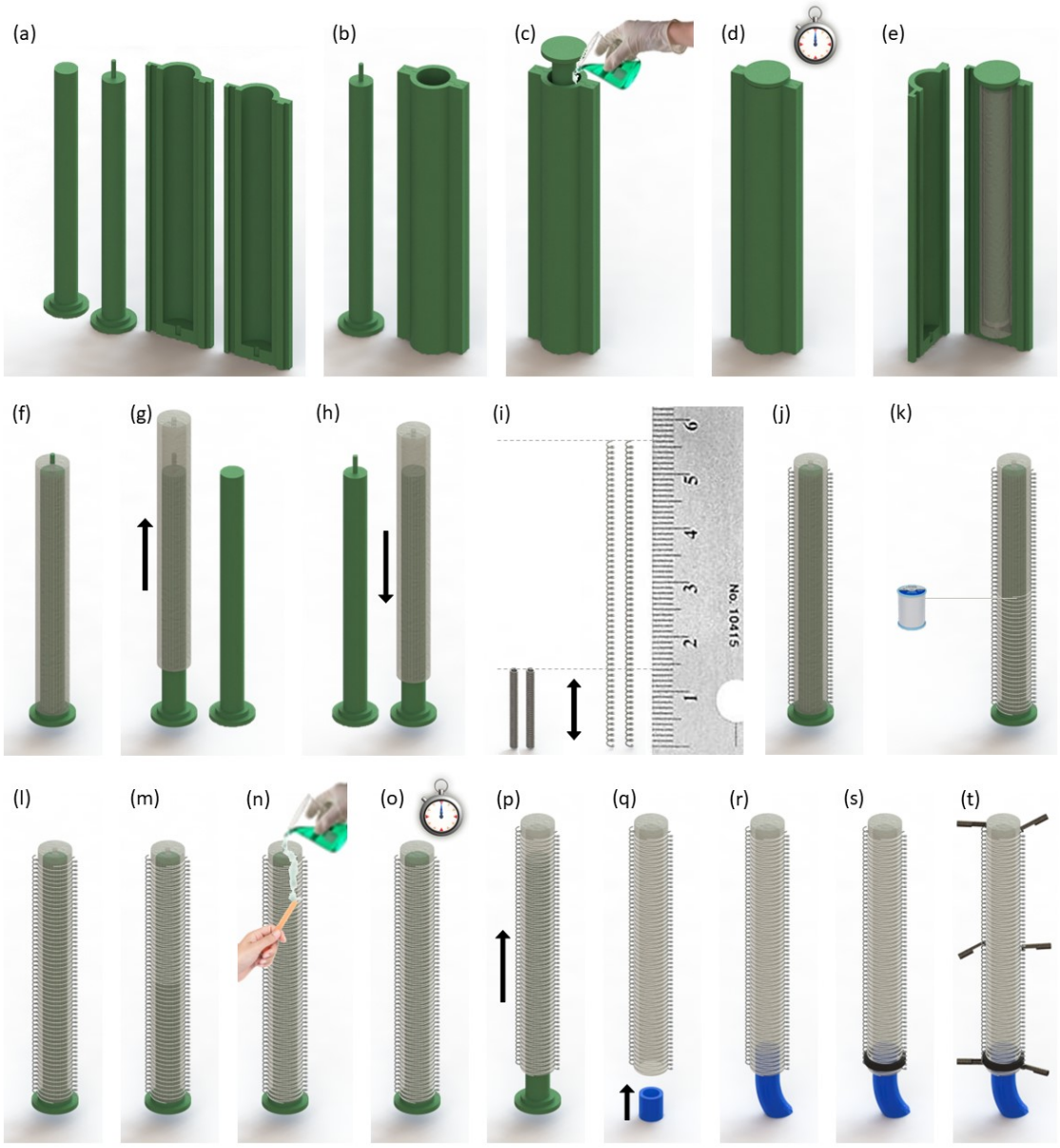

Figure 3.14: PneuSMA actuator fabrication process for 2-spring actuator. Steps (a)-(e) show the silicone tube casting; steps (i) - (j) show the pre-stretching and placement of the nitinol springs; steps (k) - (m) show the fiber wrapping process, and steps (n) - (t) show the silicone coating and the attatchment of the supply tube and electrical connectors.

(e) Mold is unclamped and opened using a slotted screwdriver to pull apart mold halves.

(f) Mold core with silicone tube is removed from outer mold pieces.

(g) Silicone tube is removed from mold core with guide pin.

(h) Silicone tube is transferred to pinless mold core.

(i) Nitinol springs are cut to 14mm (plus margin for connections) then stretched to 56mm (plus margin for connections)

(j) Pre-strained nitinol springs are temporarily taped along opposing sides of the silicone tube.

(k) Polyester thread is manually wrapped around the silicone tube, passing through every spring coil to ensure uniform spacing/pitch.

(l) Tape is removed as thread wrapping continues.

(m) After reaching the tip, the wrapping continues back down to the base, passing through each of the spring coils a second time to form a double helix wrapping.

(n) Thread ends are tied off, then a thin layer of silicone is spread over the fibers just up to the springs, and the pinhole is filled.

(o) The silicone coating is allowed to cure.

(p) The fiber-wrapped silicone tube is removed from the mold core.

(q) A thin layer of Sil-Poxy adhesive is spread on the outside of the end of the supply tube.

(r) The supply tube is inserted into the end of the actuator.

(s) The supply tube is secured with a Zip Tie, and the Sil-poxy is allowed to dry.

(t) Molex crimp terminals are attached at the ends and intermediate points on the nitinol springs.

Attaching the electrical wires to the nitinol springs is difficult due to the size, shape, and composition of the nitinol springs. Nitinol forms a thick oxide layer on the surface when exposed to air. While this feature contributes to desirable chemical stability and biocompatibility, it makes soldering nearly impossible. Since the oxide layer has a high electrical resistance, the best way to establish robust electrical connections is to use crimps that can penetrate the oxide layer and stabilize the connection. The springs used in this work were too small to crimp directly on the spring wire. Instead, a short segment of copper wire roughly matching the inner diameter of the nitinol coils was inserted in the last few coils on each end of the spring. A Molex crimp terminal could then be crimped around the end of the spring with the copper core inside as shown in Figure 3.15. To add connections at midpoints in the spring, the nitinol spring was lain across a Molex terminal with a copper wire segment

Figure 3.15: Electrical connections to nitinol springs created by crimping Molex crimp terminals around a copper core inserted into nitinol coils.

placed over top to sandwich the crimp against the spring as shown on the right side of Figure 3.15. This crimping method proved significantly more effective in reducing weight and contact resistance compared to soldering or conductive paste methods.

3.7 Experimental validation of analytical model

Experiments were conducted on five different variations of the PneuSMA actuator to validate the quasi-static analytical model. The measured curvature, length, and bend angle as a function of pressure and nitinol spring activation were compared with those predicted by the analytical model.

3.7.1 Sample preparation

The five variations of the PneuSMA actuator created for experimental testing are shown in Figure 3.16. The first three samples are called PneuFLEX actuators, a

Table 3.3: PneuSMA and PneuFLEX sample dimensions.

Sample Name	Sample Description	Strain Limiter(s)	Outer Diameter D_o	Wall Thickness t	Actuator Length L_0
PneuFLEX$_s$	PneuFLEX standard dims.	Inextensible fiber	10 mm	1 mm	56 mm
PneuFLEX$_t$	PneuFLEX thicker walls	Inextensible fiber	10 mm	1.5 mm	56 mm
PneuFLEX$_w$	PneuFLEX wider dims.	Inextensible fiber	14 mm	1 mm	56 mm
PneuSMA1	PneuSMA single spring	1 nitinol spring	10 mm	1 mm	56 mm
PneuSMA2	PneuSMA opposing springs	2 nitinol springs	10 mm	1 mm	56 mm

name coined by Deimel and Brock [45], to describe fiber-reinforced bending actuators that do not contain any SMA springs. Instead of nitinol springs, the PneuFLEX actuators have an inextensible fiber embedded along one side of the silicone tube to prevent elongation on one side and thus enable bending upon pressurization. The subscripts s, t, and w on the names of the PneuFLEX samples indicate the dimensions of the silicone tube cross section with s indicating standard dimensions, t indicating thicker walls, and w indicating a wider tube. The two PneuSMA actuators both have standard silicone tube dimensions, but the PneuSMA1 actuator has a single nitinol spring on one side while the PneuSMA2 actuator has two nitinol springs arranged on opposite sides of the tube. Each actuator was made with Smooth-On^{TM} Dragon Skin 10 FAST silicone and Kellog's Research Lab 35°C nitinol micro springs with 0.25mm wire diameter, 0.9mm mandrel diameter, and tight spring pitch such that there is no space between coils at rest length and hence the initial pitch is given by $p_i = d$. The dimensions and strain-limiting mechanisms for each actuator are listed in Table 3.3.

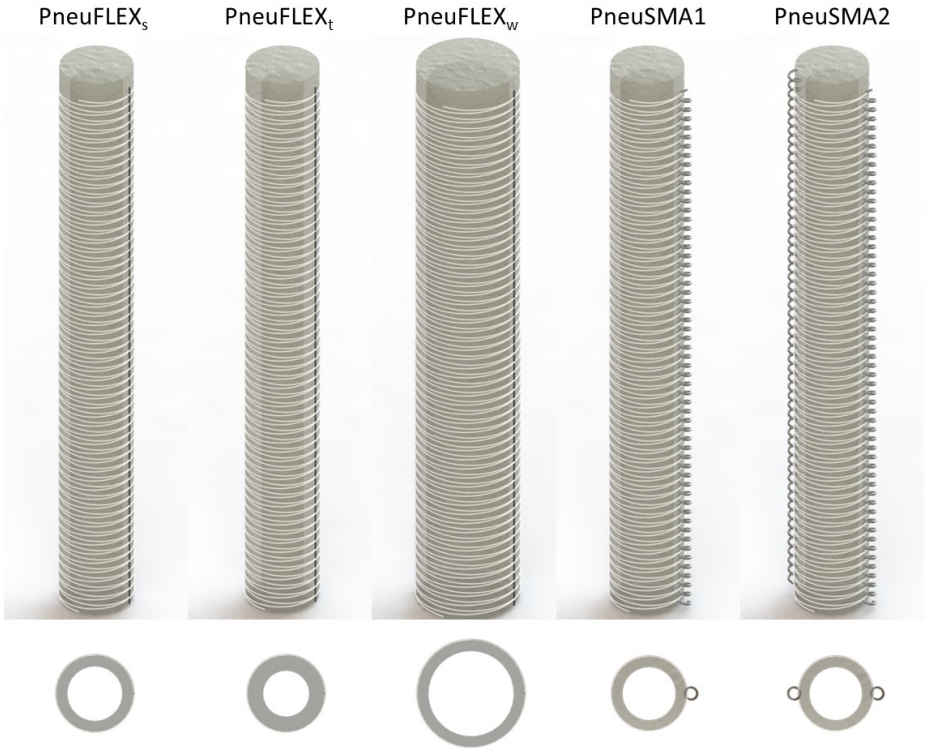

Figure 3.16: PneuSMA and PneuFLEX samples for experimental validation.

3.7.2 Experimental setup

To test the PneuSMA actuators for validation of the analytical model, the supply air pressure and the heating of the nitinol springs must be controllable while the pressure, electrical resistance of the nitinol springs, and the resulting configuration of the actuator are monitored.

The test setup for these experiments is shown in Figure 3.17 where the actuator is clamped in a vice with a supply tube attached to an air compressor. The pressure in the actuator is measured using a pressure transducer and controlled using a pressure regulator between the actuator and the air compressor. The heating of the nitinol spring is controlled via pulse-width modulation input from the Arduino Mega to a voltage regulator. At 100% duty cycle, the voltage regulator supplies a constant current to the nitinol spring, despite subtle changes in the nitinol resistance. Monitoring the voltage drop across the nitinol springs with an amplifier then allows the resistance to be monitored simultaneously while the spring is heating or cooling, provided that at least a small trickle current is flowing through the coils even during cooling. A camera facing the front of the actuator tracks the configuration of the actuator during the tests. The actuator's curvature, length, and bend angle are then extracted from the video footage using basic image processing in MATLAB.

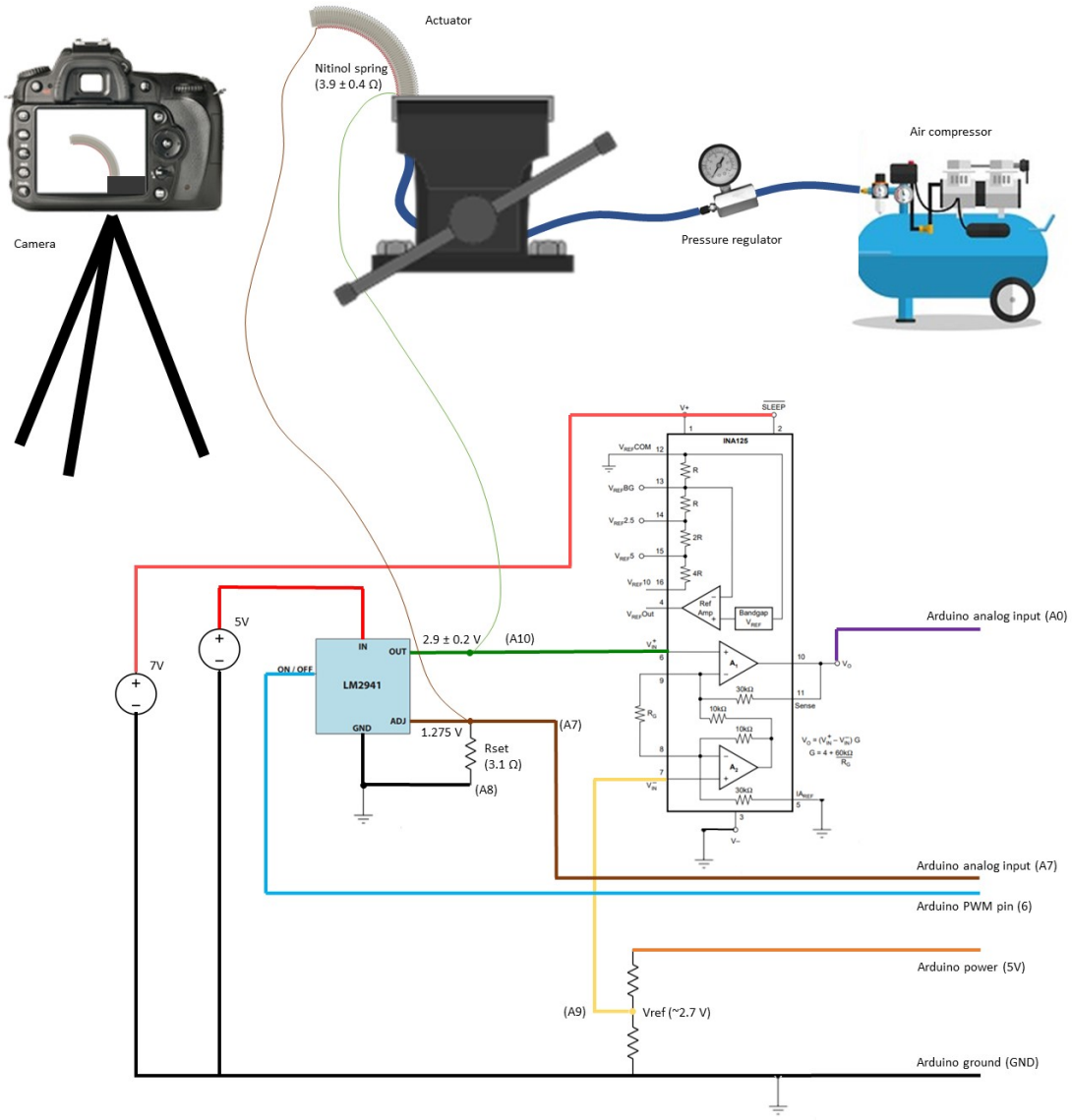

Figure 3.17: Wiring diagram and experimental setup for PneuSMA actuator tests.

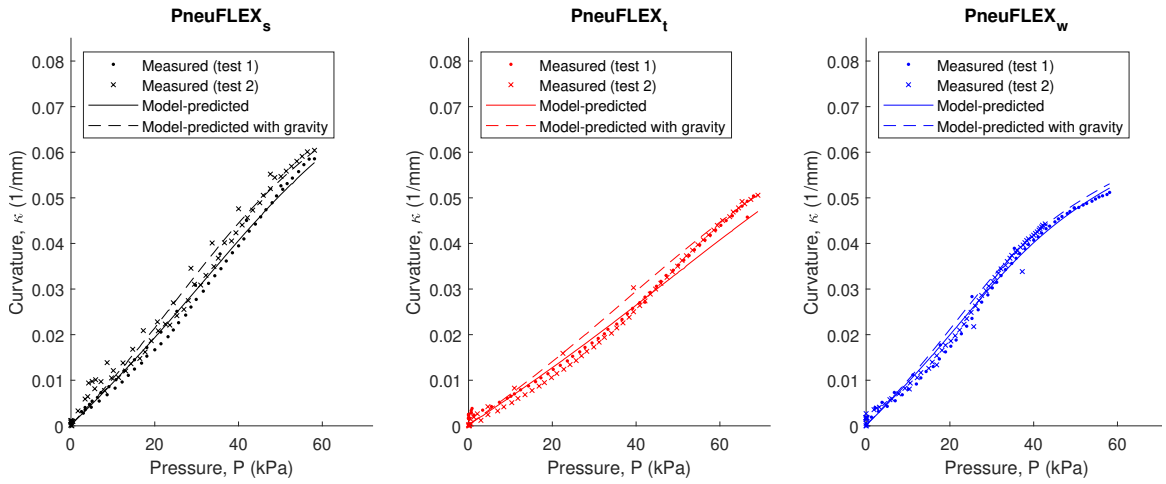

Figure 3.18: Measured curvature versus model-predicted curvature for three different PneuFLEX actuator geometries.

3.7.3 PneuFLEX curvature tests

First, the PneuFLEX actuators (no nitinol springs) were tested to confirm the validity of the analytical model before adding the complexity of the nitinol springs. Each PneuFLEX actuator was clamped in the vice and pressurized to about 60 kPa (8.7 psig), then vented back to zero pressure while the curvature was measured via camera. Tests were conducted twice with each PneuFLEX actuator for repeatability. The measured curvature from each PneuFLEX actuator is compared with the model-predicted curvature in Figure 3.18. No noticeable hysteresis was observed, and the model tracks well with the experimental data.

The effects of gravity were also explored with the PneuFLEX actuators. Incorporating the weight of the actuator in the force and bending moment balance equations

caused a slight increase in the predicted curvature as the actuators were tested in a vertical orientation where their weight would cause increased bending. The model-predicted curvatures with and without the inclusion of gravity differed by a maximum of 8.2% in the standard geometry, 9.7% in the thick-walled geometry, and 4.3% in the wide geometry. The effects of gravity were deemed relatively minor for the light weight of actuator used in this work (< 2.5 g), and the slight difference in predicted curvature with and without gravity lies well within the range of uncertainty based on silicone wall thickness measurement uncertainty. Thus, gravitational effects were excluded in the modeling of the PneuSMA actuators.

3.7.4 PneuSMA constant pressure tests

The two PneuSMA actuators were tested at constant pressure to observe the effects of temperature (and hence electrical resistance) on the actuator curvature. For these tests, the actuators were clamped in the vice, pressurized to a desired setpoint, then thermally cycled by ramping the duty cycle on the voltage regulator up from 0 to 80%, holding at 80% duty cycle for 10-15 seconds, then cooling with 0% duty cycle. The pressure and RMS current inputs for each actuator are shown in Figure 3.19. The resistance in the nitinol springs was measured during the tests and smoothed using polynomial fits to the expreimental data, as shown in Figure 3.20.

The resulting actuator curvatures are plotted against both time and electrical resistance in Figure 3.21. Note that the one-spring PneuSMA actuator ($PneuSMA_1$)

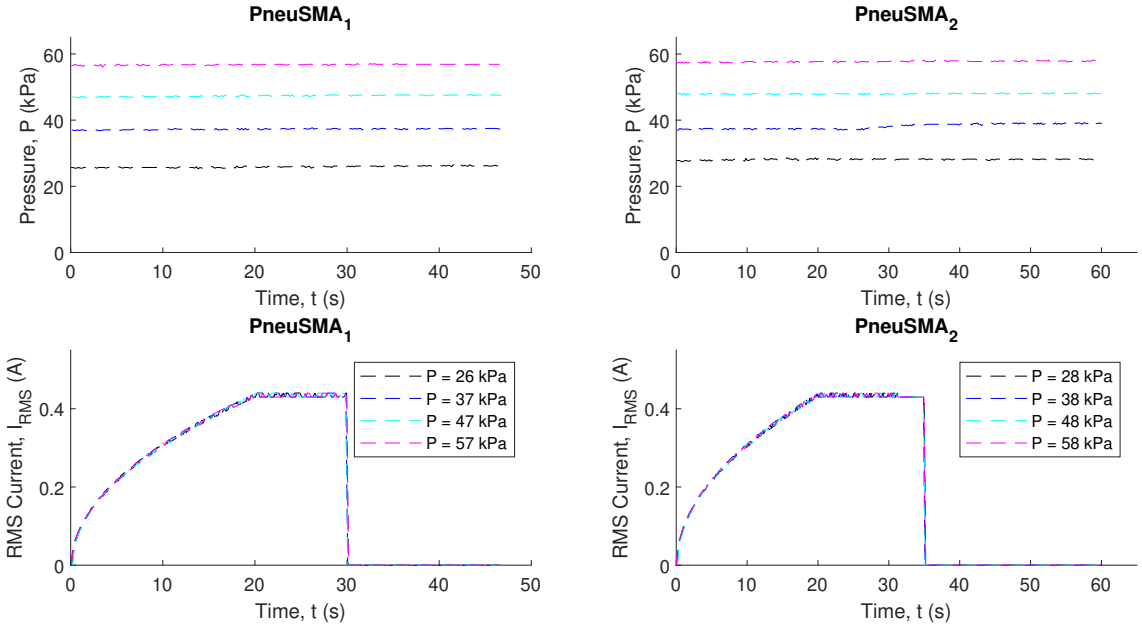

Figure 3.19: Applied pressure and RMS current input during constant pressure PneuSMA tests.

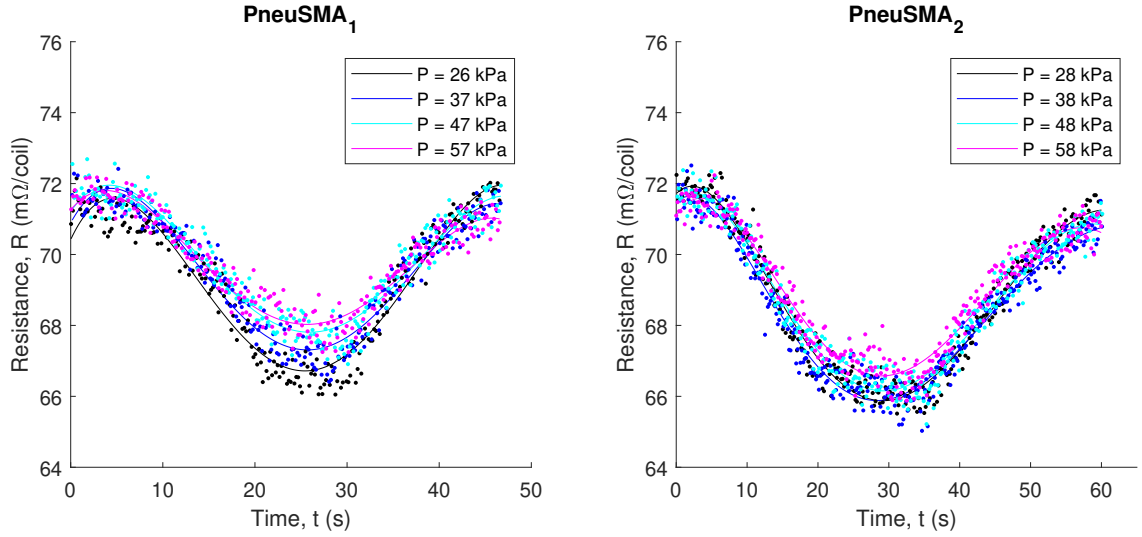

Figure 3.20: Measured electrical resistance in nitinol springs during constant pressure testing of the PneuSMA actuators. Dots represent actual measurements; solid lines are polynomials fit to the measured data.

starts with some curvature before heating begins due the asymmetric spring force upon pressurization to the setpoint. The $PneuSMA_2$ actuator, on the other hand, starts off with zero curvature prior to heating as the opposing springs apply equal forces until one is heated while the other remains at room temperature.

Also note that the actuator does not return to its initial curvature after the heating/cooling cycle as the heating process causes most of the initial residual strain to be recovered. This underlying effect is discussed in Section 3.4.1, but its implications are witnessed in the actuators themselves. In these tests, the model tracks fairly well with the experimental data, capturing the general curvature trends and expected residual strain recovery.

3.7.5 PneuSMA constant heating tests

Constant heating tests were also conducted on the PneuSMA actuators to isolate the effect of pressure on the curvature of the actuators. For these tests, the right-hand nitinol springs were heated at a constant rate until thermal equilibrium was reached, then the pressure was ramped up to about 40-70 kPa (5.8 - 10.2 psig) and ramped back down to zero. Figure 3.22 shows a typical pressure input curve for the constant heating PneuSMA tests. However, at high temperatures, the pressure could not be ramped as high because the vice would begin to interfere with the actuator bending and skew the results. The measured resistances in the nitinol springs during the constant heating tests are shown in Figure 3.23, along with straight lines fit to

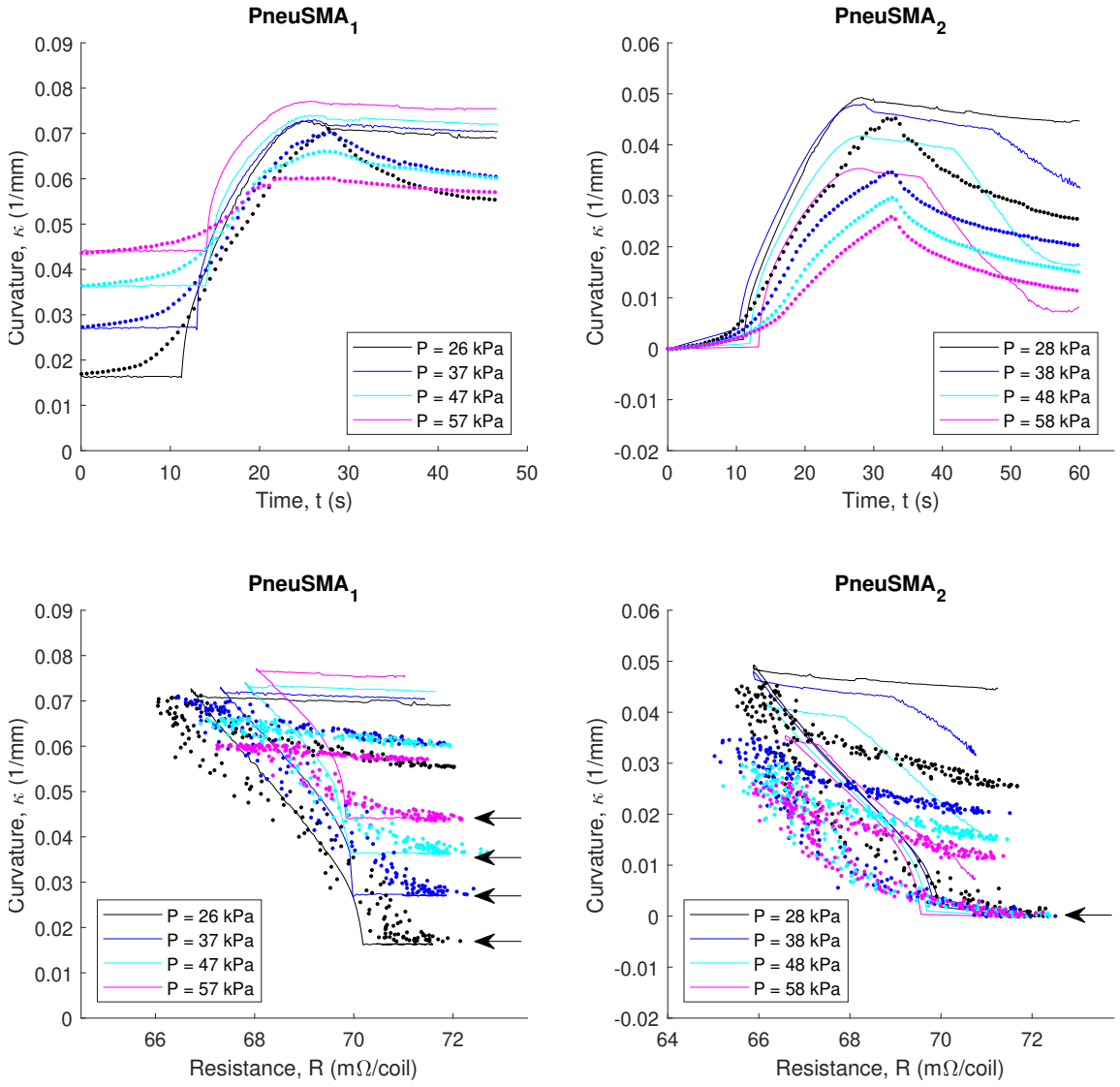

Figure 3.21: Comparison of measured curvatures and model-predicted curvatures from constant pressure testing of PneuSMA actuators. Solid curves represent model prediction; discrete points represent measured curvatures.

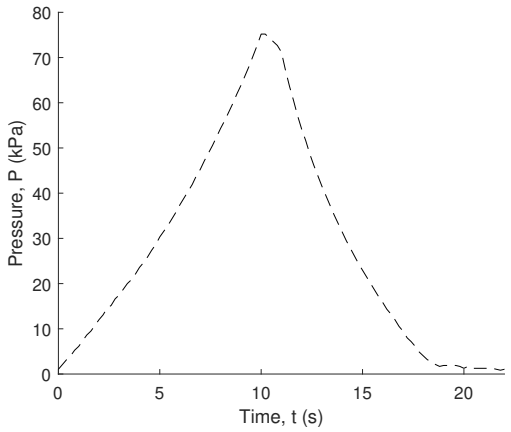

Figure 3.22: Typical pressure input for constant heating PneuSMA tests.

smooth the measurements.

The resulting actuator curvatures as a function of pressure are plotted in Figure 3.24, alongside the model-predicted curvatures. These tests show that the actuator curvature generally decreases as pressure increases. This observation aligns with the expected behavior as bending is primarily caused by contraction of the nitinol springs, and increasing the pressure opposes the nitinol spring contraction, causing a loosening of the bend radius. The only exception to this trend occurs in the low temperature tests with the one-spring PneuSMA actuator where the curvature increases slightly with pressure. This behavior is understandable given the design of the actuator. Since there is no spring on the left-hand side of the one-spring PneuSMA actuator, bending is significantly enhanced by elongation of the silicone on the left-hand side. Increasing pressure promotes further silicone elongation and can thus increase curvature. This

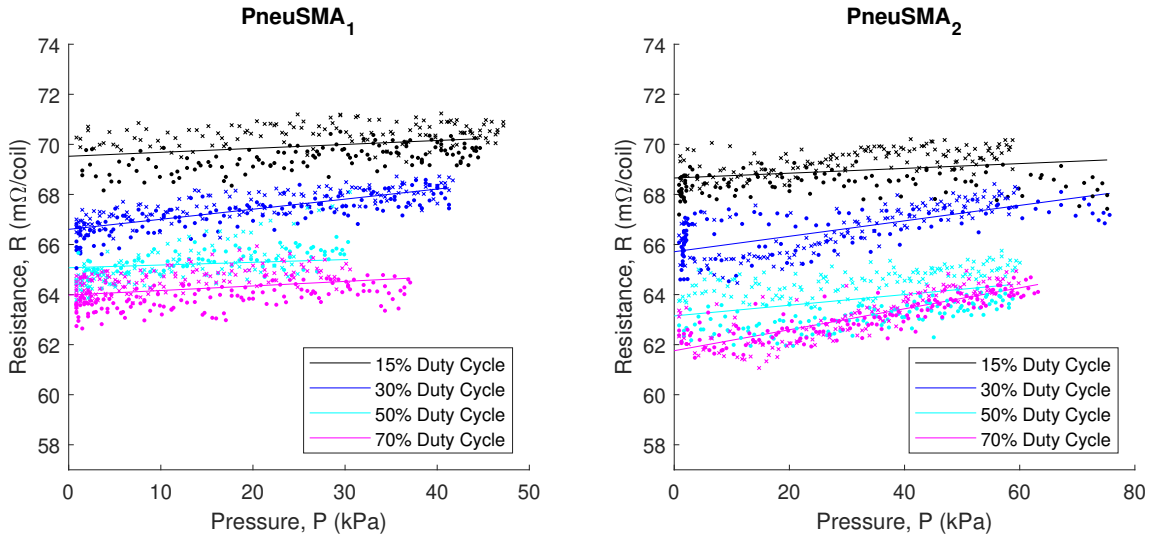

Figure 3.23: Measured electrical resistance in nitinol springs during constant heating testing of the PneuSMA actuators. Arrows indicate the test starting points; dots represent actual measurements; solid lines are fit to smooth the measured data.

behavior is not seen in the high temperature tests with the one-spring PneuSMA actuator because at high temperatures the spring contraction is the dominant cause of bending and minor effects from silicone elongation do not cause a noticible curvature increase with pressure.

Note that there is no noticeable hysteresis in the constant heating tests with pressure cycling. The actuator curvatures trace the same paths during both the pressurization and depressurization processes, and the actuator returns to its original configuration after pressure cycling. A different unloading path would be followed if either (a) the springs were stretched far enough with the applied pressure to cause further detwinning of the martensite, or (b) the temperature was increased at some

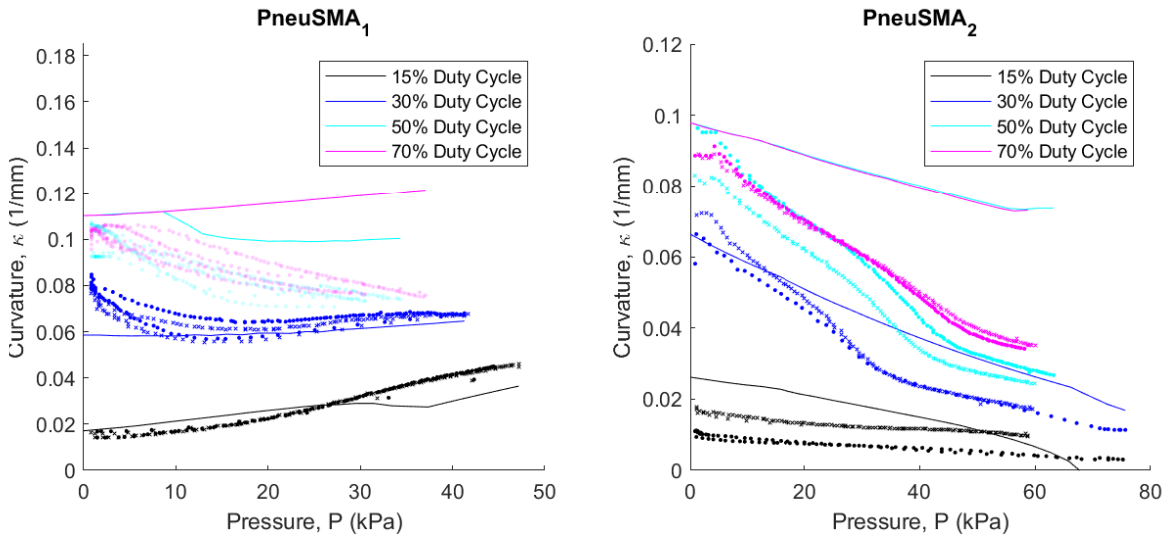

Figure 3.24: Comparison of measured curvatures and model-predicted curvatures from constant heating testing of PneuSMA actuators. Solid curves represent model prediction; discrete points represent measured curvatures.

point to cause recovery of some of the initial residual strain. In the constant heating tests, neither of these effects were realized as the springs never exceeded the initial pre-strain of $\gamma_p = 0.1924$, and the tests were conducted with a constant heating rate which would result in nearly constant temperature.

The analytical model does not track as closely with the experimental data in the constant heating tests compared to the constant pressure tests. As seen in Figure 3.24, a significant deviation is seen especially in the high temperature tests as pressure is increased and the model predicts a much higher curvature than is seen in the experimental measurements. In the one-spring PneuSMA actuator, this discrepancy can be explained by an interference between the actuator tip and the clamp at the

base of the actuator. When the spring on the $PneuSMA_1$ actuator is heated up to the 50 or 70% duty cycle setpoints, the actuator buckles and curls so tightly that it bends more than 270° and bends back on itself, preventing further bending. As the pressure is increased, the tip remains in contact with the base and is not able to exhibit its full curvature potential. Hence, the measured curvatures in the $PneuSMA_1$ actuator at 50 and 70% duty cycles are substantially skewed and should be disregarded. In the two-spring PneuSMA actuator, the opposing spring reduces the curvature enough that the interference does not occur. However, the $PneuSMA_2$ actuator still shows a lower curvature than is predicted by the model, especially in the high temperature tests. In this case, the reduction in curvature is likely due to some incidental heating of the opposing spring. The resistance and temperature in the opposing spring was not measured during the tests as it was assumed to be at room temperature and hence fully martensitic. However, it is highly possible that as the right-hand spring was heated, the temperature of the left-hand spring may have increased slightly due to conductive heat transfer, which would cause a reduction in the experimental curvatures, especially in the high temperature tests.

3.8 Model implications

Several valuable implications can be drawn from the analytical model developed for the PneuSMA actuator in terms of design optimization, workspace estimation, and control implementation.

3.8.1 Workspace comparison

It has been previously stated that the PneuSMA actuator offers improved spatial maneuverability compared to simple fiber-reinforced bending actuators such as the PneuFLEX actuators tested in this work. The analytical model developed for the PneuSMA actuator allows this improvement in the actuator workspace to be quantified and visualized. Figure 3.25 shows the range of curvatures and bend angles achievable with three different types of actuators: (1) a PneuFLEX actuator with standard dimensions, (2) a PneuSMA actuator with two springs arranged opposite one another, and (3) a PneuSMA actuator with one spring along the right side. It can be seen that the PneuSMA actuators are capable of much higher curvatures as well as multi-directional bending in the $PneuSMA_2$ actuator. Note that the curvature and bend angle workspaces for the PneuSMA actuators are represented by shaded regions while the PneuFLEX curvature and bend angle workspaces can be represented with a single curve as a function of pressure. This is because a variety of curvatures and bend angles can be achieved at a single pressure in the PneuSMA actuators by adjusting the SMA spring activation levels, whereas the PneuFLEX actuator curvature is a function of pressure alone.

A trade-off exists between the $PneuSMA_1$ and $PneuSMA_2$ actuator designs. While the two-spring PneuSMA actuator offers multi-directional bending, the one-spring PneuSMA actuator can achieve the tightest curvature, making it ideal for

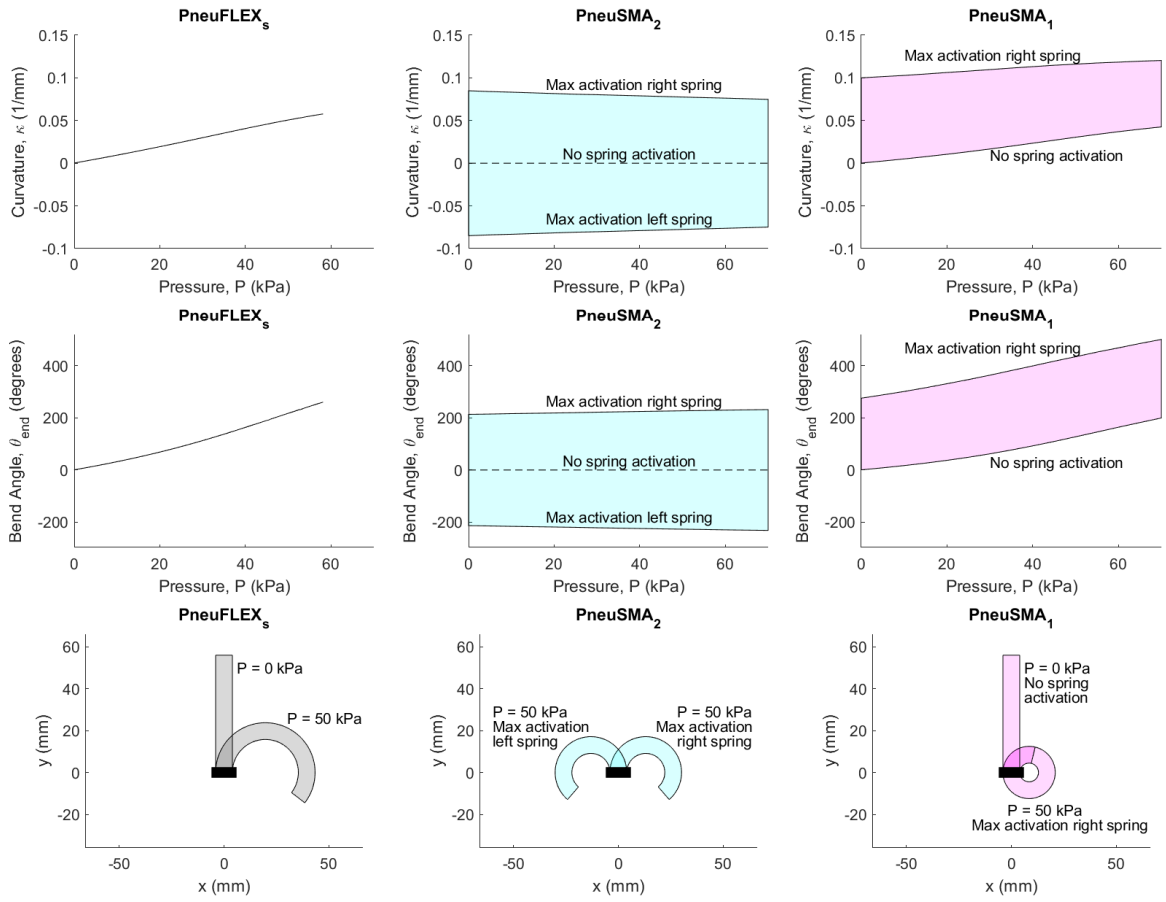

Figure 3.25: Workspace comparison between PneuFLEX and PneuSMA actuators. The bottom row shows the minimum and maximum curvature configurations within a pressure range of 0-60 kPa (0-8.7 psig).

gripping small objects or traversing tight corners in a channel. Still, both PneuSMA actuators outperform the simple fiber-reinforced bending actuator in terms of both curvature and maneuverability.

3.8.2 Design optimization

The analytical PneuSMA model can be used, as demonstrated above, to predict the workspace for a given actuator design. Several design parameters can be tuned to offer different bending capabilities and spatial resolution. For example, three-dimensional bending can be achieved by arranging three nitinol springs in a triad arrangement, or by alternating segments with two opposing springs in the x-y plane then the x-z plane then x-y plane, etc. Selecting different silicone materials, SMA spring alloys, silicone cross-sectional geometry, and SMA spring dimensions all would affect the bend angle and curvature workspace. The model can be used to predict the workspace for any variation of the PneuSMA actuator in order to select an optimal design for a given application.

3.9 Conclusions and future work

In this chapter, the design of a highly-maneuverable hybrid pneumatic/shape-memory alloy (PneuSMA) soft actuator was presented. The design features pre-stretched nitinol springs along the sides of the actuator to control the bending direction and magnitude. A background explanation of the constituent silicone and

nitinol materials was presented, along with experimental characterization studies on their mechanical properties. Extensions were made to the resistance-based nitinol spring model from the previous chapter to account for residual strain due to the formation of detwinned martensite at low temperatures.

An analytical model was also developed to predict the configuration of the PneuSMA actuator based on pressure and nitinol electrical resistance inputs. The analytical model relies on quasi-static assumptions and is based on a force and moment balance on the end of the actuator, incorporating the buckling effects and nonlinear stiffness of the silicone rubber as well as the temperature-depended properties of the nitinol springs. Although the model was developed for standard PneuSMA actuators with round cross section, it can easily be adapted for application to different actuator cross sections, different dimensions, different spring arrangements, or even for simple fiber-reinforced bending (PneuFLEX) actuators with no SMA springs involved.

Experimental tests on several variations of the PneuSMA and PneuFLEX actuators were conducted to compare the measured curvatures with the model predictions. The model tracked extremely well with the experimental curvatures from from the PneuFLEX actuators tested over a range of pressures from 0 to 60 kPa (0 to 8.7 psig). The PneuSMA actuators were tested under constant pressure conditions with thermal cycling, then under constant heating condition with pressure cycling. The model provided a reasonably good fit to the experimental curvatures from the constant pres-

sure tests, capturing both the initial curvature and the effects of strain recovery in the nitinol springs after thermal cycling. The experimental curvatures from the constant heating tests show some deviation from the analytical model, especially at high temperatures. However, these discrepancies can be explained by interference between the actuator tip and base in the one-spring actuator, and by slight incidental heating of the opposing spring in the two-spring actuator. Overall, the quasi-static analytical model developed for the PneuSMA actuator captures the general configuration trends under both the constant pressure and constant heating conditions.

With this incorporation of a position control algorithm with both resistance position feedback, the PneuSMA analytical model could be used to drive a multi-segmented actuator to a desired configuration, or even through a tortuous channel, which is especially desirable for medical applications. The next steps for making the PneuSMA actuator suitable for medical applications would include:

- Implement a position control algorithm based on electrical resistance feedback from nitinol springs.
- Modify the fabrication process slightly in order to place the nitinol springs on the inside walls of the actuator so that heated springs do not come into contact with bodily tissue during medical procedures.
- Incorporate a venting system to speed the cooling of the nitinol springs placed on the inside walls of the actuator.

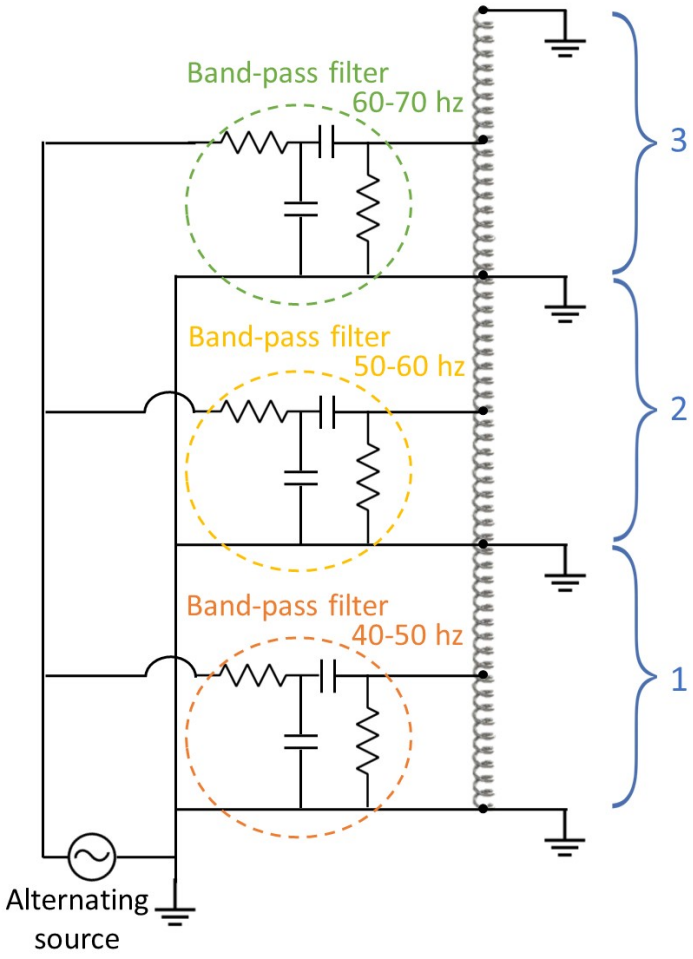

Figure 3.26: Demonstration of possible circuit design for independent current control in three segments of a nitinol spring using a single voltage source.

- Develop a circuit design that is capable of measuring resistance and supplying heat to various segments along nitinol springs with minimal wire connections. This may be achieved by tuning the frequency of an alternating current in the nitinol spring with band-pass filters that only allow the current to pass through certain segments as shown in Figure 3.26.

With these advancements to the design and control aspects, the PneuSMA actuator could offer significant improvements compared to currently used tip-steerable catheter devices in terms of both safety and maneuverability.

BIBLIOGRAPHY

[1] Rohan Abeyaratne and James K. Knowles. On the driving traction acting on a surface of strain discontinuity in a continuum. *Journal of the Mechanics and Physics of Solids*, 38(3):345–360, January 1990.

[2] Gunjan Agarwal, Nicolas Besuchet, Basile Audergon, and Jamie Paik. Stretchable Materials for Robust Soft Actuators towards Assistive Wearable Devices. *Scientific Reports*, 6(1):34224, September 2016. Number: 1 Publisher: Nature Publishing Group.

[3] G. Airoldi, D. Lodi, and M. Pozzi. The Electric Resistance of Shape Memory Alloys in the Pseudoelastic Regime. *Journal de Physique IV Proceedings*, 07(C5):C5–507–C5–512, 1997. Publisher: EDP Sciences.

[4] Emily A. Allen and John P. Swensen. Directional Stiffness Control Through Geometric Patterning and Localized Heating of Field's Metal Lattice Embedded in Silicone. *Actuators*, 7(4):80, December 2018.

[5] Emily A. Allen and John P. Swensen. Versatile Layering Approach to Pneumatic Soft Actuator Manufacturing. In *ASME 2019 Conference on Smart Materials, Adaptive Structures and Intelligent Systems (SMASIS)*. American Society of Mechanical Engineers Digital Collection, December 2019.

[6] Emily A. Allen and John P. Swensen. Design of a Highly-Maneuverable Pneumatic Soft Actuator Driven by Intrinsic SMA Coils (PneuSMA Actuator). In *2020 IEEE/RSJ International Conference on Intelligent Robots and Systems (IROS)*, pages 8667–8672, Las Vegas, NV, USA, October 2020. IEEE.

[7] Sung-Min An, Junghyun Ryu, Maenghyo Cho, and Kyu-Jin Cho. Engineering design framework for a shape memory alloy coil spring actuator using a static two-state model. *Smart Materials and Structures*, 21(5):055009, May 2012.

[8] Iain A. Anderson, Todd A. Gisby, Thomas G. McKay, Benjamin M. O'Brien, and Emilio P. Calius. Multi-functional dielectric elastomer artificial muscles for soft and smart machines. *Journal of Applied Physics*, 112(4):041101, 2012. _eprint: https://doi.org/10.1063/1.4740023.

[9] F. Auricchio and E. Sacco. A one-dimensional model for superelastic shape-memory alloys with different elastic properties between austenite and martensite. *International Journal of Non-Linear Mechanics*, 32(6):1101–1114, November 1997.

[10] Andrea Bajo and Nabil Simaan. Kinematics-Based Detection and Localization of Contacts Along Multisegment Continuum Robots. *IEEE Transactions on Robotics*, 28(2):291–302, April 2012.

[11] J. M. Ball and R. D. James. Fine Phase Mixtures as Minimizers of Energy. In

Stuart S. Antman, Haïm Brezis, Bernard D. Coleman, Martin Feinberg, John A. Nohel, and William P. Ziemer, editors, *Analysis and Continuum Mechanics: A Collection of Papers Dedicated to J. Serrin on His Sixtieth Birthday*, pages 647–686. Springer, Berlin, Heidelberg, 1989.

[12] C. D. J. Barras and K. A. Myers. Nitinol – Its Use in Vascular Surgery and Other Applications. *European Journal of Vascular and Endovascular Surgery*, 19(6):564–569, June 2000.

[13] G. R. Barsch and J. A. Krumhansl. Nonlinear and nonlocal continuum model of transformation precursors in martensites. *Metallurgical Transactions A*, 19(4):761–775, April 1988.

[14] Francis Bechet, Kenji Ogawa, Emre Sariyildiz, and Kouhei Ohnishi. Electrohydraulic Transmission System for Minimally Invasive Robotics. *IEEE Transactions on Industrial Electronics*, 62(12):7643–7654, December 2015.

[15] Christoph Bechtold, Rodrigo Lima de Miranda, Christoph Chluba, and Eckhard Quandt. Fabrication of self-expandable NiTi thin film devices with microelectrode array for bioelectric sensing, stimulation and ablation. *Biomedical Microdevices*, 18(6):106, November 2016.

[16] Julius Bernth, Alberto Arezzo, and Hongbin Liu. A Novel Robotic Meshworm

With Segment-Bending Anchoring for Colonoscopy. *IEEE Robotics and Automation Letters*, 2:1–1, July 2017.

[17] Joshua Bishop-Moser and Sridhar Kota. Design and Modeling of Generalized Fiber-Reinforced Pneumatic Soft Actuators. *IEEE Transactions on Robotics*, 31(3):536–545, June 2015.

[18] Loïc Blanc, Alain Delchambre, and Pierre Lambert. Flexible Medical Devices: Review of Controllable Stiffness Solutions. *Actuators*, 6(3):23, September 2017. Number: 3 Publisher: Multidisciplinary Digital Publishing Institute.

[19] P. Blanc and C. Lexcellent. Micromechanical modelling of a CuAlNi shape memory alloy behaviour. *Materials Science and Engineering: A*, 378(1):465–469, July 2004.

[20] J. G. Boyd and D. C. Lagoudas. A thermodynamical constitutive model for shape memory materials. Part I. The monolithic shape memory alloy. *International Journal of Plasticity*, 12(6):805–842, January 1996.

[21] Pinar Boyraz, Gundula Runge, and Annika Raatz. An Overview of Novel Actuators for Soft Robotics. *Actuators*, 7:48, August 2018.

[22] L. C. Brinson and M. S. Huang. Simplifications and Comparisons of Shape Memory Alloy Constitutive Models. *Journal of Intelligent Material Systems and Structures*, 7(1):108–114, January 1996.

[23] L.C. Brinson. One-Dimensional Constitutive Behavior of Shape Memory Alloys: Thermomechanical Derivation with Non-Constant Material Functions and Redefined Martensite Internal Variable. *Journal of Intelligent Material Systems and Structures*, 4(2):229–242, April 1993.

[24] G. F. Buess, A. Arezzo, and M. O. Schurr. Techniques for endoluminal intestinal tract surgery. *Minimally Invasive Therapy & Allied Technologies*, 7(1):31–36, January 1998. Publisher: Taylor & Francis _eprint: https://doi.org/10.3109/13645709809152840.

[25] Vladimir Buljak and Gianluca Ranzi. Chapter 9 - Shape memory alloys. In Vladimir Buljak and Gianluca Ranzi, editors, *Constitutive Modeling of Engineering Materials*, pages 293–313. Academic Press, January 2021.

[26] Le Chen, Ying Feng, Rui Li, Xinkai Chen, and Hui Jiang. Jiles-Atherton Based Hysteresis Identification of Shape Memory Alloy-Actuating Compliant Mechanism via Modified Particle Swarm Optimization Algorithm. *Complexity*, 2019:e7465461, February 2019. Publisher: Hindawi.

[27] Ching-Ping Chou and B. Hannaford. Measurement and modeling of McKibben pneumatic artificial muscles. *IEEE Transactions on Robotics and Automation*, 12(1):90–102, February 1996.

[28] Jong-Ha Chung, Jin-Seok Heo, and Jung-Ju Lee. Implementation strategy

for the dual transformation region in the Brinson SMA constitutive model. *Smart Materials and Structures*, 16(1):N1–N5, November 2006. Publisher: IOP Publishing.

[29] Matteo Cianchetti. Fundamentals on the Use of Shape Memory Alloys in Soft Robotics. In Maki K. Habib and J. Paulo Davim, editors, *Interdisciplinary Mechatronics*, pages 227–254. John Wiley & Sons, Inc., Hoboken, NJ USA, May 2013.

[30] Matteo Cianchetti, Marcello Calisti, Laura Margheri, Michael Kuba, and Cecilia Laschi. Bioinspired locomotion and grasping in water: The soft eight-arm OCTOPUS robot. *Bioinspiration &amp Biomimetics*, 10, March 2015.

[31] Matteo Cianchetti, Maurizio Follador, Barbara Mazzolai, Paolo Dario, and Cecilia Laschi. Design and development of a soft robotic octopus arm exploiting embodied intelligence. In *2012 IEEE International Conference on Robotics and Automation*, pages 5271–5276. IEEE, 2012.

[32] Matteo Cianchetti, Cecilia Laschi, Arianna Menciassi, and Paolo Dario. Biomedical applications of soft robotics. *Nature Reviews Materials*, 3(6):143–153, June 2018. Number: 6 Publisher: Nature Publishing Group.

[33] Matteo Cianchetti, Virgilio Mattoli, Barbara Mazzolai, Cecilia Laschi, and Paolo Dario. A new design methodology of electrostrictive actuators for bio-

inspired robotics. *Sensors and Actuators B: Chemical*, 142:288–297, October 2009.

[34] Matteo Cianchetti, Tommaso Ranzani, Giada Gerboni, Thrishantha Nanayakkara, Kaspar Althoefer, and Prokar Dasgupta. Soft Robotics Technologies to Address Shortcomings in Today's Minimally Invasive Surgery: The STIFF-FLOP Approach. *Soft Robotics. (SoRo)*, 1:122–131, June 2014.

[35] Cheikh Cisse, Wael Zaki, and Tarak Ben Zineb. A review of constitutive models and modeling techniques for shape memory alloys. *International Journal of Plasticity*, 76:244–284, January 2016.

[36] Fionnuala Connolly, Panagiotis Polygerinos, Conor J. Walsh, and Katia Bertoldi. Mechanical programming of soft actuators by varying fiber angle. *Soft Robotics*, 2(1):26–32, 2015.

[37] Fionnuala Connolly, Conor J. Walsh, and Katia Bertoldi. Automatic design of fiber-reinforced soft actuators for trajectory matching. *Proceedings of the National Academy of Sciences*, 114(1):51–56, January 2017. Publisher: Proceedings of the National Academy of Sciences.

[38] Stephen Coyle, Carmel Majidi, Philip LeDuc, and K. Jimmy Hsia. Bio-inspired soft robotics: Material selection, actuation, and design. *Extreme Mechanics Letters*, 22:51–59, July 2018.

[39] Di Cui, Gangbing Song, and Hongnan Li. Modeling of the electrical resistance of shape memory alloy wires. *Smart Materials and Structures*, 19(5):055019, April 2010. Publisher: IOP Publishing.

[40] Kathryn A. Daltorio, Alexander S. Boxerbaum, Andrew D. Horchler, Kendrick M. Shaw, Hillel J. Chiel, and Roger D. Quinn. Efficient worm-like locomotion: slip and control of soft-bodied peristaltic robots. *Bioinspiration & Biomimetics*, 8(3):035003, August 2013. Publisher: IOP Publishing.

[41] R. J. Damiano, H. A. Tabaie, M. J. Mack, J. R. Edgerton, C. Mullangi, W. P. Graper, and S. M. Prasad. Initial prospective multicenter clinical trial of robotically-assisted coronary artery bypass grafting. *The Annals of Thoracic Surgery*, 72(4):1263–1268; discussion 1268–1269, October 2001.

[42] Aline De Greef, Pierre Lambert, and Alain Delchambre. Towards flexible medical instruments: Review of flexible fluidic actuators. *Precision Engineering*, 33(4):311–321, October 2009.

[43] Mohammad Dehghani and S.A.A. Moosavian. Dynamics modeling of planar continuum robots by finite circular elements for motion control. In *2015 AI Robotics (IRANOPEN)*, pages 1–6, April 2015.

[44] Raphael Deimel and O. Brock. A novel type of compliant and underactuated robotic hand for dexterous grasping. *Int. J. Robotics Res.*, 2016.

[45] Raphael Deimel and Oliver Brock. A compliant hand based on a novel pneumatic actuator. In *2013 IEEE International Conference on Robotics and Automation*, pages 2047–2053, May 2013. ISSN: 1050-4729.

[46] T. Devashena and K. Dhanalakshmi. Electro-Thermo-Mechano-Magneto Characteristics of Shape Memory Spring Actuator/Sensor in Assistive Devices. In Milan Tuba, Shyam Akashe, and Amit Joshi, editors, *ICT Systems and Sustainability*, Advances in Intelligent Systems and Computing, pages 379–386, Singapore, 2020. Springer.

[47] R. P. Dhote, R. N. V. Melnik, and J. Zu. Dynamic multi-axial behavior of shape memory alloy nanowires with coupled thermo-mechanical phase-field models. *Meccanica*, 7(49):1561–1575, 2014.

[48] Yu Dong, Zhang Boming, and Liang Jun. A changeable aerofoil actuated by shape memory alloy springs. *Materials Science and Engineering: A*, 485(1-2):243–250, June 2008.

[49] Dylan Drotman, Michael Ishida, Saurabh Jadhav, and Michael T. Tolley. Application-Driven Design of Soft, 3-D Printed, Pneumatic Actuators With Bellows. *IEEE/ASME Transactions on Mechatronics*, 24(1):78–87, February 2019.

[50] G. R. Dunlop and Pb Christchurch. Feedback Control of a Nitinol Wire Actuator.

[51] F. Falk. Model free energy, mechanics, and thermodynamics of shape memory alloys. *Acta Metallurgica*, 28(12):1773–1780, December 1980.

[52] F. Falk. Ginzburg-Landau theory of static domain walls in shape-memory alloys. *Zeitschrift für Physik B Condensed Matter*, 51(2):177–185, June 1983.

[53] American Society for Testing and Materials. Standard Test Methods for Rubber Properties in Compression. *ASTM Standard D575-91*, 2018.

[54] American Society for Testing and Materials. Standard Test Methods for Vulcanized Rubber and Thermoplastic Elastomers—Tension. *ASTM Standard D412-16*, 2021.

[55] J. Fraś, J. Czarnowski, M. Maciaś, J. Główka, M. Cianchetti, and A. Menciassi. New STIFF-FLOP module construction idea for improved actuation and sensing. In *2015 IEEE International Conference on Robotics and Automation (ICRA)*, pages 2901–2906, May 2015. ISSN: 1050-4729.

[56] Stephen J Furst, John H Crews, and Stefan Seelecke. Stress, strain, and resistance behavior of two opposing shape memory alloy actuator wires for resistance-based self-sensing applications. *Journal of Intelligent Material Sys-*

tems and Structures, 24(16):1951–1968, November 2013. Publisher: SAGE Publications Ltd STM.

[57] Stephen J Furst and Stefan Seelecke. Modeling and experimental characterization of the stress, strain, and resistance of shape memory alloy actuator wires with controlled power input. *Journal of Intelligent Material Systems and Structures*, 23(11):1233–1247, July 2012. Publisher: SAGE Publications Ltd STM.

[58] Ken Gall, T. Jesse Lim, David L McDowell, Huseyin Sehitoglu, and Yuriy I Chumlyakov. The role of intergranular constraint on the stress-induced martensitic transformation in textured polycrystalline NiTi. *International Journal of Plasticity*, 16(10):1189–1214, January 2000.

[59] Kevin C. Galloway, Panagiotis Polygerinos, Conor J. Walsh, and Robert J. Wood. Mechanically programmable bend radius for fiber-reinforced soft actuators. In *2013 16th International Conference on Advanced Robotics (ICAR)*, pages 1–6, November 2013.

[60] Joey Z. Ge, Ariel A. Calderón, Longlong Chang, and Néstor O. Pérez-Arancibia. An earthworm-inspired friction-controlled soft robot capable of bidirectional locomotion. *Bioinspiration & Biomimetics*, 14(3):036004, February 2019. Publisher: IOP Publishing.

[61] Giada Gerboni, Tommaso Ranzani, Alessandro Diodato, Gastone Ciuti, Matteo Cianchetti, and Arianna Menciassi. Modular soft mechatronic manipulator for minimally invasive surgery (MIS): overall architecture and development of a fully integrated soft module. *Meccanica*, 50(11):2865–2878, November 2015.

[62] M. Wildan Gifari, Hamid Naghibi, Stefano Stramigioli, and Momen Abayazid. A review on recent advances in soft surgical robots for endoscopic applications. *The International Journal of Medical Robotics and Computer Assisted Surgery*, 15(5):e2010, 2019. _eprint: https://onlinelibrary.wiley.com/doi/pdf/10.1002/rcs.2010.

[63] Yannik Goergen, Romol Chadda, Rouven Britz, Dominik Scholtes, Nataliya Koev, Paul Motzki, Roland Werthschützky, Mario Kupnik, and Stefan Seelecke. Shape Memory Alloys in Continuum and Soft Robotic Applications. In *ASME 2019 Conference on Smart Materials, Adaptive Structures and Intelligent Systems*, page V001T04A014, Louisville, Kentucky, USA, September 2019. American Society of Mechanical Engineers.

[64] Santhan Gonthina, Apoorva Kapadia, Isuru Godage, and Ian Walker. Modeling Variable Curvature Parallel Continuum Robots Using Euler Curves. In *2019 International Conference on Robotics and Automation (ICRA)*, pages 1679–1685, May 2019.

[65] Benjamin Gorissen, Michaël De Volder, Aline De Greef, and Dominiek Reynaerts. Theoretical and experimental analysis of pneumatic balloon microactuators. *Sensors and Actuators A: Physical*, 168(1):58–65, July 2011.

[66] Stefan Groth, Douglas Rex, Thomas Rösch, and Nicolas Hoepffner. High Cecal Intubation Rates With a New Computer-Assisted Colonoscope: A Feasibility Study. *The American journal of gastroenterology*, 106:1075–80, March 2011.

[67] Yaguang Guo, Liwu Liu, Yanju Liu, and Jinsong Leng. Review of Dielectric Elastomer Actuators and Their Applications in Soft Robots. *Advanced Intelligent Systems*, 3(10):2000282, 2021. _eprint: https://onlinelibrary.wiley.com/doi/pdf/10.1002/aisy.202000282.

[68] Ujjaval Gupta, Lei Qin, Yuzhe Wang, Hareesh Godaba, and Jian Zhu. Soft robots based on dielectric elastomer actuators: a review. *Smart Materials and Structures*, 28(10):103002, September 2019. Publisher: IOP Publishing.

[69] Austin Gurley, Tyler Ross Lambert, David Beale, and Royall Broughton. Robust Self-Sensing in NiTi Actuators Using a Dual Measurement Technique. In *Volume 2: Modeling, Simulation and Control; Bio-Inspired Smart Materials and Systems; Energy Harvesting*, page V002T03A022, Stowe, Vermont, USA, September 2016. American Society of Mechanical Engineers.

[70] D J Hartl and D C Lagoudas. Aerospace applications of shape memory al-

loys. *Proceedings of the Institution of Mechanical Engineers, Part G: Journal of Aerospace Engineering*, 221(4):535–552, April 2007. Publisher: IMECHE.

[71] Elliot W. Hawkes, Carmel Majidi, and Michael T. Tolley. Hard questions for soft robotics. *Science Robotics*, 6(53):eabg6049, 2021.

[72] Weiping Hu, Rahim Mutlu, Weihua Li, and Gursel Alici. A Structural Optimisation Method for a Soft Pneumatic Actuator. *Robotics*, 7(2):24, June 2018. Number: 2 Publisher: Multidisciplinary Digital Publishing Institute.

[73] Miinshiou Huang, Xiujie Gao, and L. Catherine Brinson. A multivariant micromechanical model for SMAs Part 2. Polycrystal model. *International Journal of Plasticity*, 16(10):1371–1390, January 2000.

[74] Xiaonan Huang, Kitty Kumar, Mohammad K. Jawed, Amir Mohammadi Nasab, Zisheng Ye, Wanliang Shan, and Carmel Majidi. Highly Dynamic Shape Memory Alloy Actuator for Fast Moving Soft Robots. *Advanced Materials Technologies*, 4(4):1800540, 2019. _eprint: https://onlinelibrary.wiley.com/doi/pdf/10.1002/admt.201800540.

[75] Xinjia Huang, Jiang Zou, and Guoying Gu. Kinematic Modeling and Control of Variable Curvature Soft Continuum Robots. *IEEE/ASME Transactions on Mechatronics*, 26(6):3175–3185, December 2021.

[76] Fumiya Iida and Cecilia Laschi. Soft Robotics: Challenges and Perspectives. *Proceedings Of The 2Nd European Future Technologies Conference And Exhibition 2011 (Fet 11)*, 7:99–102, 2011. Publisher: Elsevier Science, Reg Sales Off, Customer Support Dept, 655 Ave Of The Americas, New York, Ny 10010 Usa.

[77] K. Ikuta. Micro/miniature shape memory alloy actuator. In *, IEEE International Conference on Robotics and Automation Proceedings*, pages 2156–2161 vol.3, May 1990.

[78] K. Ikuta, H. Ichikawa, K. Suzuki, and T. Yamamoto. Micro hydrodynamic actuated multiple segments catheter for safety minimally invasive therapy. In *2003 IEEE International Conference on Robotics and Automation (Cat. No.03CH37422)*, volume 2, pages 2640–2645 vol.2, September 2003. ISSN: 1050-4729.

[79] K. Ikuta, M. Tsukamoto, and S. Hirose. Shape memory alloy servo actuator system with electric resistance feedback and application for active endoscope. In *1988 IEEE International Conference on Robotics and Automation Proceedings*, pages 427–430 vol.1, April 1988.

[80] Hu Jin, Erbao Dong, Min Xu, Chunshan Liu, Gursel Alici, and Yang Jie. Soft and smart modular structures actuated by shape memory alloy (SMA) wires

as tentacles of soft robots. *Smart Materials and Structures*, 25(8):085026, July 2016. Publisher: IOP Publishing.

[81] Y. M. Jin, A. Artemev, and A. G. Khachaturyan. Three-dimensional phase field model of low-symmetry martensitic transformation in polycrystal: simulation of 2 martensite in AuCd alloys. *Acta Materialia*, 49(12):2309–2320, July 2001.

[82] Manivannan Sivaperuman Kalairaj, Bok Seng Yeow, Chwee Ming Lim, and Hongliang Ren. Needle-Size Bending Actuators Based on Controlled Nitinol Curvatures and Elastic Structures. *Journal of Mechanisms and Robotics*, 12(3), February 2020.

[83] Tom Kalisky, Yueqi Wang, Benjamin Shih, Dylan Drotman, Saurabh Jadhav, Eliah Aronoff-Spencer, and Michael Tolley. Differential pressure control of 3d printed soft fluidic actuators. In *2017 IEEE/RSJ International Conference on Intelligent Robots and Systems (IROS)*, pages 6207–6213, 09 2017.

[84] S. Kim, E. Hawkes, K. Choy, M. Joldaz, J. Foleyz, and R. Wood. Micro artificial muscle fiber using NiTi spring for soft robotics. In *2009 IEEE/RSJ International Conference on Intelligent Robots and Systems*, pages 2228–2234, October 2009. ISSN: 2153-0866.

[85] Sangbae Kim, Cecilia Laschi, and Barry Trimmer. Soft robotics: a bioinspired evolution in robotics. *Trends in Biotechnology*, 31(5):287–294, May 2013.

[86] Yeongjin Kim, Shing Shin Cheng, Mahamadou Diakite, Rao P. Gullapalli, J. Marc Simard, and Jaydev P. Desai. Toward the Development of a Flexible Mesoscale MRI-compatible Neurosurgical Continuum Robot. *IEEE transactions on robotics: a publication of the IEEE Robotics and Automation Society*, 33(6):1386–1397, December 2017.

[87] G.K. Klute, J.M. Czerniecki, and B. Hannaford. McKibben artificial muscles: pneumatic actuators with biomechanical intelligence. In *1999 IEEE/ASME International Conference on Advanced Intelligent Mechatronics (Cat. No.99TH8399)*, pages 221–226, September 1999.

[88] J. Koh and K. Cho. Omegabot : Biomimetic inchworm robot using SMA coil actuator and smart composite microstructures (SCM). In *2009 IEEE International Conference on Robotics and Biomimetics (ROBIO)*, pages 1154–1159, December 2009. ISSN: null.

[89] Cecilia Laschi, Matteo Cianchetti, Barbara Mazzolai, Laura Margheri, Maurizio Follador, and Paolo Dario. Soft Robot Arm Inspired by the Octopus. *Advanced Robotics*, 26(7):709–727, 2012. Publisher: Taylor & Francis _eprint: https://doi.org/10.1163/156855312X626343.

[90] Cecilia Laschi, Barbara Mazzolai, and Matteo Cianchetti. Soft robotics: Technologies and systems pushing the boundaries of robot abilities.

Science Robotics, 1(1), 2016. Publisher: Science Robotics _eprint: https://robotics.sciencemag.org/content/1/1/eaah3690.full.pdf.

[91] Ji-Hyeong Lee, Yoon Seop Chung, and Hugo Rodrigue. Long Shape Memory Alloy Tendon-based Soft Robotic Actuators and Implementation as a Soft Gripper. *Scientific Reports*, 9(1):11251, August 2019. Number: 1 Publisher: Nature Publishing Group.

[92] Sang-Hak Lee and Sang-Woo Kim. Improved position control of shape memory alloy actuator using the self-sensing model. *Sensors and Actuators A: Physical*, 297:111529, October 2019.

[93] Constantina Lekakou, Yahya Elsayed, Tao Geng, and Chakravarthini M. Saaj. Skins and Sleeves for Soft Robotics: Inspiration from Nature and Architecture. *Advanced Engineering Materials*, 17(8):1180–1188, 2015. _eprint: https://onlinelibrary.wiley.com/doi/pdf/10.1002/adem.201400406.

[94] Valery I. Levitas and Dean L. Preston. Three-dimensional Landau theory for multivariant stress-induced martensitic phase transformations. I. Austenite$\ensuremath{\leftrightarrow}$martensite. *Physical Review B*, 66(13):134206, October 2002. Publisher: American Physical Society.

[95] Valery I. Levitas and Dean L. Preston. Three-dimensional Landau theory for multivariant stress-induced martensitic phase transformations. II. Multi-

variant phase transformations and stress space analysis. *Physical Review B*, 66(13):134207, October 2002. Publisher: American Physical Society.

[96] Valery I. Levitas, Dean L. Preston, and Dong-Wook Lee. Three-dimensional Landau theory for multivariant stress-induced martensitic phase transformations. III. Alternative potentials, critical nuclei, kink solutions, and dislocation theory. *Physical Review B*, 68(13):134201, October 2003. Publisher: American Physical Society.

[97] Yunquan Li, Yonghua Chen, and Yingtian Li. Pre-Charged Pneumatic Soft Gripper With Closed-Loop Control. *IEEE Robotics and Automation Letters*, 4(2):1402–1408, April 2019.

[98] Yunquan Li, Yonghua Chen, Tao Ren, Yingtian Li, and Shiu hong Choi. Precharged Pneumatic Soft Actuators and Their Applications to Untethered Soft Robots. *Soft Robotics*, 5(5):567–575, October 2018. Publisher: Mary Ann Liebert, Inc., publishers.

[99] C. Liang and C.A. Rogers. One-Dimensional Thermomechanical Constitutive Relations for Shape Memory Materials. *Journal of Intelligent Material Systems and Structures*, 1(2):207–234, April 1990. Publisher: SAGE Publications Ltd STM.

[100] Richard L. Liboff and Gregory K. Schenter. Electron-phonon scattering contri-

butions to metallic resistivity at 0 K. *Physical Review B*, 54(23):16591–16601, December 1996.

[101] W. Liu and C. R. Rahn. Fiber-Reinforced Membrane Models of McKibben Actuators. *Journal of Applied Mechanics*, 70(6):853–859, January 2004.

[102] Paulo Silva Lobo, João Almeida, and Lúis Guerreiro. Shape Memory Alloys Behaviour: A Review. *Procedia Engineering*, 114:776–783, January 2015.

[103] Yichi Luo, Jiang Zou, and Guoying Gu. Multimaterial Pneumatic Soft Actuators and Robots through a Planar Laser Cutting and Stacking Approach. *Advanced Intelligent Systems*, 3(10):2000257, 2021. _eprint: https://onlinelibrary.wiley.com/doi/pdf/10.1002/aisy.202000257.

[104] Brian Lynch, Xin-Xiang Jiang, Alex Ellery, and Fred Nitzsche. Characterization, modeling, and control of Ni-Ti shape memory alloy based on electrical resistance feedback. *Journal of Intelligent Material Systems and Structures*, 27(18):2489–2507, November 2016. Publisher: SAGE Publications Ltd STM.

[105] Sadashiva M and M Yunus Sheikh. A Review on Application of Shape Memory Alloys. *The International Journal of Recent Technology and Engineering (IJRTE)*, 9(6):111–120, March 2021.

[106] N. Ma and G. Song. Study of damping capacities of nitinol shape-memory alloys in martensite, austenite, and martensite-austenite co-existence phases.

In *Smart Structures and Materials 2005: Damping and Isolation*, volume 5760, pages 142–151. SPIE, May 2005.

[107] N Ma, G Song, and H-J Lee. Position control of shape memory alloy actuators with internal electrical resistance feedback using neural networks. *Smart Materials and Structures*, 13(4):777–783, August 2004.

[108] Farahnaz Maghooa, Agostino Stilli, Yohan Noh, Kaspar Althoefer, and Helge A Wurdemann. Tendon and pressure actuation for a bio-inspired manipulator based on an antagonistic principle. In *2015 IEEE International Conference on Robotics and Automation (ICRA)*, pages 2556–2561, May 2015. ISSN: 1050-4729.

[109] D. Roy Mahapatra and R. V. N. Melnik. Finite Element Analysis of Phase Transformation Dynamics in Shape Memory Alloys with a Consistent Landau-Ginzburg Free Energy Model. *Mechanics of Advanced Materials and Structures*, 13(6):443–455, October 2006. Publisher: Taylor & Francis _eprint: https://doi.org/10.1080/15376490600862863.

[110] Tobias Mahl, Alexander Hildebrandt, and Oliver Sawodny. A Variable Curvature Continuum Kinematics for Kinematic Control of the Bionic Handling Assistant. *IEEE Transactions on Robotics*, 30(4):935–949, August 2014.

[111] Carmel Majidi. Soft Robotics: A Perspective—Current Trends and Prospects for the Future. *Soft Robotics*, 1:5–11, March 2014.

[112] Mariangela Manti, Vito Cacucciolo, and Matteo Cianchetti. Stiffening in Soft Robotics: A Review of the State of the Art. *IEEE Robotics & Automation Magazine*, 23(3):93–106, September 2016.

[113] Hani J. Marcus, Thomas P. Cundy, Archie Hughes-Hallett, Guang-Zhong Yang, Ara Darzi, and Dipankar Nandi. Endoscopic and keyhole endoscope-assisted neurosurgical approaches: a qualitative survey on technical challenges and technological solutions. *British Journal of Neurosurgery*, 28(5):606–610, October 2014.

[114] Luc Marechal, Pascale Balland, Lukas Lindenroth, Fotis Petrou, Christos Kontovounisios, and Fernando Bello. Toward a Common Framework and Database of Materials for Soft Robotics. *Soft Robotics*, 8(3):284–297, June 2021.

[115] L. Margheri, C. Laschi, and B. Mazzolai. Soft robotic arm inspired by the octopus: I. From biological functions to artificial requirements. *Bioinspiration & Biomimetics*, 7(2):025004, May 2012. Publisher: IOP Publishing.

[116] Laura Margheri, Maurizio Follador, Matteo Cianchetti, Barbara Mazzolai, and Cecilia Laschi. Bio-inspired Design of an Artificial Muscular-Hydrostat Unit for Soft Robotic Systems. In Tony J. Prescott, Nathan F. Lepora, Anna Mura, and

Paul F. M. J. Verschure, editors, *Biomimetic and Biohybrid Systems*, Lecture Notes in Computer Science, pages 375–376, Berlin, Heidelberg, 2012. Springer.

[117] P. a. L. S. Martins, R. M. Natal Jorge, and A. J. M. Ferreira. A Comparative Study of Several Material Models for Prediction of Hyperelastic Properties: Application to Silicone-Rubber and Soft Tissues. *Strain*, 42(3):135–147, 2006. _eprint: https://onlinelibrary.wiley.com/doi/pdf/10.1111/j.1475-1305.2006.00257.x.

[118] Johnson Matthey. Nitinol-technical-properties. https://matthey.com/products-and-markets/other-markets/medical-components/resource-library/nitinol-technical-properties.

[119] Mohammadreza Memarian, Rob Gorbet, and Dana Kulić. Control of soft pneumatic finger-like actuators for affective motion generation. In *2015 IEEE/RSJ International Conference on Intelligent Robots and Systems (IROS)*, pages 1691–1697, September 2015.

[120] Kamran Mohiuddin and Scott J. Swanson. Maximizing the benefit of minimally invasive surgery. *Journal of Surgical Oncology*, 108(5):315–319, 2013. _eprint: https://onlinelibrary.wiley.com/doi/pdf/10.1002/jso.23398.

[121] T Mori and K Tanaka. Average stress in matrix and average elastic energy

of materials with misfitting inclusions. *Acta Metallurgica*, 21(5):571–574, May 1973.

[122] Bobak Mosadegh, Panagiotis Polygerinos, Christoph Keplinger, Sophia Wennstedt, Robert F. Shepherd, Unmukt Gupta, Jongmin Shim, Katia Bertoldi, Conor J. Walsh, and George M. Whitesides. Pneumatic Networks for Soft Robotics that Actuate Rapidly. *Advanced Functional Materials*, 24(15):2163–2170, 2014. _eprint: https://onlinelibrary.wiley.com/doi/pdf/10.1002/adfm.201303288.

[123] P. Motzki, J. Kunze, B. Holz, A. York, and S. Seelecke. Adaptive and energy efficient SMA-based handling systems. In *SPIE - Active and Passive Smart Structures and Integrated Systems 2015*, volume 9431, page 943116, April 2015.

[124] Paul Motzki, Julian Kunze, Alexander York, and S Seelecke. Energy-efficient SMA Vacuum Gripper System. In *Actuator 16 - 15th International Conference on New Actuators*, June 2016.

[125] Paul Motzki and Stefan Seelecke. Industrial Applications for Shape Memory Alloys. In *Encyclopedia of Smart Materials*, pages 254–266. Elsevier, November 2021.

[126] Jun-Ya Nagase, Norihiko Saga, Toshiyuki Satoh, and Koichi Suzumori. Development and control of a multifingered robotic hand using a pneumatic

tendon-driven actuator. *Journal of Intelligent Material Systems and Structures*, 23(3):345–352, February 2012. Publisher: SAGE Publications Ltd STM.

[127] Vitaly Napadow, Quingshan Chen, Van J. Wedeen, and Richard J. Gilbert. Intramural mechanics of the human tongue in association with physiological deformations. *Journal of biomechanics*, 32 1:1–12, 1999.

[128] Srinivas Neppalli and Bryan Jones. Design, construction, and analysis of a continuum robot. In *2007 IEEE/RSJ InternationalConference on Intelligent Robots and Systems (IROS)*, pages 1503–1507, December 2007.

[129] V. Novák, P. Šittner, G. N. Dayananda, F. M. Braz-Fernandes, and K. K. Mahesh. Electric resistance variation of NiTi shape memory alloy wires in thermomechanical tests: Experiments and simulation. *Materials Science and Engineering: A*, 481-482:127–133, May 2008.

[130] K. Ostuka and C. M. Wayman. *Shape memory material*. Cambridge University Press, 1998.

[131] Aniket Pal, Vanessa Restrepo, Debkalpa Goswami, and Ramses V. Martinez. Exploiting Mechanical Instabilities in Soft Robotics: Control, Sensing, and Actuation. *Advanced Materials*, 33(19):2006939, 2021. _eprint: https://onlinelibrary.wiley.com/doi/pdf/10.1002/adma.202006939.

[132] E. Patoor, A. Eberhardt, and M. Berveiller. Thermomechanical Behavior of Shape Memory Alloys, 1988.

[133] Catherine M Pemble and Bruce C Towe. A miniature shape memory alloy pinch valve. *Sensors and Actuators A: Physical*, 77(2):145–148, October 1999.

[134] Winfried Peters, Wolfgang Hagemann, and Alun Tomos. What makes plants different? Principles of extracellular matrix function in 'soft' plant tissues. *Comparative biochemistry and physiology. Part A, Molecular & integrative physiology*, 125:151–67, March 2000.

[135] Lorenza Petrini and Francesco Migliavacca. Biomedical Applications of Shape Memory Alloys. *Journal of Metallurgy*, 2011, January 2011.

[136] Panagiotis Polygerinos, Nikolaus Correll, Stephen A. Morin, Bobak Mosadegh, Cagdas D. Onal, Kirstin Petersen, Matteo Cianchetti, Michael T. Tolley, and Robert F. Shepherd. Soft Robotics: Review of Fluid-Driven Intrinsically Soft Devices; Manufacturing, Sensing, Control, and Applications in Human-Robot Interaction. *Advanced Engineering Materials*, 19(12):1700016, 2017. _eprint: https://onlinelibrary.wiley.com/doi/pdf/10.1002/adem.201700016.

[137] Panagiotis Polygerinos, Zheng Wang, Kevin C. Galloway, Robert J. Wood, and Conor J. Walsh. Soft robotic glove for combined assistance and at-home

rehabilitation. *Robotics and Autonomous Systems*, 73:135–143, 2015. Wearable Robotics.

[138] Panagiotis Polygerinos, Zheng Wang, Johannes T. B. Overvelde, Kevin C. Galloway, Robert J. Wood, Katia Bertoldi, and Conor J. Walsh. Modeling of Soft Fiber-Reinforced Bending Actuators. *IEEE Transactions on Robotics*, 31(3):778–789, June 2015.

[139] José L. Pons. *Emerging Actuator Technologies: A Micromechatronic Approach*. John Wiley and Sons, June 2005.

[140] J. L. Ponsky. Endoluminal surgery: past, present and future. *Surgical Endoscopy And Other Interventional Techniques*, 20(2):S500–S502, April 2006.

[141] Andrei Popov, Michel Labib, Julien Fays, and Ruxandra Botez. Closed-Loop Control Simulations on a Morphing Wing. *Journal of Aircraft - J AIRCRAFT*, 45:1794–1803, September 2008.

[142] Lori Michelle Prothero. *SHAPE MEMORY ALLOY ROBOTIC TRUSS*. PhD thesis, Auburn University, 2008.

[143] Yun Qin, Zhenyu Wan, Yinan Sun, Erik H. Skorina, Ming Luo, and Cagdas D. Onal. Design, fabrication and experimental analysis of a 3-D soft robotic snake. In *2018 IEEE International Conference on Soft Robotics (RoboSoft)*, pages 77–82, Livorno, April 2018. IEEE.

[144] John A. Redmond, Diann Brei, Jonathan Luntz, Alan L. Browne, Nancy L. Johnson, and Kenneth A. Strom. The Design and Experimental Validation of an Ultrafast Shape Memory Alloy ResetTable (SMART) Latch. *Journal of Mechanical Design*, 132(6), May 2010.

[145] Tariq Rehman, Ahmad Athif Mohd Faudzi, Dyah Ekashanti Octorina Dewi, and Mohamad Sultan Mohamad Ali. Design, characterization, and manufacturing of circular bellows pneumatic soft actuator. *The International Journal of Advanced Manufacturing Technology*, 93(9):4295–4304, December 2017.

[146] Tao Ren, Yingtian Li, Menghong Xu, Yunquan Li, Caihua Xiong, and Yonghua Chen. A Novel Tendon-Driven Soft Actuator with Self-Pumping Property. *Soft Robotics*, 7(2):130–139, April 2020. Publisher: Mary Ann Liebert, Inc., publishers.

[147] David Rigberg, Allan Tulloch, Youngjae Chun, Kotekar Panduranga Mohanchandra, Greg Carman, and Peter Lawrence. Thin-film nitinol (NiTi): A feasibility study for a novel aortic stent graft material. *Journal of Vascular Surgery*, 50(2):375–380, August 2009.

[148] Hugo Rodrigue, Wei Wang, Binayak Bhandari, Min-Woo Han, and Sung-Hoon Ahn. SMA-based smart soft composite structure capable of multiple modes of actuation. *Composites Part B: Engineering*, 82:152–158, December 2015.

[149] T.A.U. Roshan, B.A.D.J.C.K. Basnayake, Y.W.R. Amarasinghe, Dimuthu Wijethunge, and Nuwan D Nanayakkara. Development of a PID Based Closed Loop Controller for Shape Memory Alloy Actuators. In *2018 Moratuwa Engineering Research Conference (MERCon)*, pages 460–464, May 2018.

[150] Josephine Ruth D, Dhanalakshmi Kaliaperumal, and Sunjai Nakshatharan. Bidirectional angular control of an integrated sensor/actuator shape memory alloy based system. *Measurement*, 69:210–221, June 2015.

[151] Amir Sadjadpour and Kaushik Bhattacharya. A micromechanics inspired constitutive model for shape-memory alloys: the one-dimensional case. *Smart Materials and Structures*, 16(1):S51–S62, January 2007. Publisher: IOP Publishing.

[152] Marcos Fernando Bujanda Sanchez. *ELECTRONS IN SOLIDS Third Edition An Introductory Survey*. Academic Press, 1992.

[153] Debadrata Sarkar, Shounak Dasgupta, Srinivasa N., Aman Arora, and Soumen Sen. A Soft Bending-type Actuator using Hyper-elastic Materials: Development, Analysis and Characterization. In *Advances in Robotics 2019 (AIR 2019)*, pages 1–7, July 2019.

[154] Andrea Sellitto and Aniello Riccio. Overview and Future Advanced Engineering Applications for Morphing Surfaces by Shape Memory Alloy Materials. *Mate-*

rials, 12(5):708, January 2019. Number: 5 Publisher: Multidisciplinary Digital Publishing Institute.

[155] Sangok Seok, Cagdas D. Onal, Robert Wood, Daniela Rus, and Sangbae Kim. Peristaltic locomotion with antagonistic actuators in soft robotics. In *2010 IEEE International Conference on Robotics and Automation*, pages 1228–1233, May 2010. ISSN: 1050-4729.

[156] Sangok Seok, Cagdas Denizel Onal, Kyu-Jin Cho, Robert J. Wood, Daniela Rus, and Sangbae Kim. Meshworm: A Peristaltic Soft Robot With Antagonistic Nickel Titanium Coil Actuators. *IEEE/ASME Transactions on Mechatronics*, 18(5):1485–1497, October 2013.

[157] Ahmed A. Shabana and Refaat Y. Yakoub. Three Dimensional Absolute Nodal Coordinate Formulation for Beam Elements: Theory. *Journal of Mechanical Design*, 123(4):606–613, May 2000.

[158] Robert F. Shepherd, Filip Ilievski, Wonjae Choi, Stephen A. Morin, Adam A. Stokes, Aaron D. Mazzeo, Xin Chen, Michael Wang, and George M. Whitesides. Multigait soft robot. *Proceedings of the National Academy of Sciences*, 108(51):20400–20403, 2011. Publisher: National Academy of Sciences _eprint: https://www.pnas.org/content/108/51/20400.full.pdf.

[159] Muhammad M Sherif and Osman E Ozbulut. Thermomechanical and electrical

response of a superelastic NiTi shape memory alloy cable. *Journal of Intelligent Material Systems and Structures*, 31(19):2229–2242, November 2020. Publisher: SAGE Publications Ltd STM.

[160] Samuel Shian, Katia Bertoldi, and David R. Clarke. Dielectric Elastomer Based "Grippers" for Soft Robotics. *Advanced Materials*, 27(43):6814–6819, 2015. _eprint: https://onlinelibrary.wiley.com/doi/pdf/10.1002/adma.201503078.

[161] Ali Shiva, Agostino Stilli, Yohan Noh, Angela Faragasso, Iris De Falco, Giada Gerboni, Matteo Cianchetti, Arianna Menciassi, Kaspar Althoefer, and Helge A. Wurdemann. Tendon-Based Stiffening for a Pneumatically Actuated Soft Manipulator. *IEEE Robotics and Automation Letters*, 1(2):632–637, July 2016.

[162] Gaurav Singh and Girish Krishnan. A constrained maximization formulation to analyze deformation of fiber reinforced elastomeric actuators. *Smart Materials and Structures*, 26(6):065024, May 2017. Publisher: IOP Publishing.

[163] Gaurav Singh, Chenzhang Xiao, Elizabeth T. Hsiao-Wecksler, and Girish Krishnan. Design and analysis of coiled fiber reinforced soft pneumatic actuator. *Bioinspiration & Biomimetics*, 13(3):036010, April 2018. Publisher: IOP Publishing.

[164] Inderjeet Singh, Yacine Amara, Melingui Achille, Pushparaj Pathak, and

Rochdi Merzouki. Modeling of Continuum Manipulators Using Pythagorean Hodograph Curves. *Soft Robotics*, 5, May 2018.

[165] G Song. Robust position regulation of a shape memory alloy wire actuator. *Proceedings of The Institution of Mechanical Engineers Part I-journal of Systems and Control Engineering - PROC INST MECH ENG I-J SYST C*, 216:301–308, May 2002.

[166] Dileep Kumar Soother, Jawaid Daudpoto, and Bhawani Shankar Chowdhry. Challenges for practical applications of shape memory alloy actuators. *Materials Research Express*, 7(7):073001, July 2020. Publisher: IOP Publishing.

[167] M. Sreekumar, T. Nagarajan, M. Singaperumal, M. Zoppi, and R. Molfino. Critical review of current trends in shape memory alloy actuators for intelligent robots. *Industrial Robot: An International Journal*, 34(4):285–294, January 2007. Publisher: Emerald Group Publishing Limited.

[168] Kim Young Su, Jahan Zeb Gul, and Kyung Hyun Choi. A biomimetic jumping locomotion of functionally graded frog soft robot. In *2017 14th International Conference on Ubiquitous Robots and Ambient Intelligence (URAI)*, pages 675–676, 2017.

[169] Qing Ping Sun and Keh Chih Hwang. Micromechanics modelling for the constitutive behavior of polycrystalline shape memory alloys—I. Derivation of general

relations. *Journal of the Mechanics and Physics of Solids*, 41(1):1–17, January 1993.

[170] Yi Sun, Yun Seong Song, and Jamie Paik. Characterization of silicone rubber based soft pneumatic actuators. In *2013 IEEE/RSJ International Conference on Intelligent Robots and Systems*, pages 4446–4453, November 2013. ISSN: 2153-0866.

[171] K. Suzumori, S. Iikura, and H. Tanaka. Development of flexible microactuator and its applications to robotic mechanisms. In *1991 IEEE International Conference on Robotics and Automation Proceedings*, pages 1622–1627 vol.2, April 1991.

[172] K. Tanaka. A Thermomechanical Sketch of Shape Memory Effect : One-Dimensional Tensile Behavior. *Materials Science*, January 1986.

[173] K. Tanaka and S. Nagaki. A thermomechanical description of materials with internal variables in the process of phase transitions. *Ingenieur-Archiv*, 51(5):287–299, September 1982.

[174] Hironari Taniguchi. Flexible Artificial Muscle Actuator Using Coiled Shape Memory Alloy Wires. *APCBEE Procedia*, 7:54–59, January 2013.

[175] B. Tondu and P. Lopez. Modeling and control of McKibben artificial muscle robot actuators. *IEEE Control Systems Magazine*, 20(2):15–38, April 2000.

[176] Deepak Trivedi, Christopher D. Rahn, William M. Kier, and Ian D. Walker. Soft robotics: Biological inspiration, state of the art, and future research. *Applied Bionics and Biomechanics*, 5(3):99–117, January 2008. Publisher: IOS Press.

[177] N. Troisfontaine, Philippe Bidaud, and Paolo Dario. Control experiments on two SMA based micro-actuators. In Alicia Casals and Anibal T. de Almeida, editors, *Experimental Robotics V*, pages 490–499. Springer Berlin Heidelberg, December 2007.

[178] Allan Joshua Veale and Shane Quan Xie. Towards compliant and wearable robotic orthoses: A review of current and emerging actuator technologies. *Medical Engineering & Physics*, 38(4):317–325, April 2016.

[179] Alexander G. Volkov, Tejumade Adesina, Vladislav S. Markin, and Emil Jovanov. Kinetics and Mechanism of Dionaea muscipula Trap Closing. *Plant Physiology*, 146(2):694–702, 2008. Publisher: American Society of Plant Biologists _eprint: http://www.plantphysiol.org/content/146/2/694.full.pdf.

[180] Arthur Munzenmaier Wahl. *Mechanical Springs*. Penton Publishing Company, 1944. Google-Books-ID: dKZBAAAAIAAJ.

[181] James Walker, Thomas Zidek, Cory Harbel, Sanghyun Yoon, F. Sterling Strickland, Srinivas Kumar, and Minchul Shin. Soft Robotics: A Review of Recent

Developments of Pneumatic Soft Actuators. *Actuators*, 9(1):3, March 2020. Number: 1 Publisher: Multidisciplinary Digital Publishing Institute.

[182] Boran Wang, Kean C. Aw, Morteza Biglari-Abhari, and Andrew McDaid. Design and fabrication of a fiber-reinforced pneumatic bending actuator. In *2016 IEEE International Conference on Advanced Intelligent Mechatronics (AIM)*, pages 83–88, July 2016.

[183] L. X. Wang and R. V. N. Melnik. Thermo-Mechanical Wave Propagations in Shape Memory Alloy Rod with Phase Transformations. *Mechanics of Advanced Materials and Structures*, 14(8):665–676, November 2007. Publisher: Taylor & Francis _eprint: https://doi.org/10.1080/15376490701673227.

[184] Wei Wang, Nam-Geuk Kim, Hugo Rodrigue, and Sung-Hoon Ahn. Modular assembly of soft deployable structures and robots. *Materials Horizons*, 4(3):367–376, May 2017. Publisher: The Royal Society of Chemistry.

[185] Y. Wang and A. G. Khachaturyan. Three-dimensional field model and computer modeling of martensitic transformations. *Acta Materialia*, 45(2):759–773, February 1997.

[186] Zheng Wang, Panagiotis Polygerinos, Johannes T. B. Overvelde, Kevin C. Galloway, Katia Bertoldi, and Conor J. Walsh. Interaction Forces of Soft Fiber

Reinforced Bending Actuators. *IEEE/ASME Transactions on Mechatronics*, 22(2):717–727, April 2017.

[187] Zhongkui Wang and Shinichi Hirai. Chamber dimension optimization of a bellow-type soft actuator for food material handling. In *2018 IEEE International Conference on Soft Robotics (RoboSoft)*, pages 382–387, April 2018.

[188] R. Webster and Bryan A. Jones. Design and Kinematic Modeling of Constant Curvature Continuum Robots: A Review. *Int. J. Robotics Res.*, 2010.

[189] M. Wehner, Y. Park, C. Walsh, R. Nagpal, R. J. Wood, T. Moore, and E. Goldfield. Experimental characterization of components for active soft orthotics. In *2012 4th IEEE RAS EMBS International Conference on Biomedical Robotics and Biomechatronics (BioRob)*, pages 1586–1592, June 2012. ISSN: 2155-1774.

[190] George M. Whitesides. Soft Robotics. *Angewandte Chemie International Edition*, 57(16):4258–4273, 2018. _eprint: https://onlinelibrary.wiley.com/doi/pdf/10.1002/anie.201800907.

[191] X. Wu, Jihong Wu, and Zhiqiang Wang. The variation of electrical resistance of near stoichiometric NiTi during thermo-mechanic procedures. *Smart Materials and Structures*, 1999.

[192] X. D. Wu, Y. Z. Fan, and J. S. Wu. A study on the variations of the electrical

resistance for NiTi shape memory alloy wires during the thermo-mechanical loading. *Materials & Design*, 21(6):511–515, December 2000.

[193] Matheus S. Xavier, Andrew J. Fleming, and Yuen K. Yong. Finite element modeling of soft fluidic actuators: Overview and recent developments. *Advanced Intelligent Systems*, 3(2):2000187, 2021.

[194] Matheus S. Xavier, Charbel D. Tawk, Ali Zolfagharian, Joshua Pinskier, David Howard, Taylor Young, Jiewen Lai, Simon M. Harrison, Yuen K. Yong, Mahdi Bodaghi, and Andrew J. Fleming. Soft Pneumatic Actuators: A Review of Design, Fabrication, Modeling, Sensing, Control and Applications. *IEEE Access*, 10:59442–59485, 2022.

[195] Wei Xiao, Dean Hu, Weixiong Chen, Gang Yang, and Xu Han. Design, Characterization and Optimization of Multi-directional Bending Pneumatic Artificial Muscles. *Journal of Bionic Engineering*, 18(6):1358–1368, November 2021.

[196] Zhou Xue, Qiuxuan Wu, and Farong Gao. Design and modeling of omnidirectional bending pneumatic flexible arm. *2018 3rd International Conference on Advanced Robotics and Mechatronics (ICARM)*, pages 835–839, 2018.

[197] Seung Man Yang, Jae-Hung Han, and In Lee. Characteristics of smart composite wing with SMA actuators and optical fiber sensors. *International Journal of Applied Electromagnetics and Mechanics*, 23:177–186, September 2006.

[198] Ying Yang, Yanxiao Wu, Cheng Li, Xiaoming Yang, and Wei Chen. Flexible Actuators for Soft Robotics. *Advanced Intelligent Systems*, 2(1):1900077, 2020. _eprint: https://onlinelibrary.wiley.com/doi/pdf/10.1002/aisy.201900077.

[199] Yee Harn Teh and Roy Featherstone. An Architecture for Fast and Accurate Control of Shape Memory Alloy Actuators. *The International Journal of Robotics Research*, 27(5):595–611, May 2008.

[200] Jung-Hwan Youn, Seung Mo Jeong, Geonwoo Hwang, Hyunwoo Kim, Kyujin Hyeon, Jihwan Park, and Ki-Uk Kyung. Dielectric Elastomer Actuator for Soft Robotics Applications and Challenges. *Applied Sciences*, 10(2):640, January 2020. Number: 2 Publisher: Multidisciplinary Digital Publishing Institute.

[201] Jian Zhang, Junjie Zhou, Shihua Yuan, and Chongbo Jing. Design, Fabrication and Experiments of a 3D-motion Soft Elastomer Actuator. In *2019 IEEE International Conference on Mechatronics and Automation (ICMA)*, pages 497–501, August 2019. ISSN: 2152-744X.

[202] Zhiyuan Zhang, Xueqian Wang, Songtao Wang, Deshan Meng, and Bin Liang. Design and Modeling of a Parallel-Pipe-Crawling Pneumatic Soft Robot. *IEEE Access*, 7:134301–134317, 2019.

[203] Petr Šittner and Václav Novák. Anisotropy of martensitic transformations in

modeling of shape memory alloy polycrystals. *International Journal of Plasticity*, 16(10):1243–1268, January 2000.